The Astrophysical Journal, 775:111 (34pp), 2013 October 1 doi:10.1088/0004-637X/775/2/111

MODELING THE POLLUTION OF PRISTINE GAS IN THE EARLY UNIVERSE

Liubin Pan[1], Evan Scannapieco[2], and Jon Scalo[3]
[1] Harvard-Smithsonian Center for Astrophysics, 60 Garden St., Cambridge, MA 02138, USA; lpan@cfa.harvard.edu
[2] School of Earth and Space Exploration, Arizona State University, P.O. Box 871404, Tempe, AZ 85287-1494, USA; evan.scannapieco@asu.edu
[3] Department of Astronomy, University of Texas, Austin, TX 78712, USA; parrot@astro.as.utexas.edu
Received 2012 December 18; accepted 2013 June 17; published 2013 September 13

ABSTRACT

We conduct a comprehensive theoretical and numerical investigation of the pollution of pristine gas in turbulent flows, designed to provide useful new tools for modeling the evolution of the first generation of stars. The properties of such Population III (Pop III) stars are thought to be very different than those of later stellar generations, because cooling is dramatically different in gas with a metallicity below a critical value Z_c, which lies between $\sim 10^{-6}$ and $\sim 10^{-3}\ Z_\odot$. The critical value is much smaller than the typical overall average metallicity, $\langle Z \rangle$, and therefore the mixing efficiency of the pristine gas in the interstellar medium plays a crucial role in determining the transition from Pop III to normal star formation. The small critical value, Z_c, corresponds to the far left tail of the probability distribution function (PDF) of the metal abundance. Based on closure models for the PDF formulation of turbulent mixing, we derive evolution equations for the fraction of gas, P, lying below Z_c, in statistically homogeneous compressible turbulence. Our simulation data show that the evolution of the pristine fraction P can be well approximated by a generalized "self-convolution" model, which predicts that $\dot{P} = -(n/\tau_{\rm con})P(1 - P^{1/n})$, where n is a measure of the locality of the mixing or PDF convolution events and the convolution timescale $\tau_{\rm con}$ is determined by the rate at which turbulence stretches the pollutants. Carrying out a suite of numerical simulations with turbulent Mach numbers ranging from $M = 0.9$ to 6.2, we are able to provide accurate fits to n and $\tau_{\rm con}$ as a function of M, $Z_c/\langle Z \rangle$, and the length scale, L_p, at which pollutants are added to the flow. For pristine fractions above $P = 0.9$, mixing occurs only in the regions surrounding blobs of pollutants, such that $n = 1$. For smaller values of P, n is larger as the mixing process becomes more global. We show how these results can be used to construct one-zone models for the evolution of Pop III stars in a single high-redshift galaxy, as well as subgrid models for tracking the evolution of the first stars in large cosmological numerical simulations.

Key words: dark ages, reionization, first stars – evolution – galaxies: high-redshift – ISM: abundances – stars: Population III – turbulence

Online-only material: color figures

1. INTRODUCTION

All stable elements heavier than lithium were forged in stars. Big bang nucleosynthesis produced helium efficiently, but it was halted by the expansion of the universe before it could go much further (Walker et al. 1991). On the other hand, all stars observed to date have substantial mass fractions of carbon, silicon, iron, and other elements that are the products of the final stages of stellar evolution. In fact, even the most pristine stars observed (Cayrel et al. 2004; Frebel et al. 2008; Caffau et al. 2011) have been polluted by this material. The earliest stellar generation, referred to as Population III (Pop III), is missing.

While this absence could be due to the formation of an extremely small number of metal-free stars, detailed theoretical studies suggest that it is more likely that these stars were too massive to survive to the present day (Scannapieco et al. 2006; Brook et al. 2007). In fact, the absence of heavy elements drastically decreases the cooling rates in collapsing star-forming gas, such that that primordial gas clouds would have been much less susceptible to fragmentation, perhaps forming 10^3–10^4 solar mass star-forming clumps (Hutchins 1976; Abel et al. 2000; Bromm et al. 2002; Bromm & Loeb 2003). Furthermore, the strong accretion rates onto the central protostellar cores in such pristine clumps cannot be arrested by radiation pressure, bipolar outflows, or rotation (Ferrara 2001), meaning that these regions may have formed stars with masses hundreds of times greater than the sun. On the other hand, recent work suggests that physical processes, such as enhanced hydrogen deuteride (HD) cooling in shock-compressed primordial gas (Johnson & Bromm 2006), a lack of magnetic fields in primordial turbulent clouds (Padoan et al. 2007), photoionization of turbulent primordial clouds (Clark et al. 2011a), fragmentation of the protostellar accretion disks (e.g., Stacy et al. 2010; Clark et al. 2011b), early termination of accretion (McKee & Tan 2008; Hosokawa et al. 2011), and gravitational torques (Greif et al. 2012), may have led to primordial stars with masses $\approx 10\ M_\odot$ in single or perhaps binary systems (Turk et al. 2009).

Even at these comparatively low masses, direct detections of primordial stars would be possible only through observations of the high-redshift universe, relying on what is likely to have been an extended transition between metal-free and pre-enriched (Population II/I) star formation (Scannapieco et al. 2003; Jimenez & Haiman 2006; Trenti & Stiavelli 2007, 2009; Maio et al. 2010), as well as the unusual observable signatures of metal-free stars. During their lifetimes, for example, the lack of heavy elements in Pop III stars drastically reduces their opacities, resulting in much higher surface temperatures and strong ultraviolet spectroscopic features that would distinguish them from current stellar populations (Schaerer 2002; Nagao et al. 2008). Alternatively, if they were extremely massive, Pop III stars could be detectable as they ended their lives as tremendously powerful pair-production supernovae (Bond et al. 1984; Heger & Woosley 2002; Scannapieco et al. 2005; Whalen et al. 2012). Furthermore, the reliance on H_2 + HD cooling in primordial gas may have effects beyond masses of stars, such as affecting the phase nature of the interstellar medium (ISM) and the star formation rate (Norman & Spaans 1997).

Whatever the detection method, when and where metal-free gas condensed into stars is a question of fundamental importance in planning searches for this remarkable early generation of stars. On cosmological scales, the key issue is the time it takes for heavy elements to propagate from one galaxy to another. As shown in Scannapieco et al. (2003), the distances between these oases of early star formation are so vast that for several hundred million years, the universe was divided into two regions: one in which galaxies formed out of material that was already polluted with heavy elements well above the minimum "critical mass fraction," Z_c, at which normal stellar evolution occurs (Schneider et al. 2003; Bromm & Loeb 2003; Omukai et al. 2005), and one in which galaxies were formed from initially pristine material.

The evolution of initially pristine galaxies is especially interesting, as it depends on two important theoretical issues. The first of these is the uncertain value of Z_c, which is expected to lie in the range from $\sim 10^{-8}$ to $\sim 10^{-5}$ (or from 10^{-6} to 10^{-3} times solar metallicity), depending on whether the cooling is dominated by dust grains (Omukai et al. 2005) or by the fine structure lines of carbon and oxygen (Bromm & Loeb 2003). The second important issue is the rate at which the gas within the galaxy can be polluted above this critical value by the turbulent mixing of heavy elements (Pan & Scalo 2007). Within a given galaxy, the key quantity to characterize the transition is the fraction, $P(Z_c, t)$, of the interstellar gas with metal concentration Z below Z_c as a function of time. The temporal behavior of this fraction depends not only on the rate at which new sources of metals are released to the interstellar gas, but, more importantly, on the transport and mixing of the metals in the interstellar gas. For example, a high mixing efficiency would result in a rapid decrease in $P(Z_c, t)$, and hence a sharp transition as the average concentration exceeds the threshold Z_c. On the other hand, a low mixing efficiency would lead to a gradual transition. The ISM is known to be turbulent and highly compressible, and the turbulent motions are likely to be supersonic. Therefore, understanding mixing in supersonic turbulence is crucial to understanding the evolution of primordial gas in early galaxies. The evolution of the pristine fraction was considered by Oey (2000, 2003) in the context of the sequential enrichment model, which, however, does not correctly reflect or capture the physics of mixing in interstellar turbulence (Pan & Scalo 2007).

In Pan et al. (2012, hereafter PSS), we developed a theoretical approach to model the evolution of the pristine fraction in statistically homogeneous turbulence. The starting point of our theoretical model was the probability distribution function (PDF) method for turbulent mixing, since the pristine fraction $P(Z_c, t)$ corresponds to the far left tail of the metallicity PDF. The PDF equation for passive scalars cannot be solved exactly, and we adopted several closure models from the literature and derived predictions for the evolution of the pristine fraction. Using numerical simulations, we showed that a class of PDF closure models, called self-convolution models, provided successful fitting functions to the evolution of $P(Z_c, t)$ for a limited range of flow Mach number and pollution properties. These models are based on the physical picture of turbulence stretching pollutants and causing a cascade of concentration structures toward small scales (Pan & Scalo 2007), a picture that is generally valid in turbulent flows at all Mach numbers (Pan & Scannapieco 2010, hereafter PS10). Mixing occurs as the scale of the structures becomes sufficiently small for molecular diffusivity to efficiently operate, and the homogenization between neighboring structures can be described as a convolution of the concentration PDF. As discussed in more detail below, the models are dependent on two major parameters: $\tau_{\rm con}$, which sets the characteristic timescale for convolution of the metal abundance PDF through turbulent stretching of concentration structures, and n, which quantifies the degree of spatial locality of the PDF convolution process.

Here, we use a suite of numerical simulations to expand these results and show that the generalized self-convolution model provides good fits for all the turbulence and pollutant conditions relevant for primordial star formation. Note that, besides affecting the temperature directly, H_2 + HD cooling without heavy elements makes neutral primordial gas less compressible (Scalo & Biswas 2002; Spaans & Silk 2005), emphasizing the importance of studying the Mach number dependence of the pollution processes. By comparing this model to simulations with Mach numbers $M = 0.9$, 2.1, 3.5, and 6.2, in which pollutants are added at different length scales, and four different initial values of P, we are able to obtain detailed fits of $\tau_{\rm con}$, and n over all Mach numbers, initial pollution fraction, and pollution scales of interest. We tabulate and obtain empirical fits to our results, and show how they can be used both to make simple one-zone estimates of the evolution of P within a single high-redhshift galaxy, as well as to construct a subgrid model for numerical simulations, which tracks the evolution of the primordial fraction below the resolution scale. The model is expected to improve the prediction for the evolution of the primordial gas fraction in early galaxies, and should also be applicable to any physical problem in which the unresolved, unmixed fraction needs to be tracked throughout a simulation.

A realistic simulation for the pollution of the pristine gas in early galaxies needs to properly specify the driving mechanism of the interstellar turbulence. A variety of physical processes may contribute to turbulent motions in the ISM. Turbulence can be produced at galactic scales, e.g., by the gas infall from the halo or by merger events during the assembly of the galaxy. Supernova explosions by the first stars also contribute to the turbulent energy. In the present work, we adopt a solenoidal driving force in the simulations, which may be a good approximation if the interstellar turbulence is mainly driven by large-scale motions or instabilities, associated with galaxy formation, mergers, or interactions. On the other hand, if the primary source for turbulent energy is stellar winds and supernova explosions, the driving force may be compressive rather than solenoidal. In that case, several questions need to be addressed by future studies. First, as shown by Federrath et al. (2010), a compressively driven supersonic turbulent flow shows significantly different statistics than the solenoidal case. The amplitude of the density fluctuations is much larger due to stronger compressions, and the intermittency of the velocity field is significantly higher. We will speculate how these features may qualitatively affect the parameters in our convolution models. A quantitative understanding may be obtained by a suite of simulations using driving forces at different degrees of compressibility. Second, if supernovae are the primary energy source of turbulence, the injection of heavy elements is highly correlated with the turbulent driving force. This is not accounted for in our simulations either. These issues are complicated and require a systematic investigation. This is, however, beyond of the scope of the current paper, which is essentially an initial step that provides the theoretical framework and useful subgrid methodology for the modeling of the pristine gas pollution in early galaxies.

The structure of this work is as follows. In Section 2, we introduce the PDF formulation for turbulent mixing and discuss the fundamental mixing physics. In Section 3, we describe the self-convolution closure models, and show how they can be used to predict the evolution of the pristine fraction in statistically homogeneous turbulence. In Section 4, we describe our suite of numerical simulations, and in Section 5, we use them to test and constrain the self-convolution models over the full range of turbulence and pollution conditions necessary to model primordial star formation. Having fixed the parameters in the theoretical models with our simulation results we show how they can then be applied to one-zone models of high-redshift galaxies in Section 6, and in Section 7, we show how they can be used to construct subgrid models for the unresolved primordial fraction in large, numerical simulations. A summary of our conclusions is given in Section 8.

2. THE PDF FORMULATION FOR TURBULENT MIXING

The mixing of heavy elements in the ISM can be studied by tracking the evolution of the concentration field, $C(\mathbf{x}, t)$, defined as the ratio of the local density of these elements to the total gas density. The concentration field obeys the advection-diffusion equation,

$$\frac{\partial C}{\partial t} + v_i \frac{\partial C}{\partial x_i} = \frac{1}{\rho}\frac{\partial}{\partial x_i}\left(\rho\gamma\frac{\partial C}{\partial x_i}\right) + S(\mathbf{x}, t), \quad (1)$$

where $\rho(\mathbf{x}, t)$ and $\mathbf{v}(\mathbf{x}, t)$ denote the density and velocity fields in interstellar turbulence, γ is the molecular diffusivity, and the term $S(\mathbf{x}, t)$ represents continuing sources of heavy elements or pollutants. The concentration field, $C(\mathbf{x}, t)$, could also represent the local abundance of a specific element, but here we are interested in the mass fraction of all metals at a given location. The pristine mass fraction in a flow corresponds to the low tail of the PDF of the pollutant concentration, so we adopt a PDF approach for turbulent mixing.

This approach was first established for the turbulent velocity field (Monin 1967; Lundgren 1967) and was later extended to mixing of passive or reactive species in turbulent flows (Ievlev 1973; Dopazo & O'Brien 1974; Pope 1976, 1985; O'Brien 1980; Kollmann 1990; Dopazo et al. 1997). It has been particularly successful in the field of reacting turbulent flows (e.g., Haworth 2010). However, most of the work on the PDF modeling of turbulent mixing has been dedicated to incompressible or weakly compressible turbulence. In order to apply the method to the ISM of galaxies, where strong density fluctuations exist, PSS generalized the PDF formulation to mixing in highly compressible turbulent flows at large Mach numbers, emphasizing the importance of using a density weighting scheme.

As in PSS, here we use a statistical ensemble to define a density-weighted concentration PDF, $\Phi(Z; \mathbf{x}, t) \equiv \langle\rho\phi(Z; \mathbf{x}, t)\rangle/\langle\rho(\mathbf{x}, t)\rangle$, where $\phi(Z; \mathbf{x}, t) \equiv \delta(Z - C(\mathbf{x}, t))$ is the fine-grained PDF in a single realization, $\langle\cdots\rangle$ denotes the ensemble average, and Z is the sampling variable. The probability distribution defined here at a given position and time is an average over many independent realizations in the statistical ensemble. The ensemble average density, $\langle\rho(\mathbf{x}, t)\rangle$, is in general a function of $\mathbf{x}$ and t. In PSS, $\langle\rho(\mathbf{x}, t)\rangle$ was implicitly assumed to be constant. Below we consider the more general case that accounts for the spatial and temporal variations of $\langle\rho(\mathbf{x}, t)\rangle$. An important motivation for using a density-weighting factor is that, when studying mixing of primordial gas in early galaxies, it is appropriate to consider the mass fraction, rather than the volume fraction, of the interstellar gas with $Z \leqslant Z_c$.

An equation for $\Phi(Z; \mathbf{x}, t)$ can be derived using the advection-diffusion equation (1), for $C(\mathbf{x}, t)$, and the continuity equation, for $\rho(\mathbf{x}, t)$. Applying the same method as in Appendix A of PSS and accounting for the spatial and temporal dependence of $\langle\rho\rangle$, we find

$$\frac{\partial(\langle\rho\rangle\Phi)}{\partial t} + \frac{\partial}{\partial x_i}(\langle\rho\rangle\Phi\langle v_i|C = Z\rangle_\rho) = -\frac{\partial}{\partial Z}\left(\langle\rho\rangle\Phi\left\langle\frac{1}{\rho}\frac{\partial}{\partial x_i}\left(\rho\gamma\frac{\partial C}{\partial x_i}\right)\middle| C = Z\right\rangle_\rho\right) - \frac{\partial}{\partial Z}(\langle\rho\rangle\Phi\langle S|C = Z\rangle_\rho), \quad (2)$$

where $\langle\ldots|C = Z\rangle_\rho$ denotes the conditional ensemble average with density weighting. For any physical quantity, $A(\mathbf{x}, t)$, this ensemble average is defined as

$$\langle A|C = Z\rangle_\rho \equiv \frac{\langle\rho A|C = Z\rangle}{\langle\rho|C = Z\rangle}, \quad (3)$$

where the conditional average $\langle\ldots|C = Z\rangle$ without density weighting is evaluated by selecting and counting only those realizations satisfying the constraint that the concentration $C(\mathbf{x}, t)$ at $\mathbf{x}$ and t is equal to Z. Setting $\langle\rho(\mathbf{x}, t)\rangle$ to be constant reduces Equation (2) to Equation (2.2) in PSS. Derivations of analogous PDF equations for passive and reacting scalar turbulence in the incompressible case can be found in, e.g., Pope (2000) and Fox (2003). The PDF equation is essentially a Liouville equation for the conservation of the concentration probability in phase space. Analogous to the Liouville equation in kinetic theory, the concentration field corresponds to the particle momentum and the advection-diffusion equation corresponds to the particle equation of motion (PSS).

Although the PDF equation is derived in the context of a statistical ensemble, it is also useful for the study of scalar statistics in a single realization, i.e., the real flow. If the flow and the scalar statistics are spatially homogeneous, $\langle\rho(\mathbf{x}, t)\rangle$ and $\Phi(Z; \mathbf{x}, t)$, are independent of $\mathbf{x}$, and the ergodic theorem indicates that the statistics over an ensemble is equivalent to that over the spatial domain of a single realization. This means that $\Phi(Z; \mathbf{x}, t)$ is equal to the PDF, $\Phi(Z; t) = \int_V \rho\delta(Z - C(\mathbf{x}, t))dx^3/\int_V \rho dx^3$, computed from the density and concentration fluctuations over the entire volume, V, of the real flow domain. At galactic length scales, the assumption of statistical homogeneity is likely invalid. For example, coherent mean flows, such as galactic rotation, infall, or outflow, may exist at large scales in the ISM. Also a large-scale metallicity gradient may develop if the star formation rate has a radial dependence, and the metallicity statistics can vary substantially from region to region.

However, the ensemble-defined PDF $\Phi(Z; \mathbf{x}, t)$ may still be used to study this spatial dependence if it is understood as corresponding to the concentration PDF for local fluctuations in a region of considerable size in the real flow. If the size is selected to be large enough to allow sufficient statistics, but small enough for local statistical homogeneity to be restored (i.e., considerably smaller than the characteristic scale for the mean flow or mean concentration gradient), then the ergodic theorem will apply locally, and $\Phi(Z; \mathbf{x}, t)$ will represent the PDF in the region around $\mathbf{x}$. In fact, in an attempt to build a subgrid model for the pollution of pristine interstellar gas, a concentration PDF characterizing the fluctuations in local regions is defined by applying a spatial filter to the real flow (see Section 7 and the Appendix), and the equation derived for the filtered PDF is identical to Equation (2) for $\Phi(Z; \mathbf{x}, t)$ over an ensemble.

This confirms the equivalence of $\Phi(Z; \mathbf{x}, t)$ to the local concentration PDF in the real flow and the applicability of Equation (2) to the study of mixing in a statistically inhomogeneous setting.

The last three terms in Equation (2) correspond to turbulent advection, molecular diffusivity, and source terms in the advection-diffusion equation. We give a brief general discussion for each term below, and refer the interested reader to PSS for more details.

2.1. The Advection Term

The second term in Equation (2) is the advection term. As it takes a divergence form, it conserves the global PDF with density weighting, i.e., the integral of $\langle\rho\rangle\Phi(Z; \mathbf{x}, t)$ over the entire flow domain. This corresponds to a fundamental issue in mixing physics: the turbulent velocity field does not homogenize at all by itself. Intuitively, a velocity field moves, stretches, and redistributes the concentration field, but it does not change the *mass* fraction of the fluid elements at a given concentration level, and thus does not truly mix. On the other hand, without density weighting, the advection term in the PDF equation would not be a divergence term if the flow is compressible, but instead would be a term representing the effect of expansions and compressions on the volume fraction of fluid elements at a given concentration. This effect is different from mixing, and makes the PDF modeling more complicated. Therefore, in addition to the practical reasons mentioned above, adopting a density-weighting scheme is also strongly motivated on a theoretical basis.

The advection term vanishes and need not be considered in a flow that is statistically homogeneous. In case of statistical inhomogeneity, the term corresponds to the transport of the concentration PDF by the velocity field: turbulent advection causes changes in the local PDF as it moves the fluid elements around. If one is interested in the concentration fluctuations in a local region, this transport effect must be accounted for carefully. A similar advection term exists in the equation for the filtered PDF of the local concentration fluctuations, which is used to build a subgrid model for the pollution of pristine gas in early galaxies in Section 7. In that case, a proper treatment of the advection term is essential, as it is responsible for the flux of pristine mass fraction into or out of a computation cell due to the velocity field (see Section 7). However, an exact treatment of the advection term is impossible due to the usual difficulty in turbulence theory known as the closure problem (see, e.g., Pope 2000). A similar problem exists for the diffusivity term, which is discussed in more details in Section 2.2. We will adopt the commonly used eddy-diffusivity approximation to model the advection term in Section 7.

2.2. The Diffusivity Term

As shown in Pan & Scalo (2007) and PSS, the molecular diffusivity term in Equation (2), i.e., the first term on the right-hand side, is the only term responsible for the homogenization of the concentration fluctuations. The term can be rewritten as (see the Appendix)

$$-\frac{\partial}{\partial Z}\left(\langle\rho\rangle\Phi\left\langle\frac{1}{\rho}\frac{\partial}{\partial x_i}\left(\rho\gamma\frac{\partial C}{\partial x_i}\right)\,\middle|\, C=Z\right\rangle_\rho\right)$$
$$=\frac{\partial}{\partial x_i}\left\langle\rho\gamma\frac{\partial\phi}{\partial x_i}\right\rangle-\frac{\partial^2}{\partial Z^2}\left(\langle\rho\rangle\Phi\left\langle\gamma\left(\frac{\partial C}{\partial x_i}\right)^2\,\middle|\, C=Z\right\rangle_\rho\right), \quad (4)$$

where the first term on the right-hand side is a spatial diffusion of the fine-grained concentration PDF (defined in Section 2) by the molecular diffusivity. As a divergence term, it conserves the global PDF and does not contribute to true homogenization. The second term can be thought of as an anti-diffusion process in concentration space, as the coefficient is negative definite. It continuously narrows the PDF toward the mean value. Unfortunately, this diffusivity term does not have an exact or closed form. As it involves concentration gradients, it is nonlocal and dependent on the two-point concentration PDF. Deriving an equation for the two-point PDF gives rise to terms that require knowledge of three-point statistics, and so on, leading to a chain of multipoint PDF equations similar to the BBGKY hierarchy in kinetic theory (Lundgren 1967; Dopazo & O'Brein 1974). Assumptions must be made to truncate the hierarchy to obtain a closed set of equations. This is the so-called closure problem. In PSS, we considered a number of closure models and showed that a class of models based on the convolution of the concentration PDF are particularly successful in fitting the simulation results for the pollution of pristine material in turbulent flows. One of these convolution models for closure of the diffusivity term was used in our earlier modeling of the primordial fraction (Pan & Scalo 2007). We will summarize these models in Section 3.

Although the diffusivity term lacks an apparent dependence on the velocity field, an efficient homogenization of the concentration field does rely on the existence of turbulent motions. The action of the diffusivity term is very slow at large length scales where the pollutants are injected, because the molecular diffusivity γ is usually tiny in most natural environments including the ISM. For example, Pan & Scalo (2007) estimated γ for the Galaxy's ISM, weighted by residence time in different phases of the neutral gas, of about 10^{20} cm^2 s^{-1}, with a corresponding diffusivity scale of $\simeq 0.06\,(L_{100}/v_{10})^{1/2}$ pc, where L_{100} is the galactic turbulence integral scale in units of 100 pc, and v_{10} is the turbulent rms velocity in units of 10 km s^{-1}. This is the scale to which turbulence must stretch the pollutants in order for mixing to occur. Therefore, mixing by molecular diffusivity is negligible in the absence of a velocity field. A turbulent velocity can act as a catalyst and significantly accelerate the mixing process. This implicit role of turbulence on scalar homogenization is through the dependence of the diffusivity term on the concentration gradients (see Equation (2)). By continuously stretching the pollutants, turbulence produces structures at smaller and smaller scales, resulting in an enormous increase in the concentration gradients. Once the structures reach a small scale called the diffusion scale, where molecular diffusivity operates faster than turbulent stretching, they are homogenized efficiently by the diffusivity term. This suggests that the mixing timescale is essentially determined by turbulent stretching, even though the velocity itself does not truly mix. It is the cooperation of molecular diffusivity and turbulent motions that gives a significant mixing efficiency.

2.3. The Source Term

The last term in Equation (2) is the source term, corresponding to the injection of new pollutants into the turbulent flow. In general, pollutants are any source materials with a composition pattern different from that in the existing flow. Thus, for mixing of heavy elements in the ISM of galaxies, the source term would include both ejecta from supernova and stellar winds and, if it exists, infall of low-metallicity or primordial gas. To evaluate the source term, it is actually not necessary to compute its conditional average form in Equation (2). Instead, it can be

estimated by directly considering the rate at which the pollutants are injected and how they affect the concentration PDF in the flow. For example, assuming that the supernova ejecta are nearly pure metals, the source term for the supernova contribution would take a delta function form at $Z = 1$ with a coefficient depending on the supernova rate, ejecta mass, etc. (see Section 6; Pan & Scalo 2007). On the other hand, a primordial infall would give a delta function at $Z = 0$. Therefore, the effect of continuous sources of primordial gas and new metals is to force spikes in the concentration PDF at small and large concentration values, respectively.

3. MODELING THE DIFFUSIVITY TERM

The primary goal of this study is to investigate how the diffusivity term in the PDF equation, representing the homogenization by molecular diffusivity catalyzed by turbulent motions, reduces the fraction of pristine material in a turbulent flow. To understand the fundamental physics, we consider an idealized problem: mixing of decaying scalars (i.e., $S(\mathbf{x}, t) = 0$) in statistically stationary and homogeneous turbulence. The initial scalar field is also assumed to be statistically homogeneous. Clearly, this idealized problem is much simpler than in a realistic galactic environment. However, the simplified setting is extremely useful for understanding the underlying physics. As discussed in Section 2, under the assumption of statistical homogeneity, the advection term vanishes and the PDF, $\Phi(Z; \mathbf{x}, t)$, is independent of $\mathbf{x}$ and is equivalent to that computed from the spatial fluctuations in a single realization. With these simplifications, the PDF equation becomes

$$\frac{\partial \Phi(Z;t)}{\partial t} = -\frac{\partial^2}{\partial Z^2}\left(\Phi\left\langle \gamma\left(\frac{\partial C}{\partial x_i}\right)^2 \middle| C = Z\right\rangle_\rho\right) \quad (5)$$

where we used Equation (4). The diffusivity term is the only term in the simplified PDF equation.

In analogy with the mixing of primordial gas in early galaxies, we set the initial condition of the decaying scalar to be bimodal, consisting of pure pollutants ($Z = 1$) and completely unpolluted flow ($Z = 0$). This corresponds to a double-delta function form for the initial concentration PDF,

$$\Phi(Z; 0) = P_0\delta(Z) + H_0\delta(Z - 1), \quad (6)$$

where P_0 and H_0 are the initial probabilities/fractions of pristine gas and pollutants, respectively, and $P_0 + H_0 = 1$ from normalization.

Before introducing closure models for the diffusivity term, we discuss the evolution of the concentration variance, which helps reveal the general physics of turbulent mixing. In terms of the density-weighted PDF, the average concentration with density weighting is written as $\langle Z\rangle \equiv \int Z\Phi(Z;t)dZ$, which is equal to $\langle\rho C\rangle/\langle\rho\rangle$. Similarly, the density-weighted variance is expressed as $\langle(\delta Z)^2\rangle \equiv \int(Z - \langle Z\rangle)^2\Phi(Z;t)dZ$, which is equivalent to $\langle\rho(\delta C)^2\rangle/\langle\rho\rangle$, with $\delta C = C - \langle\rho C\rangle/\langle\rho\rangle$ being the fluctuating part of the concentration field. Taking the second-order moment of Equation (5) yields $\partial_t\langle\rho(\delta C)^2\rangle = -2\langle\rho\gamma(\partial_i C)^2\rangle$, which can also be derived directly from the advection-diffusion equation using the assumption of statistically homogeneity (see PS10). We therefore have

$$\frac{d\langle(\delta Z)^2\rangle}{dt} = -\frac{\langle(\delta Z)^2\rangle}{\tau_{\rm m}}. \quad (7)$$

The mixing timescale, $\tau_{\rm m}$, is the ratio of the concentration variance to its dissipation rate,

$$\tau_{\rm m} = \langle\rho(\delta C)^2\rangle/(2\langle\rho\gamma(\partial_i C)^2\rangle). \quad (8)$$

Clearly, τ_m is the timescale for the variance decay, and thus also characterizes the rate at which the diffusivity term reduces the PDF width.

As discussed in Section 2, the mixing timescale, $\tau_{\rm m}$, depends on the rate of turbulent stretching, which produces concentration structures at small scales and feeds molecular diffusivity with large concentration gradients. In the classical phenomenology for turbulent mixing, the continuous production of small-scale structures is described as a cascade, in the sense that the process proceeds progressively faster toward smaller scales. The picture is similar to the cascade of kinetic energy. It predicts that the mixing timescale is determined mainly by the eddy turnover time at the scale where the pollutants are injected, but is insensitive to the small diffusion scale, where the molecular diffusivity acts to homogenize. The prediction has been confirmed by PS10 using simulated supersonic turbulent flows with solenoidal driving force. They found that, at all Mach numbers explored, the mixing time was close to the eddy turnover time at the pollutant injection scale, suggesting that the cascade picture, originally proposed for mixing in incompressible flows, is valid also for highly compressible turbulence.

PS10 also found that compressible modes in solenoidally driven supersonic turbulence do not make a significant contribution to the cascade of concentration structures to small scales. Compressible modes consist of both expansions and compressions. As passive scalars simply follow the flow motions, the compression events would decrease the length scale of the concentration structures, or equivalently increase the concentration gradients. This makes a contribution to enhance the mixing rate. On the other hand, the expansion events would cause the mixing process to slow down. The two opposite effects tend to counteract each other. However, they do not exactly cancel out, and the effect of compressions appears to win slightly. Using the density fluctuations as a measure for the strength of the compression events, PS10 found that, in solenoidally driven flows, the net contribution of compressible modes to the enhancement of the concentration gradients is much smaller than the solenoidal modes (see Section 5 of PS10). A limitation in the effect of compressible modes on mixing is that the squeezing effect by compressions is not continuous due to the gas pressure. It is likely that a compressed region would expand before being squeezed by a second compression event.

Such a limitation does not exist in the stretching by solenoidal modes, which operates continuous and unlimited by the gas pressure. The stretching effect by incompressible modes appears to be the primary "mixer" in the simulated flows with solenoidal driving at all Mach numbers. As a consequence, a useful measure for the mixing efficiency would be the fraction of energy contained in solenoidal modes in the inertial range of the flow, which is responsible for the cascade of passive scalars toward the diffusion scale. A statistical analysis of the simulated velocity fields by PS10 showed that the solenoidal energy fraction in the inertial range decreases with M for $M \lesssim 3$ and then saturates at an equipartition value of $2/3$ at $M \gtrsim 3$. This provides a satisfactory explanation for the behavior of the mixing timescale normalized to the flow dynamical time as a function of M. The normalized mixing timescale increases with M for $M \lesssim 3$ and saturates at larger M. This finding supports our argument above that compressible modes are less efficient at enhancing

mixing in solenoidally driven flows, and with a larger fraction of compressible energy in the inertial range, the mixing is slower.

It remains to be checked if the normalized timescale as a function of M has the same behavior in supersonic turbulence with completely compressive driving. One issue is that, quantitatively, the energy fraction of solenoidal or compressible modes at inertial-range scales as a function of M in fully developed flows with compressive driving may be different from the solenoidal case. Second, as shown in Federrath et al. (2010), at the same M, the density fluctuations in a compressively driven flow are much stronger. This implies that the net effect of compressible modes on amplifying the concentration gradients would be more efficient than in the solenoidal driving case. If the contribution from compressible modes to the mixing efficiency in highly supersonic compressively driven flows is comparable to or even faster than the solenoidal modes, the behavior of $\tau_{\rm m}$ as a function of M may be qualitatively different, with the normalized timescale decreasing with M at sufficiently high M. On the other hand, if compressible modes in supersonic flows with compressive driving are still less efficient at enhancing mixing than solenoidal modes, one may expect a similar behavior for the normalized mixing timescale. We will investigate these possibilities in a future work.

3.1. Self-convolution PDF Models

A variety of closure models have been developed for the diffusivity term in the PDF equation. PSS considered several existing models from the literature, including the mapping closure model (Chen et al. 1989), based on an approximation for the exact but unclosed form of the diffusivity term, and a class of models, referred to as self-convolution models by PSS, based largely on a physical picture of the turbulent mixing process (Curl 1963; Dopazo 1979; Janicka et al. 1979; Venaille & Sommeria 2007; Villermaux & Duplat 2003; Duplat & Villermaux 2008). One of the self-convolution models was used in the initial study of pollution of pristine gas by Pan & Scalo (2007). By a detailed comparison with numerical simulations of turbulent mixing in two compressible flows at Mach 0.9 and 6.2, PSS showed that the convolution models provide both clear physical insights and successful fitting functions for the decay of the pristine mass fraction. Here, we give a brief introduction of the convolution models, and refer the interested reader to PSS for details.

There has been compelling evidence that the dominant scalar structures at small scales are two-dimensional sheets or edges (e.g., Pan & Scannapieco 2011 and references therein). The rate at which the scalar sheets are produced is determined mainly by the turbulent stretching rate at large length scales. With time, the sheets become thinner, and once the thickness of the sheets is sufficiently small for molecular diffusivity to efficiently operate, the neighboring sheets are homogenized, leading to a reduction in the PDF width.

The physical picture outlined above can be approximately described by an integral equation for the concentration PDF,

$$\frac{\partial\Phi(Z;t)}{\partial t}=s(t)\left(\int_0^1\Phi(Z_1;t)\int_0^1\Phi(Z_2;t)\delta\left(Z-\frac{Z_1+Z_2}{2}\right)\times dZ_1dZ_2-\Phi(Z;t)\right), \quad (9)$$

where Z_1 and Z_2 denote the concentrations in two nearby sheets prior to the mixing by molecular diffusivity, and the delta function in the integrand arises from the assumption that a perfect homogenization occurs instantaneously once two scalar sheets are sufficiently stretched for molecular diffusivity to take effect. Here, $s(t)$ is the turbulent stretching rate that controls the rate at which the PDF convolution proceeds. The second term on the right-hand side is the "destruction" of the previous PDF due to the mixing event. Using the properties of delta functions, Equation (9) can be written as $\partial_t\Phi(Z;t)=s(t)[2\int_0^1\Phi(Z';t)\Phi(2Z-Z';t)dZ'-\Phi(Z;t)]$, which shows that turbulent mixing is essentially assumed to be a self-convolution process.

For a reason to be clarified soon, Equation (9) was referred to as the discrete convolution model in PSS. It was first proposed by Curl (1963) in a study of droplet interactions in a two-liquid system, and was later extended to model mixing in turbulent flows (Dopazo 1979; Janicka et al. 1979). Several variants and generalizations of Equation (9) have been proposed to solve the problems of the model for turbulent mixing. One problem of Curl's model is that, for a double-delta initial PDF (Equation (6)), it produces unphysical spikes in between the initial delta functions. In order to avoid this, Dopazo (1979) and Janicka et al. (1979) suggested replacing the delta function in Equation (9) by a general function, $J(Z;Z_1,Z_2)$, that is smooth in between Z_1 and Z_2. PSS showed that, with this modification, the model gives essentially the same prediction for the evolution of the pristine mass fraction. Another weakness of the convolution PDF models with double integral equations is that, for mixing in incompressible flows, they substantially overestimate the PDF tails at late times (Kollmann 1990). However, the model offers an insightful picture for the mixing of pristine gas and provides useful fitting functions to the pristine fraction decay in certain physical regimes.

More recently, Venaille & Sommeria (2007) developed a "continuous" version of the self-convolution model, based on an extension of the Curl (1963) model in Laplace space. We first define the Laplace transform, $\Psi(\zeta;t)$, of the concentration PDF as $\Psi(\zeta;t)=\int_0^\infty\Phi(Z;t)\exp(-Z\zeta)dZ$. Using the convolution theorem, the Laplace transform of Equation (9) reads

$$\frac{\partial\Psi(\zeta;t)}{\partial t}=s(t)[\Psi(\zeta/2;t)^2-\Psi(\zeta;t)]. \quad (10)$$

Rewriting Equation (10) in a difference form, we have $\Psi(\zeta;t+\delta t)=\epsilon\Psi(\zeta/2;t)^2+(1-\epsilon)\Psi(\zeta;t)$, where $\epsilon=s(t)\delta t$, with δt being an infinitesimal time step. The difference equation has the following interpretation: during a time step δt, mixing occurs in an infinitesimal fraction, ϵ, of the flow, and in this fraction of the flow the scalar PDF undergoes a convolution. This suggests that in Curl's model the PDF convolution occurs locally in space. Also note that, whenever a mixing event occurs, it appears as a single complete convolution in the model, and in this sense the convolution process is "discrete."

The continuous-convolution model essentially assumes that the convolution occurs everywhere in the flow at any given time, but in an infinitesimal time, the number of convolutions is infinitesimal and equal to ϵ (Duplat & Villermaux 2008). The assumption can be represented by $\Psi(\zeta;t+\delta t)=\Psi(\zeta/(1+\epsilon);t)^{(1+\epsilon)}$. The Taylor expansion of this equation gives $\Psi(\zeta/(1+\epsilon);t)^{(1+\epsilon)}\simeq\Psi(\zeta;t)+\epsilon[\Psi(\zeta;t)\ln(\Psi(\zeta;t))-\zeta\partial\Psi(\zeta;t)/\partial\zeta]$. Taking the limit $\delta t\to 0$, we obtain

$$\frac{\partial\Psi(\zeta;t)}{\partial t}=s(t)\left[\Psi\ln(\Psi)-\zeta\frac{\partial\Psi}{\partial\zeta}\right]. \quad (11)$$

The equation was first derived by Venaille & Sommeria (2007), who showed that the predicted PDF evolves toward Gaussian in the long time limit. In the continuous version, the PDF convolution occurs globally in space. The model prediction has been tested against experimental results by Venaille & Sommeria (2008). Similar to Curl's model, the continuous model cannot be applied to predict the evolution of the entire PDF right at the beginning if the initial PDF is a double-delta function (Venaille & Sommeria 2007). Fortunately, for the problem of pristine gas pollution, the model provides a useful prediction that works immediately from the initial time (PSS).

A more general extension of the self-convolution model in Laplace space was given in Duplat & Villermaux (2008),

$$\frac{\partial \Psi(\zeta;t)}{\partial t} = s(t)n\left[\Psi\left(\frac{\zeta}{1+1/n};t\right)^{(1+1/n)} - \Psi(\zeta;t)\right]. \quad (12)$$

With $n = 1$ and in the limit $n \to \infty$, the equation becomes Equation (10) for Curl's original model and Equation (11) for the model of Venaille & Sommeria (2007), respectively. In deriving Equation (12), it was assumed that a fraction, $n\epsilon$, of the flow experiences mixing/convolution events during a time interval δt, and the number of convolutions in this fraction of the flow is $1/n$. From the discussion above for Curl's model and its continuous version, n characterizes the degree of spatial locality of the PDF convolution. Larger values of n correspond to more "global" convolutions in the spatial space, and the parameter n may be a function of time in general.

Equation (12) was referred to as the generalized convolution model in PSS, where we found that with increasing n the tails of the predicted PDFs become narrower. For example, the discrete model with $n = 1$ predicts exceedingly fat PDF tails, while in the continuous model ($n \to \infty$), the PDF approaches Gaussian at late times. In other words, more "global" PDF convolutions produce narrower PDF tails.

Finally, we point out that self-convolution models were not originally intended for mixing in highly compressible flows and they do not directly account for how compressible modes and the density fluctuations in supersonic turbulence may affect the concentration PDF. The diffusivity term in the PDF equation (see Equation (5)) has a dependence on the density field, suggesting that the flow compressibility may have potentially important effects on the PDF evolution. To our knowledge, the effect of compressibility has not been investigated in existing PDF models for turbulent mixing. Here, we take the following approach: we compare the predictions of the convolution models for the primordial fraction against simulation results, and examine whether, by adjusting their parameters, they can be applied to study the pristine gas pollution in supersonic turbulence. Indeed, we find that, by varying the parameter n, the self-convolution models give satisfactory predictions for the pollution of pristine gas in turbulent flows at different degrees of compressibility. Nevertheless, new closure models are strongly motivated to directly and explicitly address the effects of shocks and flow compressibility on the scalar PDF in supersonic turbulence.

3.2. Mass Fraction of Pristine Gas

The pristine fraction, defined as the mass fraction of the interstellar gas with metallicity smaller than the critical value, Z_c, can be evaluated from the concentration PDF by $P(Z_c, t) = \int_0^{Z_c} \Phi(Z', t) dZ'$. The fraction can be calculated easily if the PDF evolution is known. The threshold metallicity, Z_c, for the transition to Pop II star formation is small but finite, in the range from 10^{-8} to 10^{-5} by mass (see Bromm & Yoshida 2011; Schneider et al. 2012, and references therein). We also consider the fraction, $P(t)$, in the limit of an infinitesimal threshold, i.e., $P(t) = \lim_{Z_c \to 0} P(Z_c, t)$, which corresponds to the mass fraction of exactly metal-free gas. Clearly, the fraction $P(t)$ is zero unless the concentration PDF, $\Phi(Z; t)$, has a delta function component at $Z = 0$. Equations of $P(t)$ can be exactly derived from the self-convolution models in Section 3.1.

There is a subtle issue about the decay of the exactly metal-free fraction, $P(t)$, and the pristine fraction, $P(Z_c, t)$, with a finite threshold. PSS pointed out that the nonlocal nature of the Laplacian operator in the molecular diffusivity term leads to an essentially instantaneous decrease of $P(t)$. Physically, a tiny but finite fraction of the pollutant atoms can have extremely fast thermal speed, corresponding to the high tail of the Maxwellian distribution, and may reach and pollute the pristine gas at large distances in a short time. Even though the degree of pollution by these atoms at large distances is negligibly tiny, they do reduce the mass of gas that is *exactly* metal free, and this occurs at a timescale much shorter than the sound crossing time. Therefore, with the molecular diffusivity alone, $P(t)$ would decrease to zero almost instantaneously, regardless of the amplitude of the molecular diffusivity γ. On the other hand, it takes a finite time for the molecular diffusivity to enrich the entire flow up to a finite threshold Z_c. In fact, the decay of $P(Z_c, t)$ with Z_c, say, $\simeq 10^{-8}$ by molecular diffusivity alone is very slow because γ is typically tiny, $\simeq 10^{20}$ cm^2 s^{-1} in Galactic neutral ISM (see Pan & Scalo 2007). An efficient mixing rate relies on the presence of turbulent motions.

An ideal model for the pollution of pristine gas should accurately capture both the rapid decay of $P(t)$ and the evolution behavior of $P(Z_c, t)$. However, none of the models considered in PSS satisfy both constraints. For example, the mapping closure model by Chen et al. (1989) does predict an instantaneous decay of $P(t)$, but a comparison with simulation results shows that its prediction for $P(Z_c, t)$ is poor in general, especially in highly supersonic flows. On the other hand, the convolution PDF models introduced in Section 3.1 do not reduce $P(t)$ to zero immediately, instead the delta function component at $Z = 0$ remains finite at any finite time. This is inconsistent with the expectation of an instantaneous reduction of $P(t)$, and the reason is that the Laplacian operator in the molecular diffusivity term was not directly incorporated in these models. Despite this inconsistency, PSS found a very interesting result: the evolution equations of $P(t)$ derived from the convolution models provide excellent fitting functions for the simulation results for the decay of the pristine fraction $P(Z_c, t)$ with a small but finite threshold.

Here, we take the same approach as PSS and carry out a more systematic parameter study required to accurately span the range of astrophysical environments of interest. We will use the $P(t)$ equations from the convolution models to fit the simulation results for $P(Z_c, t)$ with different thresholds, Z_c, for scalars with different initial conditions evolving in a number of turbulent flows. This systematic procedure gives best-fit parameters in the convolution models as functions of Z_c, the initial pollutant conditions, and the flow Mach number. The numerically tested $P(t)$ equations with the best-fit parameters then provide a new tool to model the pollution of the primordial gas and the transition from Pop III to Pop II star formation in early galaxies.

We derive the equations of $P(t)$ from the convolution models using the PDF equations in Laplace space. Since the delta function at $Z = 0$ persists in these models, we decompose the concentration PDF into two terms,

$$\Phi(Z; t) = P(t)\delta(Z) + \Phi_e(Z; t), \tag{13}$$

where $P(t)$ is the fraction of exactly metal-free gas, and $\Phi_e(Z; t)$ is the concentration PDF in the enriched part of the flow, which satisfies the condition $\lim_{Z\to 0} \int_0^Z \Phi_e(Z'; t)dZ' = 0$. The Laplace transform of Equation (13) gives

$$\Psi(\zeta; t) = P(t) + \Psi_e(\zeta; t), \tag{14}$$

where $\Psi_e(\zeta; t)$ is the Laplace transform of $\Phi_e(Z; t)$. From the condition $\lim_{Z\to 0} \int_0^Z \Phi_e(Z'; t)dZ' = 0$, we have $\Psi_e(\zeta; t) \to 0$ in the limit $\zeta \to +\infty$.

Inserting Equation (14) to the PDF Equation (12) for the generalized convolution model and taking the limit $\zeta \to +\infty$ yields

$$\frac{dP}{dt} = -\frac{n}{\tau_{con}} P(1 - P^{1/n}). \tag{15}$$

For later convenience, we have replaced the turbulent stretching rate, s, by a "convolution" timescale $\tau_{con} \equiv s(t)^{-1}$.

Setting $n = 1$ in Equation (15), we obtain the equation of $P(t)$ for Curl's model,

$$\frac{dP(t)}{dt} = -\frac{1}{\tau_{con}} P(1 - P), \tag{16}$$

which was first given in Pan & Scalo (2007). An alternative derivation of this equation from the PDF equation in the double integral form is presented in PSS. From Equation (16), we see an interesting and simple physical picture for the pollution of the pristine gas by turbulent mixing: the primordial fraction is reduced when the fluid elements that are exactly metal free and the rest of the flow that has been polluted by sources or previous mixing events are brought close enough by turbulent stretching for the molecular diffusivity to homogenize. Taking $n \to \infty$, Equation (15) becomes

$$\frac{dP(t)}{dt} = \frac{P \ln(P)}{\tau_{con}}, \tag{17}$$

which is the prediction of the continuous-convolution model of Venaille & Sommeria (2007) for the pristine faction evolution.

Assuming that both n and τ_{con} are constant with time, Equation (15) has an analytic solution,

$$P(t) = \frac{P_0}{\left[P_0^{1/n} + \left(1 - P_0^{1/n}\right) \exp(t/\tau_{con})\right]^n}, \tag{18}$$

where P_0 is the initial pristine fraction. This equation becomes

$$P(t) = \frac{P_0}{P_0 + (1 - P_0) \exp\left(\frac{t}{\tau_{con}}\right)}, \tag{19}$$

for Curl's "discrete" model with $n = 1$ and

$$P(t) = P_0^{\exp(t/\tau_{con})}, \tag{20}$$

for the Venaille & Sommeria (2007) model with $n \to \infty$.

These convolution models predict that the pollution of primordial gas in turbulent flows proceeds at a timescale $\tau_{con} \simeq s^{-1}$, which is essentially the timescale of turbulent stretching at large scales, anticipated by the cascade picture for turbulent mixing. Also note that the pollution timescale is essentially independent of the molecular diffusivity γ. Again, this is because the mixing rate is largely controlled by how fast the velocity field produces and feeds fine structures to the molecular diffusivity, but insensitive to the diffusion scale at which molecular diffusivity operates.

4. NUMERICAL SIMULATIONS

To calibrate n and τ_{con} as a function of the flow and pollutant properties, we carried out numerical simulations for mixing in compressible turbulence using the FLASH code (version 3.2), a multidimensional hydrodynamic code (Fryxell et al. 2000) that solves the Riemann problem on a Cartesian grid using a directionally split piecewise parabolic method (Colella & Woodward 1984; Colella & Glaz 1985; Fryxell et al. 1989). The hydrodynamic equations were evolved in a periodic box of unit size with 512^3 grid points. Simulation runs at a lower resolution (256^3) were also conducted to check the potential effect of numerical diffusion. An isothermal equation of state with unit sound speed was adopted in all our simulations. The turbulent flows were driven and maintained at a steady state by a large-scale solenoidal external force, which was set be a Gaussian stochastic vector that decorrelates exponentially with a timescale equal to a quarter of the sound crossing time. The driving force was generated in Fourier space, and it included all independent modes with wavenumbers in the range from 2π to 6π. Each mode was given the same amount of power. We defined a characteristic driving length scale $L_f \equiv \int (2\pi/k)\mathcal{P}_f(k)d\mathbf{k}/\int \mathcal{P}_f(k)d\mathbf{k}$, where $\mathcal{P}_f(k)$ is the power spectrum of the driving force. Calculating L_f from our forcing spectrum, we found $L_f = 0.46$ in units in which the box size is unity. By adjusting the amplitude of the driving force, we simulated four flows with different (density-weighted) rms velocities, v_{rms}. For each flow, we defined a dynamical timescale, $\tau_{dyn} \equiv L_f/v_{rms}$, and all the simulation runs lasted for about 5 τ_{dyn}. We computed the mean rms velocity by a temporal average after each flow reached a steady state, and the rms Mach numbers, M, i.e., the ratio of the rms velocity to the sound speed, in the four flows were $M = 0.9$, 2.1, 3.6, and 6.2, respectively. The simulation setup for the turbulent velocity field is the same as in PS10 and PSS to which we refer the interested reader for details.

To study turbulent mixing, we evolved a number of decaying scalar fields in the four simulated flows. In each flow, we solved the advection equations of all scalar fields starting at the same time after the flow had already become fully developed and statistically stationary. The initial condition of the scalar fields was taken to be bimodal, consisting of pure pollutants and completely unpolluted material only. Such a bimodal field was obtained by setting the pollutant concentration, C, to unity in selected regions, representing pure pollutants, and to zero in the rest of the simulation box, corresponding to the unpolluted flow. The rate at which the pollution of the pristine material proceeds in our simulations depends not only on the flow properties but also on the initial configuration of the pollutants. Two parameters in the initial condition are of particular interest. The first one is the initial pollutant fraction, H_0, defined as the ratio of the heavy element mass to the total flow mass in the simulation box. The fraction is related to the initial primordial fraction, P_0, by $P_0 + H_0 = 1$. Obviously, with more pollutants

Table 1
Initial Configuration of Passive Scalar Fields Evolved in Our Simulated Turbulent Flows

Category	Pollutant Configuration	$H_0 = 0.5$	$H_0 = 0.1$	$H_0 = 10^{-2}$	$H_0 = 10^{-3}$
i	1 cube	iA	iB	iC	iD
ii	1 ball	iiA	iiB	iiC	iiD
iii	2^3 balls	iiiA	iiiB	iiiC	iiiD
iv	4^3 balls	ivA	ivB	ivC	ivD
v	8^3 balls	vA	vB	vC	vD

in the flow, i.e., a larger value of H_0, one would expect a faster pollution of the pristine gas.

The mixing/pollution timescale also depends on how the pollutants are spatially distributed in the flow. For illustration, let us consider two different distribution patterns for the same amount of pollutants. In the first pattern, the pollutants are released in the form of a single blob, while in the second, the pollutants are divided into many blobs of similar sizes evenly distributed in the flow. Intuitively, the pollution process would be considerably faster in the latter case. In that case, the pollution injection scale, $L_{\rm p}$, which is essentially the average distance between the pollutant locations, is smaller, and the mixing timescale should be shorter since it is determined by the eddy turnover time at $L_{\rm p}$ (PS10). We thus expect that a smaller $L_{\rm p}$ would result in a faster decay of the pristine mass fraction, and we will quantitatively examine the dependence of the pollution of the pristine flow on this parameter. In the context of the mixing of heavy elements in the ISM of early galaxies, the pollutant fraction, H_0, is related to the number or the rate of the supernova events, and the pollutant injection scale corresponds to the average distance between the explosion locations.

In order to conduct a systematic study of the parameter dependence of P, we included in each simulated flow a total of 20 scalar fields with different initial conditions. Table 1 summarizes the fields, which are divided into five categories based on the geometry and the spatial distribution of the pollutants. For categories i and ii, the initial pollutant configuration is a single blob located right at the center of the simulation box, and the geometrical shape of the blob was set to be a cube and a spherical ball, respectively. Clearly, for a single pollutant blob, the pollutant separation and hence the injection length scale, $L_{\rm p}$, is given by the box size. Considering that the flow driving scale $L_{\rm f}$ in our simulations is 0.46 of the box size, we have $L_{\rm p} \simeq 2\,L_{\rm f}$ for categories i and ii. In the other three categories, the pollutants are divided into identical spherical blobs, equally spaced in the simulation box. The number of blobs is 8, 64, and 512, respectively, for categories iii, iv, and v. For scalar fields in these three categories, $L_{\rm p}$ corresponds to 1/2, 1/4, and 1/8 box size (or equivalently $\simeq$1, 0.5, and 0.25 $L_{\rm f}$), respectively. For reference, the scale at which the energy cascade and hence the inertial range starts in our simulated flows is about one-fourth of the box size. The injection scale (one-eighth of the box size) of category v scalar fields is well within the inertial range.

There are four scalar fields in each category, which differ in the initial pollutant mass fraction, H_0. The four scalar fields in category i, named iA, iB, iC, and iD, have $H_0 = 0.5$, 0.1, 0.01, and 0.001, respectively. Scalar fields in other categories are named in the same way. These exact H_0 values were achieved by tuning the size of the pollutant blob(s). In category i, the length of the pollutant cube is set to 0.79, 0.47, 0.22, and 0.1 in units of the box size, or 1.7, 1.0, 0.48, and 0.22 in units of the driving scale $L_{\rm f}$, for scalars A, B, C, and D, respectively, in the Mach 0.9 flow. For the four scalars in category ii, the radius, $r_{\rm p}$, of the spherical ball is 0.49, 0.29, 0.14, and 0.063 box size. In units of $L_{\rm f}$, $r_{\rm p} = 1.1$, 0.63, 0.30, and 0.14 $L_{\rm f}$, respectively. The radius of each pollutant ball for the corresponding scalar in categories iii, iv, and v is smaller by a factor of two, four, and eight, respectively, than the $r_{\rm p}$ value for category ii. This is because the numbers of balls in those categories are larger than that in category ii by factors of 8, 64, and 512. The radii $r_{\rm p}$ given here are the values used in the $M = 0.9$ flow. At larger M, $r_{\rm p}$ for each corresponding scalar is slightly different. Due to significant density fluctuations in flows at higher M, using pollutant blobs of the same size at the same locations leads to different values of H_0. We thus tuned the pollutant size to guarantee that the initial pollutant *mass* fraction, H_0, is exactly 0.5, 0.1, 0.01, and 0.001 for the scalars in each flow.

We also made an attempt to investigate a smaller value (10^{-4}) of H_0, which would also be interesting for mixing in the ISM of early galaxies. However, a tiny H_0 corresponds to a small pollutant size, and due to the limited numerical resolution, the pollutant size for $H_0 = 10^{-4}$ is too close to the resolution scale of our simulations. In that case, numerical diffusion took effect and significantly polluted the surrounding flow from the beginning, leading to a different evolution behavior for the pristine fraction at early times than the other cases with $H_0 \geqslant 10^{-3}$. In the ISM, the pollutant size is essentially a supernova remnant stall diameter, $\simeq$150 pc, with little dependence on parameters (see Thornton et al. 1998; Hanayama & Tomisaka 2006). This is expected to lie within the inertial range of interstellar turbulence. Therefore, the real homogenization of fresh metals from supernovae by molecular diffusivity must wait for turbulent stretching to bring the concentration structures to the diffusion scale, which is tiny in comparison to the remnant size. It is thus appropriate to consider pollutants with initial sizes significantly larger than the diffusion/resolution scale of the turbulent flow, and in the present work we do not explore scalar cases with $H_0 \leqslant 10^{-4}$. We point out that the first three scalar fields in category i, i.e., iA, iB, and iC, in Mach 0.9 and 6.2 flows have been studied in details in PSS. In this paper, we perform a more systematic study covering a much larger parameter space.

Neither the viscous term in the hydrodynamic equations nor the diffusivity term in the advection-diffusion equation were explicitly included in our code. Therefore, both kinetic energy dissipation and scalar homogenization (or dissipation) are through numerical diffusion in our simulations. The diffusion scale where the scalar homogenization occurs is close to the resolution scale, and so is the energy dissipation or the Kolmorgorov scale. To examine whether our results for primordial gas mixing depend on the amplitude of numerical diffusion, we also performed simulations at the resolution of 256^3, and the results at the two resolutions are compared in Section 5.4.5. Otherwise, unless explicitly stated, the results reported below are from the 512^3 simulations.

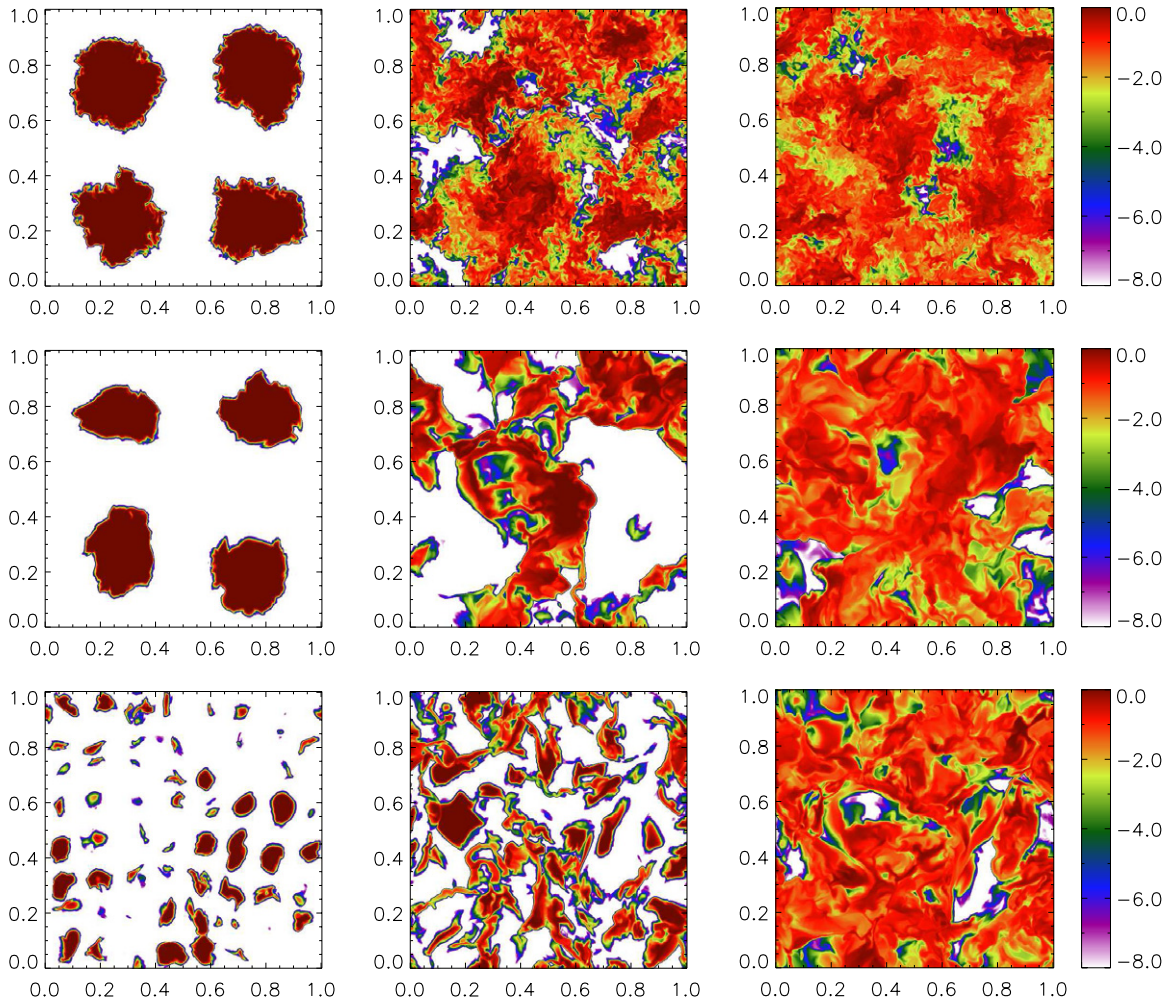

Figure 1. Evolution of the concentration fields of three scalars on a slice of the simulation grid. The color scale for the concentration field is logarithmic with white regions representing the unpolluted flow with $C \leqslant 10^{-8}$. From left to right, the top three panels show snapshots of scalar field iiiB in the Mach 0.9 flow at $t = 0.11$, 0.68, and 1.06 $\tau_{\rm dyn}$. The density-weighted scalar variances at these times are 0.086, 0.038, and 0.015, respectively. The initial condition of this scalar field is eight equally spaced blobs with a total pollutant fraction $H_0 = 0.1$. The central three panels plot a scalar field with the same initial condition but in the highly supersonic flow with $M = 6.2$. The three snapshots correspond to $t = 0.11$ (left), 0.76 (mid), and 1.41 $\tau_{\rm dyn}$ (right), with the scalar variance being 0.078, 0.023, and 0.006, respectively. The bottom panels show case vB in the Mach 6.2 flow. This scalar field initially consists of 512 pollutant blobs, and the total pollutant fraction H_0 is also equal to 0.1. At $t = 0$, 64 blobs lie on the selected slice, and the three snapshots are taken at $t = 0.11$, 0.33, and 0.76 $\tau_{\rm dyn}$. At these snapshots, the scalar variance is 0.07, 0.038, and 0.011, respectively.

(A color version of this figure is available in the online journal.)

5. RESULTS

5.1. The Concentration Field

In Figure 1, we show the concentration on a slice (on the y–z plane at $x = 0.25$) of the simulation grid for three scalar fields (rows) at three different times (columns). The concentration is plotted on a logarithmic scale with the white color representing concentration levels below 10^{-8}. The top three panels, from left to right, correspond to case iiiB in the Mach 0.9 flow at $t = 0.11$, 0.68, and 1.06 $\tau_{\rm dyn}$, respectively. At $t = 0$, four spherical pollutant blobs lie on the $x = 0.25$ plane. With time, turbulence stretches and spreads out the pollutants, and structures at small scales are continuously produced. In particular, we observe prominent "cliff" structures with sharp concentration gradients. These sheet-like structures are typical of passive scalars in incompressible turbulence (e.g., Watanabe & Gotoh 2004). As the length scale of the scalar structures reaches the (numerical) diffusion scale, mixing occurs between the pollutants/polluted flow and the pristine regions. The mixing process reduces the volume fraction of the pristine flow (white regions), and at 1.06 $\tau_{\rm dyn}$ almost the entire flow is polluted. The density-weighted concentration variance decreases from the initial value of 0.09 to 0.086, 0.038, and 0.015, respectively, for the three snapshots from the left to the right.

The three panels in the second row show snapshots of the same scalar case iiiB, but in the Mach 6.2 flow, at $t = 0.11$ (left), 0.76 (mid), and 1.41 $\tau_{\rm dyn}$ (right), respectively. Comparing with the top panels, we see that, even at later times (in units of $\tau_{\rm dyn}$), the surviving pristine volume is larger than in the $M = 0.9$ flow, suggesting that the pollution of the pristine gas is slower in turbulent flows at higher M. The concentration field appears to be smoother than in the $M = 0.9$ flow. As explained in detail in PS10, this is because in highly supersonic turbulence the visual impression of the scalar field is dominated by expansion events, which occupy most volume of the flow domain. Since a passive scalar simply follows the flow velocity, an expanding region tends to produce coherent and smooth structures at large

scales. We note that the scalar in the supersonic flow has a smoother appearance also at small scales, and the likely reason is that the code used in our simulations applies a larger effective numerical diffusion to stabilize stronger stocks in flows with larger M. Although compressible modes play a key role in shaping the large-scale geometry of the scalar field, the primary mixing agent is still stretching by solenoidal modes even in our simulated flows at very high M (PS10). The concentration variances at the three snapshots shown here are 0.078, 0.023, and 0.006, respectively. Note that, even though the scalar variances in the right two panels are smaller than the corresponding snapshots in the $M = 0.9$ flow, the remaining pristine fraction in the $M = 6.2$ flow appears to be larger. This is because in turbulent flows with higher M the scalar PDF tails are broader, leading to a larger pristine fraction at the same concentration variance. A more detailed discussion on this issue is given in Section 5.2.

The bottom three panels in Figure 1 plot the evolution of the scalar field vB in the Mach 6.2 flow, which also has $H_0 = 0.1$. Unlike case iiiB shown in the top and central panels, this field initially consists of 512 small blobs, and has a smaller injection scale, L_p. At $t = 0$, 64 blobs lie on the slice shown here. At early times, some blobs appear to be small dots or filaments because they are being advected out of the selected slice. The three panels correspond to $t = 0.11$, 0.33, and 0.76 τ_{dyn}. The mixing/pollution process proceeds much faster than case iiiB in the same flow. One reason is that, for a smaller pollutant size, turbulent stretching of the pollutant is faster, and thus mixing of each individual blob with the surrounding flow is more efficient. Also, since the separation between the pollutant blobs is small, the polluted/mixed regions by the individual pollutant blobs start to overlap quickly, resulting in a much faster erasure of the pristine flow material. As a reference, the scalar variances at the three snapshots from the left to the right are 0.07, 0.038, and 0.011, respectively.

5.2. The PDF Evolution

In this subsection, we discuss simulation results for the evolution of the concentration PDF. Figure 2 plots the PDF as a function of time for four scalar fields. For all scalars, the heights of the two spikes at $Z = 0$ and $Z = 1$ decrease at early times, and mixing causes a probability flux toward the central part, which gradually fills the concentration space between the two spikes. Both spikes are eventually removed, and for an initial PDF with negative skewness, or $P_0 > H_0$, the left spike lasts longer than the right one. At later times, a central peak forms around the mean concentration, and the PDF becomes unimodal. After that, the PDF continuously narrows toward the mean value, a process described in Section 2.2 as anti-diffusion in concentration space.

In PSS, we tested the predictions of various models for the PDF evolution against simulation data for scalar case iB in Mach 0.9 and 6.2 flows. The initial condition of this scalar is a single cubic pollutant with $H_0 = 0.1$. It was found to be very challenging for PDF models to accurately predict the scalar PDF tails, especially for scalar fields in highly supersonic flows. Here, we do not attempt to obtain successful model fits to the measured PDFs, as the main goal of this work is to understand the evolution of the pristine fraction, rather than the full details of the entire PDF. However, including a model prediction for the PDF evolution in our figure is useful, because it provides a guideline to compare the fatness of the PDF tails for different scalar fields in different flows. For this purpose, we consider the beta distribution function as a PDF model for passive scalar mixing, which has been shown to provide a good approximation for the PDF shape of decaying scalars with a double-delta initial condition in incompressible turbulence (e.g., Girimaji 1991). The beta distribution function is defined as

$$\Phi_\beta(Z) = \frac{\Gamma(\beta_1 + \beta_2)}{\Gamma(\beta_1)\Gamma(\beta_2)} Z^{\beta_1 - 1}(1 - Z)^{\beta_2 - 1}, \quad (21)$$

where Γ is the gamma function. To compare the beta distribution with the simulation results, one can determine the two parameters, β_1 and β_2, in Equation (21) by equating the mean and variance of the beta PDF to those measured from the simulation data. For each measured PDF (data points) shown in Figure 2, we plot a beta distribution (line), where the beta parameters are fixed using the concentration mean and variance at the corresponding time.

The left top panel in Figure 2 shows the result for case iiiB in the Mach 0.9 flow. The initial condition of this case is eight equally spaced spherical blobs with L_p equal to half of the box size. The total pollutant fraction, H_0, of this scalar field is 0.1. The PDFs are measured at five different times as indicated in the legend. For this scalar, the fitting quality of the beta distribution functions is generally good except at far tails. In PSS, we showed that, at later evolution times, the PDF of scalar iB in the $M = 0.9$ flow is well fit by a gamma distribution, as predicted by the PDF model of Villermaux & Duplat (2003). The initial condition of scalar iB is a single cubic pollutant, and it has a twice larger L_p than iiiB shown here. The performance of the Villermaux & Duplat (2003) model is less satisfactory for scalars with smaller L_p, e.g., it significantly underestimates the PDF tails for the scalars in Figure 2. Also, that model is invalid at the early evolution stage (see PSS). On the other hand, the beta distribution does provide acceptable fits to the measured PDFs at early times, as seen in Figure 2.

The top right panel shows the PDF of the same scalar field in the Mach 6.2 flow. Using the beta distributions as a reference, we see that at late times, the left PDF tails are broader than in the Mach 0.9 case. The bottom two panels plot the results for case vB in the same two flows. This scalar field also has $H_0 = 0.1$, but the injection scale, L_p, is significantly smaller, $\simeq 1/8$ of the box size (see Table 1). A comparison of the time series indicated by the legends in the top and bottom panels shows that the PDF variance decays much faster for scalar fields with smaller injection scale (see Section 5.3), but at similar values of the variance, the PDF tails are broader for scalar fields with smaller L_p. These observations are consistent with the findings of PS10, who studied the dependence of the PDF shape on M and L_p in details, and found that the PDF tails become broader with increasing M or decreasing L_p. The physical origin of this behavior is probably related to the phenomenon of turbulent intermittency, i.e., the existence of strong non-Gaussian velocity structures at small scales. Supporting this interpretation is the fact that the degree of non-Gaussianity of the velocity field increases as M increases or as L_p decreases, which coincides with the trend of the PDF tails of passive scalars. As discussed in Section 3.1, the convolution PDF models with smaller n predict fatter tails, meaning that n would decrease with increasing M or decreasing L_p if one attempts to fit the measured PDFs with the predictions of the convolution models. Extending the intermittency argument here to mixing in supersonic flows with totally compressive driving, we expect that, at the same M, the passive scalar PDF would have fatter tails than in our flows with

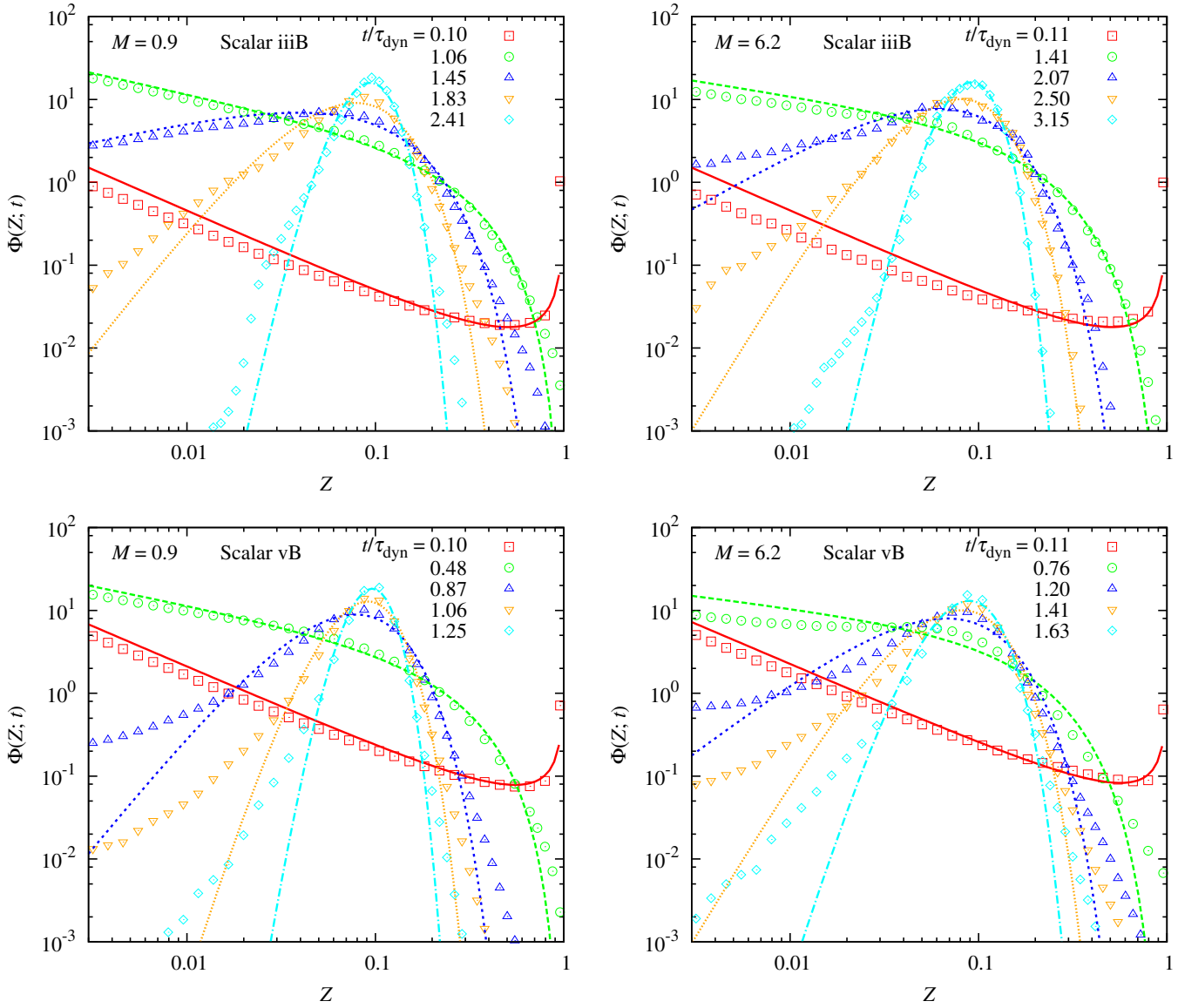

Figure 2. Density-weighted concentration PDFs of four scalar fields as a function of time. The left and right panels correspond to scalar fields advected in the Mach 0.9 and Mach 6.2 flows, respectively. Top and bottom panels show results for scalar fields in two different categories, iii and v. The initial pollutant separation for the two scalars is half and one-eighth of the box size, respectively. All scalar fields shown here have the same initial pollutant fraction $P = 0.1$, and thus their PDFs have the same mean (0.1). The lines are beta distribution functions with the same mean and variances as the corresponding PDFs measured from the simulations (data points).

(A color version of this figure is available in the online journal.)

solenoidal driving. This is because the compressively driven supersonic flows are significantly more intermittent (Federrath et al. 2010).

We point out that the fatness of the PDF tails as a function of M and L_p for decaying scalars in the current study is less clear-cut than for the forced scalars examined in PS10. The general trend is sometimes not clearly obeyed in our simulations here, especially for scalar fields in high Mach number flows ($M = 3.5$ and 6.2). For example, as seen in Figure 2, it appears that the PDF tail of scalar vB in the Mach 6.2 flow is less broad than in the Mach 0.9 flow. A possible reason is that the measurement of the PDFs of decaying scalars is less precise than in the case of forced scalars, for which the PDFs can be computed by averaging over many snapshots. Simulations with higher resolutions may help us establish a robust trend for the PDF tail of decaying scalars in turbulent flows at large M, as they provide better statistics and better resolution of complexities, such as strong density fluctuations, in highly supersonic turbulence.

Finally, we stress that the pristine fraction corresponds to the probability contained in the far left tail of the PDF with $Z < 10^{-8}$–10^{-5}, which is beyond the range of Z values shown in Figure 2. Nevertheless, the PDF tails shown in Figure 2 can be used to infer the trends of the pristine fraction with varying M and L_p. Since the PDF tail broadens with M, we would expect that, with the same concentration variance, the pristine fraction contained in the PDF would be higher for a scalar field evolving in a flow with higher Mach number or smaller pollutant injection scale. In fact, the dependence of the PDF tails on M and L_p induces interesting effects on the pristine fraction as a function of time, which will be discussed in detail in Section 5.4.

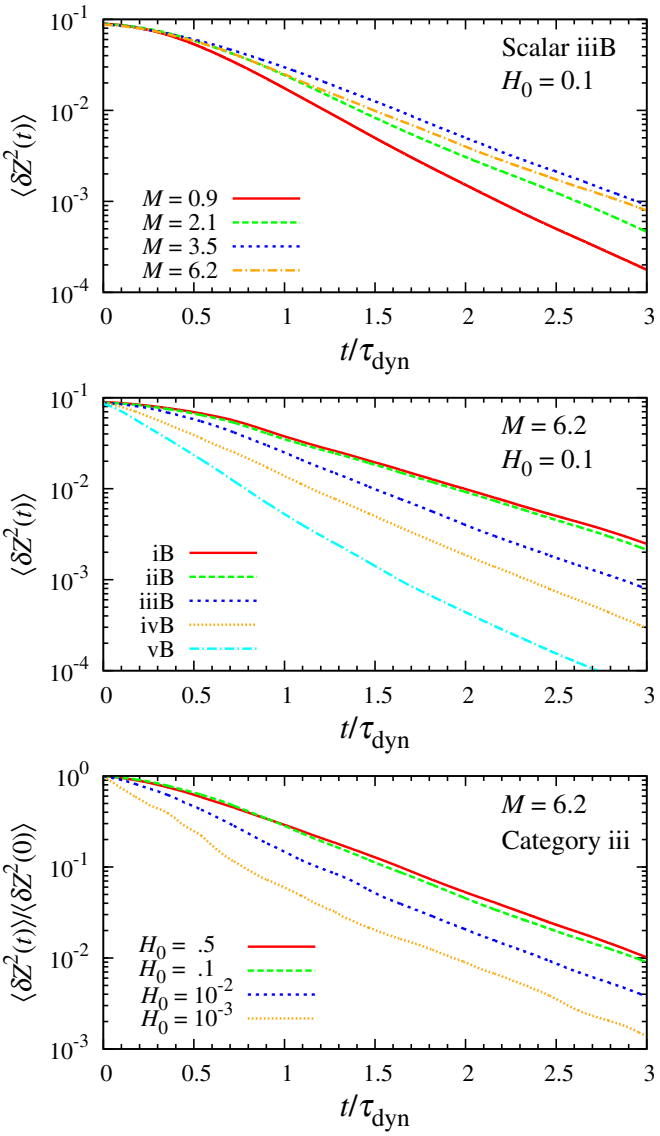

Figure 3. Density-weighted concentration variance as a function of time. Top panel: scalar field iiiB in four simulated flows with $M = 0.9$, 2.1, 3.5, and 6.2. The scalar field has a total pollutant fraction, H_0, of 0.1 and the injection length scale, $L_{\rm p}$, is $\simeq 1/2$ of the box size. Mid panel: B scalar fields ($H_0 = 0.1$) in the $M = 6.2$ flow. The five curves correspond to five categories in Table 1 with different pollutant shape and injection length scales. Bottom panel: scalar fields from category iii in the $M = 6.2$ flow. Each curve is for a different value of the initial pollutant fraction, and the variance of each scalar field is normalized to its initial value.

(A color version of this figure is available in the online journal.)

5.3. The Variance Decay

Figure 3 plots the variance decay of a number of scalar fields. The top panel shows the results for scalar fields iiiB in the four simulated flows at different M. For these scalar fields, $L_{\rm p} \simeq L_{\rm f}$, $H_0 = 0.1$, and the initial variance is 0.09. The variance decay first slows down with increasing Mach number, then becomes slightly faster as M increases from 3.5 to 6. The same behavior has been found in PS10, where a physical explanation was given (see also Section 3). In our simulated flows, compressible modes are inefficient in producing small-scale structures. Therefore, the mixing efficiency decreases as the fraction of kinetic energy contained in compressible modes at inertial-range scales increases. At $M \gtrsim 3$, this fraction saturates at an equipartition value of 1/3, and the mixing timescale becomes essentially constant. The slightly faster mixing as M increases to 6.2 is because of the effect of strong compression in our simulated flow with $M = 6.2$. Due to the limited numerical resolution, the strongest compression events in this flow can directly squeeze the scalar structures to the diffusion scale and provide some contribution to the mixing efficiency. As discussed in Section 3, the effect of compressible modes on mixing could be stronger in a highly supersonic flow with compressive driving, and the behavior of the normalized mixing timescale as a function of M in compressively driven flows will be studied in a future work. In Figure 3, we see that the variance decrease is approximately exponential. The mixing timescale $\tau_{\rm m}$ is measured to be 0.45, 0.48, 0.58, and 0.57 $\tau_{\rm dyn}$ for $M = 0.9$, 2.1, 3.5, and 6.2, respectively. The 20% increase in $\tau_{\rm m}$ as M goes from 0.9 to 6.2 is consistent with the results of PS10.

The middle panel of Figure 3 shows the variance of five B scalars in the $M = 6.2$ flow. Each case is from one of the five categories listed in Table 1, and they all have $H_0 = 0.1$. The curves for scalar fields iB and iiB are very close to each other. The initial pollutant distributions of these two scalar fields are a single cube and spherical ball, respectively, and the similarity of their variance decay suggests that the mixing timescale is essentially independent of the geometrical shape of the pollutants. On the other hand, the mixing timescale decreases steadily as the average pollutant separation becomes smaller. The injection scale, $L_{\rm p}$, for scalar fields iiiB, ivB, and vB is half, one-fourth, and one-eighth of the box size, respectively. We attempted to measure $\tau_{\rm m}$ by fitting the five curves with exponentials in the time interval from 0 to $\simeq 2\,\tau_{\rm dyn}$, which is the time range of primary interest for the pristine gas pollution (see Section 5.4). The measured values of $\tau_{\rm m}$ are 0.72, 0.71, 0.57, 0.48, and 0.34 $\tau_{\rm dyn}$, respectively, for the five curves from top to bottom. The mixing timescale is determined by the eddy turnover time at the pollutant injection scale, and thus decreases with decreasing $L_{\rm p}$. This physical picture also provides an explanation for the scale dependence of the mixing timescale found by de Avillez & Mac Low (2002) in a suite of numerical simulations of mixing in supernova-driven interstellar turbulence.

In the bottom panel, we plot the variance decay of four scalar fields from category iii in the Mach 6.2 flow. Different curves correspond to different values of H_0. Unlike the top two panels, here we normalize the concentration variance to its initial value, $\langle \delta Z^2(0) \rangle$, which makes it easier to compare the variance decay timescale of different scalars. For a double-delta PDF (Equation (6)), the initial variance $\langle \delta Z^2(0) \rangle$ is equal to $P_0 H_0 = P_0(1 - P_0) = H_0(1 - H_0)$. For $H_0 \leqslant 0.5$, $\langle \delta Z^2(0) \rangle$ decreases with decreasing H_0. This suggests that, for scalar PDFs close to a double-delta shape, the variance is not a good indicator of the pristine fraction, as the smaller variance for scalar fields with smaller H_0 in the bottom panel of Figure 3 actually corresponds to a larger pristine fraction. While a better indictor would be the variance normalized to the average concentration squared, which measures the rms of the fluctuations relative to the mean, the variance plot normalized to the initial value nevertheless provides useful information for the timescale of the mixing process.

With decreasing H_0, the radius of each individual pollutant blob becomes smaller, decreasing from about 0.5 of the box size ($H_0 = 0.5$) to only 0.06 of the box size ($H_0 = 10^{-3}$). The top two curves for $H_0 = 0.5$ and 0.1 are close to each other, and the reason is that, for these two scalar fields, both the pollutant

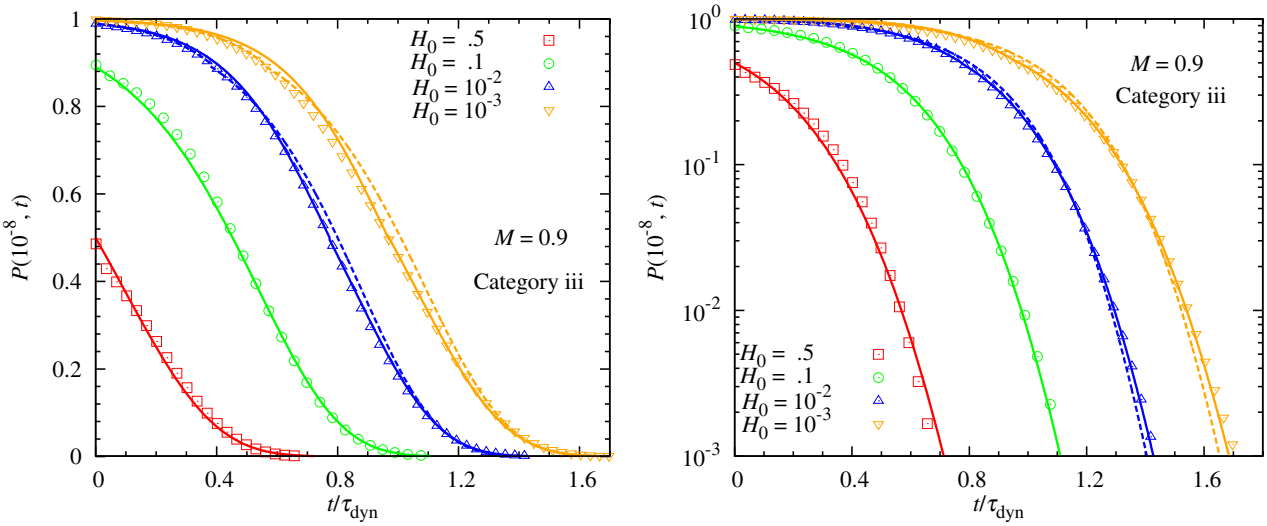

Figure 4. Pristine fraction, $P(10^{-8}, t)$, as a function of time for the four scalar fields from category iii in the Mach 0.9 flow. The left and right panels show the same plot but on a linear–linear and a linear–log scale, respectively. Lines are fitting functions based on the prediction of the self-convolution PDF models. For scalar fields iiiC ($H_0 = 0.01$) and iiiD ($H_0 = 0.001$), the dashed lines are obtained by a two-phase fitting that connects at $P(10^{-8}, t) = 0.9$, while the solid lines connect the two phases at $P(10^{-8}, t) = 0.5$. The fitting parameters are given in the text.

(A color version of this figure is available in the online journal.)

size and the pollutant separation are close to the flow driving scale, L_f, and the scale (one-fourth of the box size) at which the inertial range of the flow starts. The mixing timescales for these two scalar cases are thus given by the turnover time of large eddies of similar sizes. The situation is different for the rest two scalar fields. For $P \leqslant 0.01$, the size of each individual blob is significantly smaller than L_f. It is also smaller than the average separation, L_p ($\simeq L_f$), between the pollutant blobs. In this case, the mixing process around each blob is not synchronized with that over the entire flow. This divides the variance evolution into two phases. The early phase occurs faster and is controlled by the turbulent stretching rate at smaller scales (the pollutant size). This explains the faster variance decay for smaller H_0 at early times. After each blob is stretched, spread, and mixed to a size close to the average pollutant separation, the mixing process starts to proceed at a single pace, and the timescale is determined by the turnover time of eddies of size L_p. As seen in the bottom panel of Figure 3, the variance decay is exponential for all cases at late times with essentially the same timescale ($0.6\,\tau_{dyn}$). The existence of two phases for scalar fields with small H_0 also leaves a signature in the evolution of the pristine gas fraction.

5.4. The Pristine Fraction

5.4.1. General Results

We now present results for the decay of the pristine mass fraction in our simulated flows. In PSS, we have shown results for three scalar fields, iA, iB, and iC from category i (with $H_0 = 0.5$, 0.1, and 0.01, respectively; see Table 1), evolved in two flows with $M = 0.9$ and $M = 6.2$. The pollutant injection scale L_p of those fields was the box size, or about twice the flow driving scale L_f. In this section, we consider scalar fields in category iii in the $M = 0.9$ and 6.2 flows as primary examples. The injection scale of these fields is smaller, with $L_p \simeq L_f$. In the subsequent subsections, we will discuss in details the dependence of the pristine fraction decay on various parameters.

Figure 4 shows the mass fraction $P(10^{-8}, t)$ of the flow with concentration level below 10^{-8} for scalar fields iiiA, iiiB, iiiC, and iiiD in the $M = 0.9$ flow. The data points are simulation results, and the lines are fitting functions based on the predictions of the self-convolution PDF models discussed in Section 3.2. The left and right panels are the same figure on linear–linear and linear–log scales, respectively. The linear–linear scale shows the early evolution more clearly, while with a linear–log plot one can see the late-time behavior better. The initial pollutant fraction, H_0, of the four cases in this figure ranges from 0.5 (iiiA) to 10^{-3} (iiiD). As shown in PSS, the prediction, Equation (18), of the self-convolution models can successfully fit the simulation results for scalar fields with $H_0 \geqslant 0.1$. The fitting lines in Figure 4 for the two cases with $H_0 = 0.5$ and 0.1 are the predictions of the convolution models with $n = 10$. The initial pristine fraction P_0 in Equation (18) is set to 0.5 and 0.9, and the timescale τ_{con} is taken to be 0.27 and 0.25 τ_{dyn}, respectively. Both the linear–linear and the linear–log plots show that the model prediction matches the simulation data well, suggesting that the pollution process in turbulent flows may be adequately described as a self-convolution process.

If H_0 is smaller than $\simeq$0.1, the evolution of the pristine fraction is more complicated, and one cannot satisfactorily fit the entire evolution of $P(Z_c, t)$ with the convolution model, Equation (18), by properly choosing the parameters n and τ_{con}. In this case, the pollution process shows different behaviors at early and late evolution phases. A two-phase behavior for scalar fields with small H_0 was actually seen earlier in the scalar variance decay (see the bottom panel of Figure 3 for scalars iiiC and iiiD in the Mach 6.2 flow). For these cases, only a small fraction of the flow material, near the pollutant blobs, experiences PDF convolution at early times, because the amount of pollutants available for mixing is limited. This suggests that the convolution of the concentration PDF is local in space in the early phase, and based on the physical discussion in Section 3.1, the mixing process in this phase would be better described by a "discrete" version of the convolution model (with $n = 1$). Consistent with this picture, we find that the pristine fraction in the early phase is in good agreement with the prediction, Equation (19), of the "discrete" convolution model, or equivalently Equation (18) with $n = 1$. With time, more and more flow is polluted, and the mixed flow

material then acts as sources for further pollution. The PDF convolution would thus become more global in spatial space and hence more continuous in Laplace space, leading to an increase in n. As described in Section 3.1, n essentially corresponds to the degree of spatial locality for the PDF convolution. Recognizing the different mixing behaviors at early and late times, we attempted to apply a two-phase fitting procedure for scalar fields with $H_0 \leqslant 0.01$ (see PSS).

For a two-phase fit, we need to determine the transition time at which the two behaviors connect. Since the generalized convolution model with a single phase provides perfect fits to scalar fields with $H_0 \geqslant 0.1$, one may expect that the second phase with a more global PDF convolution starts when the pristine fraction, $P(Z_c, t)$, decreases to 0.9. We thus first tried to obtain a fitting function that connects the two phases at the time $t_{0.9}$ when $P(Z_c, t) = 0.9$. The results are shown as dashed lines in Figure 4. In these lines, the early phases are fit by the "discrete" model, Equation (19), with $\tau_{\rm con} = 0.17\,\tau_{\rm dyn}$ for both case iiiC ($H_0 = 0.01$) and case iiiD ($H_0 = 0.001$). Once $P(Z_c, t)$ decreases to 0.9, we use the generalized model prediction, $P(Z_c, t) = 0.9/[0.9^{1/n} + (1 - 0.9^{1/n})\exp((t - t_{0.9})/\tau_{\rm con})]^n$ (cf. Equation (18)) with $n = 10$. The timescale $\tau_{\rm con}$ for the late phase is set to 0.23 and $0.25\,\tau_{\rm dyn}$ for case iiiC and case iiiD, respectively. The fitting values adopted for n and $\tau_{\rm con}$ in the late phase are close to those used for the scalar fields with $H_0 \geqslant 0.1$. This means that, once the polluted fraction becomes larger than $\simeq$0.1, the pristine fraction decays in a similar way as the $H_0 \gtrsim 0.1$ fields. The fitting quality of the dashed lines appears to be acceptable. To distinguish the two convolution timescales in the early and late phases, we denote them as $\tau_{\rm con1}$ and $\tau_{\rm con2}$, respectively. We will also use $\tau_{\rm con2}$ to denote the convolution timescale for scalar fields with $H_0 \geqslant 0.1$ because the decay of the pristine fraction for those fields is similar to the later-phase evolution of the $H_0 \leqslant 0.01$ cases.

We find that one can obtain better fits for scalar fields with $H_0 \leqslant 0.01$ by connecting the two phases at later times. As shown in PSS, for these fields the "discrete" model well matches the simulation data in an extended time range until $P(Z_c, t)$ drops to 0.2–0.3. This allows us to connect the early and late behaviors at a time significantly larger than $t_{0.9}$. It turns out that the fitting quality is actually significantly improved if we start to use the generalized model with $n = 10$ at times when $P(Z_c, t)$ is smaller than $\simeq$0.7. The solid lines in Figure 4 for cases iiiC and iiiD show the fitting functions that connect the "discrete" model and the later phase at $t_{0.5}$ when $P(Z_c, t)$ decreases to 0.5. In the fitting curves, $\tau_{\rm con1}$ for the "discrete" phase is set to $0.18\,\tau_{\rm dyn}$ for both the case iiiC and case iiiD. Starting from $t_{0.5}$, we use the generalized model $P(Z_c, t) = 0.5/[0.5^{1/n} + (1 - 0.5^{1/n})\exp((t - t_{0.5})/\tau_{\rm con})]^n$ with $n = 10$. The timescale $\tau_{\rm con2}$ is set to 0.25 and $0.27\,\tau_{\rm dyn}$ for case iiiC and case iiiD, respectively. From Figure 4, the two-phase fitting lines connecting at $t_{0.5}$ agree with the data considerably better than the dashed lines that connect at $t_{0.9}$. Our choice here to connect the two phases at $t_{0.5}$ is somewhat arbitrary because there is an extended time range where both the "discrete" model and the $n = 10$ model can match the simulation data (PSS). In fact, combining the two models at any time with $0.2 \lesssim P(Z_c, t) \lesssim 0.7$ would give fitting curves of similar quality. The parameter n adopted in both the dashed lines and the solid lines is 10, i.e., the same as used for the scalar fields with $H_0 \geqslant 0.1$. This is also the case for the convolution timescale $\tau_{\rm con2}$ in the second phase. The values of $\tau_{\rm con2}$ used in the solid lines almost coincide with those adopted in the fitting lines for scalar fields with $H_0 \geqslant 0.1$, and in the dashed lines the $\tau_{\rm con2}$ values are only slightly smaller (by $\lesssim$10%). For the early phase, the adopted values for the timescale $\tau_{\rm con1}$ in the solid and dashed lines are very close too.

Our result that connecting the two phases at $t_{0.5}$ yields better fits than at $t_{0.9}$ seems to suggest that, for scalar fields with $H_0 \lesssim 0.01$, the pollution process does not make an immediate transition from the "discrete" to the generalized convolution model with larger n, when the pristine fraction decreases to 0.9. The transition tends to occur later. Considering that the generalized model with a single phase works perfectly for scalar fields with $H_0 \gtrsim 0.1$, this implies that the time at which the generalized convolution phase starts is not simply controlled by the value of the pristine or polluted fraction: it appears to have some dependence on whether the initial pristine fraction is larger or smaller than $\simeq$0.9. This does not cause any problems in a practical application if the exact value of the initial pollutant fraction, H_0, is known. One can use the generalized convolution model with a single phase if $H_0 \geqslant 0.1$, or adopt a two-phase model connecting at, say, $t_{0.5}$ if $H_0 \lesssim 0.1$.

However, there is some complication when applying this procedure to the subgrid model we will construct in Section 7 for large-eddy simulations (LESs) for the pollution of primordial gas in early galaxies. For example, if at a given time the pristine fraction in a computational cell is, say, between 0.9 and 0.5, then the choice of using the "discrete" model or the generalized model at that moment depends on whether the pristine fraction in that cell was larger or smaller than 0.9 when it was first polluted. This would make the implementation of our subgrid model complicated, as it requires keeping some information on the pollution history in each cell. We advocate simply using the generalized convolution model for any cells with a pristine fraction smaller than 0.9, as it gives acceptable, if not perfect, fits to our simulation data for $H_0 \leqslant 0.01$ scalars at any time after $t_{0.9}$. In the following subsections, we will only consider fitting functions that connect at $t_{0.5}$ for scalar fields with $H_0 \leqslant 0.01$, as they are in better agreement with the simulation data. We will tabulate the fitting parameters obtained from such fits in Section 5.4.6. If in a particular application connecting the early and later phases at $t_{0.9}$ is preferred rather than at $t_{0.5}$, our tabulated parameters would still be applicable, as the best-fit parameters used in the fitting curves that connect at $t_{0.9}$ and $t_{0.5}$ are very close.

In Figure 5, we show the simulation results and the fitting curves for scalar fields from the same category iii, but in the Mach 6.2 flow. For the fields with $H_0 = 0.5$ and 0.1, the data points are fit by the convolution model, Equation (18), with $n = 3$. The timescale $\tau_{\rm con2}$ for the two cases is set to 0.30 and $0.31\,\tau_{\rm dyn}$, respectively. Similar to the $M = 0.9$ case, two-phase models connecting at $t_{0.9}$ (dashed lines) and $t_{0.5}$ (solid lines) are used for the rest two cases with $H_0 \leqslant 0.01$. For the dashed lines, the early phase is fit by the "discrete" convolution model with $\tau_{\rm con1} = 0.22\tau_{\rm dyn}$ for scalar field iiiC and $\tau_{\rm con1} = 0.24\tau_{\rm dyn}$ for case iiiD, and for the late phase we used the $n = 3$ convolution model with $\tau_{\rm con2} = 0.31\,\tau_{\rm dyn}$ and $\tau_{\rm con2} = 0.33\,\tau_{\rm dyn}$ for the two cases, respectively. For the solid lines that connect at $t_{0.5}$, the fitting parameters for the "discrete" phase are $\tau_{\rm con1} = 0.23\tau_{\rm dyn}$ and $\tau_{\rm con1} = 0.25\tau_{\rm dyn}$ for cases iiiC and iiiD, respectively, and the late evolution stage is fit with $n = 3$ and $\tau_{\rm con2} = 0.34\,\tau_{\rm dyn}$ for both cases. Again, the fitting quality is better with a connection at $P(Z_c, t) = 0.5$. In all cases, the fitting parameters, n and $\tau_{\rm con2}$, adopted for the scalar fields with $H_0 \geqslant 0.1$ and for the late phases of the $H_0 \leqslant 0.01$ fields are very close, suggesting

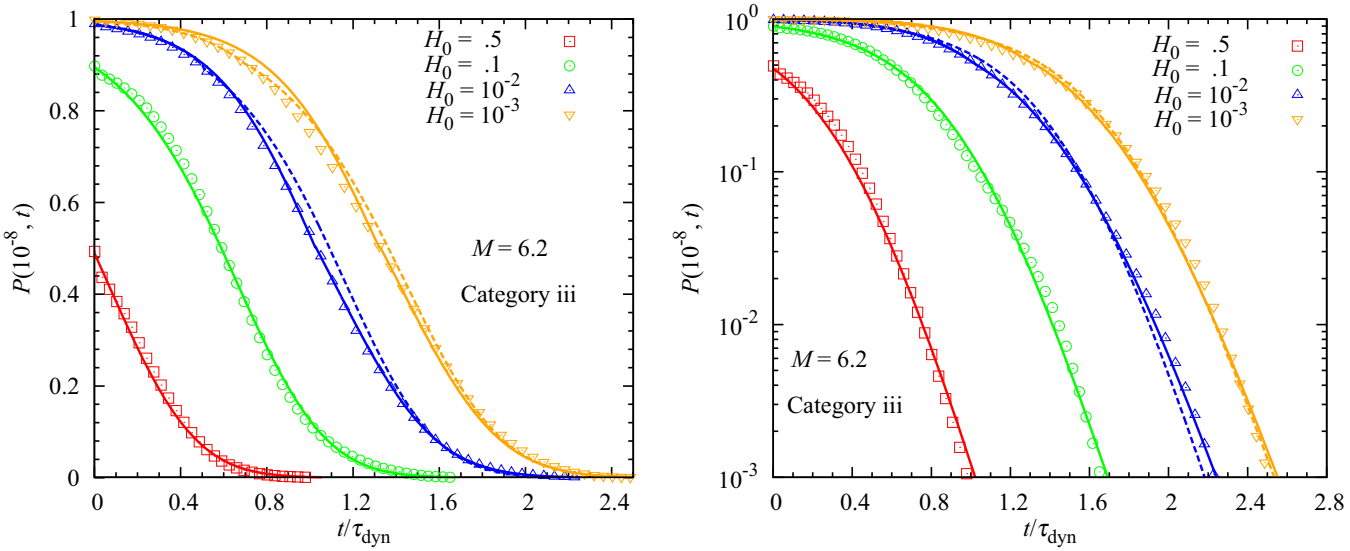

Figure 5. Same as Figure 4, but for scalar fields in the Mach 6.2 flow. See the text for details.
(A color version of this figure is available in the online journal.)

a universal decay behavior of the pristine fraction once the polluted fraction exceeds ≃0.3.

We find that, for scalar fields with $H_0 \leqslant 0.01$, it is more difficult to fit the early phases as H_0 decreases, and the fitting quality becomes poorer with decreasing H_0 (see Figures 4 and 5). The pollutant size is smaller for smaller values of H_0, and this may cause some complexities for the prediction of the pristine fraction. For example, as H_0 decreases to 0.001, the blob diameter is about the size of 30 computational cells, which is close to the scale where the flow inertial range ends. The first effect is that, with time, the size of the polluted region around each pollutant blob increases, and the turbulent stretching timescale in the polluted regions may increase with time. This is not accounted for in the convolution models since the convolution timescale is set to be constant. Another effect arises from the fact that the turbulent stretching rate has larger spatial variations at smaller scales. The turbulent eddy "seen" by a small pollutant blob may have a stretching rate different from the average value at the pollutant size. The increase in the amplitude of the stretching rate fluctuations with decreasing length scale indicates that the turbulent intensity around smaller blobs is more "random." In the early phase, the flow mass polluted by a single blob is expected to increase exponentially with the stretching rate. Therefore, using an average stretching rate for all the pollutant blobs may not give a precise prediction. The overall pollution rate depends on the turbulent stretching rates "seen" by all the pollutants at early times. The blobs encountering more intense eddies provide a larger contribution to the pollution process and vice versa. The effect is further amplified by the phenomenon of intermittency: the PDF of the stretching intensity exhibits fatter tails toward smaller scales. Therefore, the small blobs have a large chance of encountering extreme stretching events. Clearly, the effect of intermittency makes it more difficult to predict the pristine fraction for scalar fields with smaller H_0.

We point out that, for a given scalar field, the parameters, n and τ_{con2}, that can fit scalar fields with $H_0 \geqslant 0.1$ or the late phases of $H_0 < 0.1$ cases are not unique. In fact, a (small) range of parameter pairs (n, τ_{con2}) can give acceptable fits to the simulation data. For example, if a somewhat smaller (larger) n is used, one could also have a similar fit with a correspondingly smaller (larger) value of τ_{con2}. When obtaining the best-fit parameters, we attempted to select a single value of n that provides good fits to all scalar fields in each category. With the chosen n, we then determine the best-fit value of τ_{con2} for each scalar field in the category. As discussed above, the timescale turns out to be similar for all cases in a given category.

A comparison of Figures 4 and 5 shows that, when the time is normalized to the flow dynamical timescale, the pristine fraction in the Mach 6.2 flow survives for significantly longer than in the Mach 0.9 case (see also PSS). We discuss this Mach number dependence in the following subsection.

5.4.2. Dependence on the Flow Mach Number

In Figure 6, we show the evolution of the pristine fraction for scalar fields iiiB (left) and iiiC (right) in our four simulated flows. As observed earlier, with t being normalized to the flow dynamical time, τ_{dyn}, the decrease of the pristine fraction becomes slower with increasing Mach number. In the fitting lines for case iiiB (left panel), the parameter pair (n, τ_{con2}) is set to (10, 0.26 τ_{dyn}), (6, 0.29 τ_{dyn}), (5, 0.31 τ_{dyn}), and (3, 0.31 τ_{dyn}) for the four flows with $M = 0.9$, 2.1, 3.5, and 6.2, respectively. Again, we see that τ_{con2} first increases with M and then saturates for $M \gtrsim 3$. This trend is similar to that of the variance decay timescale, τ_m, as a function of M (see the top panel of Figure 3). As explained in Section 5.3, τ_m increases as the energy fraction in compressible modes increases and then becomes roughly constant when compressible energy fraction saturates at $M \gtrsim 3$. The same reasoning also applies here for the trend of τ_{con2} with M. Similar to the discussion in Section 5.3 on τ_m, the convolution timescale may have a different behavior with M in compressively driven flows.

In Section 5.2, we showed that, at a similar concentration variance, the PDF tail becomes broader as M increases, most likely because of the increase in turbulent intermittency. Because the pristine fraction corresponds to the far left tail of the concentration PDF, the effect also slows the pristine gas pollution at larger M. Another effect of the broadening of the PDF tail with increasing M is that it changes the shape of the pristine fraction versus time curve, as seen in Figure 6. To fit the

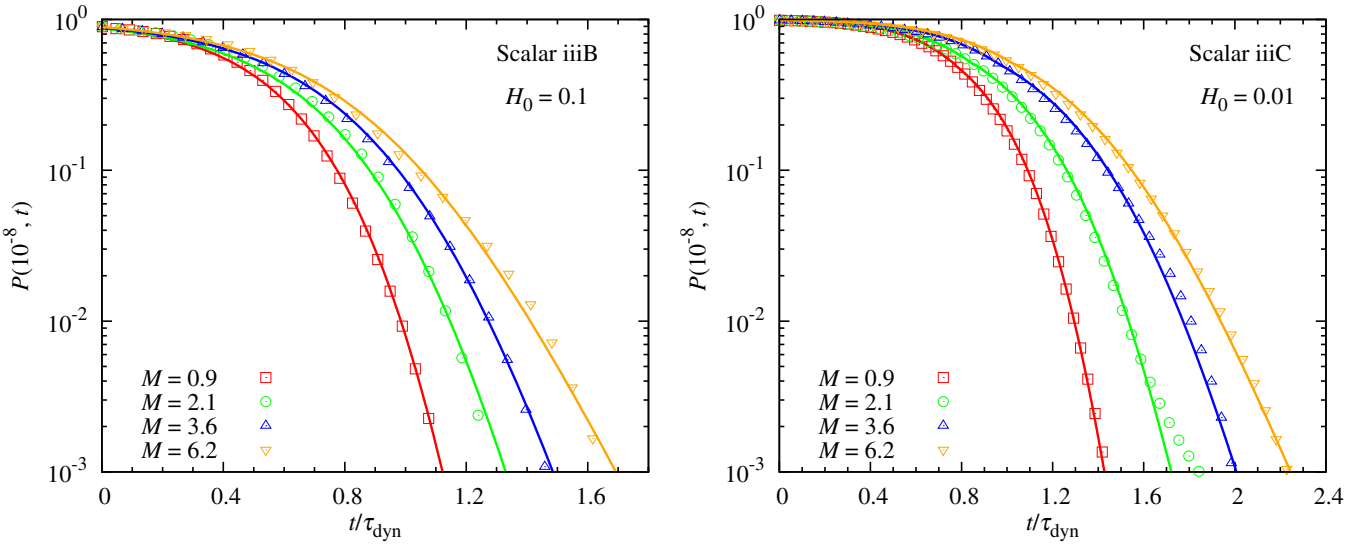

Figure 6. Mach number dependence of the pristine fraction. The two panels show $P(10^{-8}, t)$ as a function of time for scalar fields iiiB (left) and iiiC (right) in four simulated flows at Mach 0.9, 2.1, 3.5, and 6.2. Lines are fitting functions based on the predictions of self-convolution models. See the text for fitting parameters.
(A color version of this figure is available in the online journal.)

pristine fraction in flows at different M, we varied the parameter, n, in the self-convolution model, which controls the shape of the fitting function, Equation (18). The best-fit value of n decreases from 10 to 3 as M increases from 0.9 to 6.2. This decrease of n is expected from the fact that the self-convolution model with smaller n would predict broader PDF tails (see Section 3.1). The convolution model was originally proposed for mixing in incompressible turbulence, where n was a pure parameter without a clear connection to the mixing physics. Our finding that the convolution model with properly chosen n can well describe the pristine fraction evolution in compressible turbulent flows motivates a physical interpretation of the parameter.

A possible intuitive reason for why n decreases with the flow Mach number is that n reflects the degree of spatial locality of the PDF convolution, with more local mixing events implying a smaller n. In a highly supersonic turbulence, the majority of the flow mass resides in a small fraction of volume, i.e., in the dense postshock regions. Therefore, mixing of the pollutants into and within local regions of high densities is crucial toward the final homogenization. The dense postshock regions are persistent with a lifetime on the order of the flow dynamical time, and the timescale for the homogenization between different postshock regions is expected to be on the same order. This suggests that the presence of local dense regions may suppress the possibility of a global PDF convolution. In that case, as the flow Mach number increases, the convolution would become more local, leading to a decrease in n. Based on this argument, we speculate that, in compressively driven flows at similar M, the parameter n would be smaller than in our simulated flows. The convolution in a compressively driven flow is expected to be more local because the density fluctuations are stronger (e.g., Federrath et al. 2010).

The right panel of Figure 6 plots the results for case iiiC with $H_0 = 0.01$ in the four simulated flows. Again the decrease of the pristine fraction is slower in flows with larger M. As discussed earlier, a two-phase fitting scenario is needed for scalar fields with $H_0 \leqslant 0.01$. Using the discrete convolution model to fit the early-phase evolution, we find that the timescale τ_{con1} is 0.17, 0.19, 0.22, and 0.23 τ_{dyn} for $M = 0.9$, 2.1, 3.5, and 6.2, respectively. The two phases are connected at $t_{0.5}$. Note that the timescale τ_{con1} also increases with M at first and then saturates for $M \gtrsim 3$. For the late phase of scalar case iiiC, we adopted the same values of n (i.e., 10, 6, 5, and 3) for the flows as used in the case of iiiB. To match the simulation data, τ_{con2} in the late phase is set to 0.25, 0.30, 0.34, and 0.34 τ_{dyn} for $M = 0.9$, 2.1, 3.5, and 6.2, respectively. Again, these numbers are close to the best-fit values for case iiiB shown in the left panel.

In summary, we found that the pollution of the pristine gas is slower in flows at higher M. Two reasons are responsible for this behavior. First, the mixing (or variance decay) timescale τ_m becomes larger as M increases. Second, at the same concentration variance, the left PDF tail broadens with M, and this corresponds to a larger pristine fraction.

5.4.3. Dependence on the Pollutant Injection Length Scale

Next, we study the dependence of the pristine fraction evolution on the initial spatial configuration of the pollutants, i.e., on how the pollutants are released into the flow. Each category in Table 1 represents a different pollutant shape or distribution at the initial time. In Figure 7, we compare the simulation results for scalar fields from different categories in the Mach 6.2 flow. The left panel shows five B fields with $H_0 = 0.1$, and the right panel is for C cases with $H_0 = 0.01$. The initial condition for the scalar fields in categories i and ii is a single pollutant cube and a single spherical blob, respectively, and the pristine fraction evolution for scalar fields in these two categories is almost the same, suggesting that the geometric shape of the pollutant blob does not affect the pollution rate.

On the other hand, the pollution process has a sensitive dependence on the injection length scale, L_p. For scalar fields in first two categories (i and ii), L_p is about equal to the box size, or twice the flow driving scale, L_f. For categories iii, iv, and v, $L_p \simeq L_f$, $L_f/2$, and $L_f/4$, respectively. As expected in Section 4, the decay of the pristine fraction becomes progressively faster with decreasing L_p. The four lines in each panel of Figure 7 are fitting functions based on the self-convolution models. Since the data points almost coincide for scalar fields in categories i and ii, a single fitting curve (the line on the right) works for both cases. The other three fitting lines, from the right to the left, correspond to scalar fields in categories iii, iv, and v, respectively. The fitting

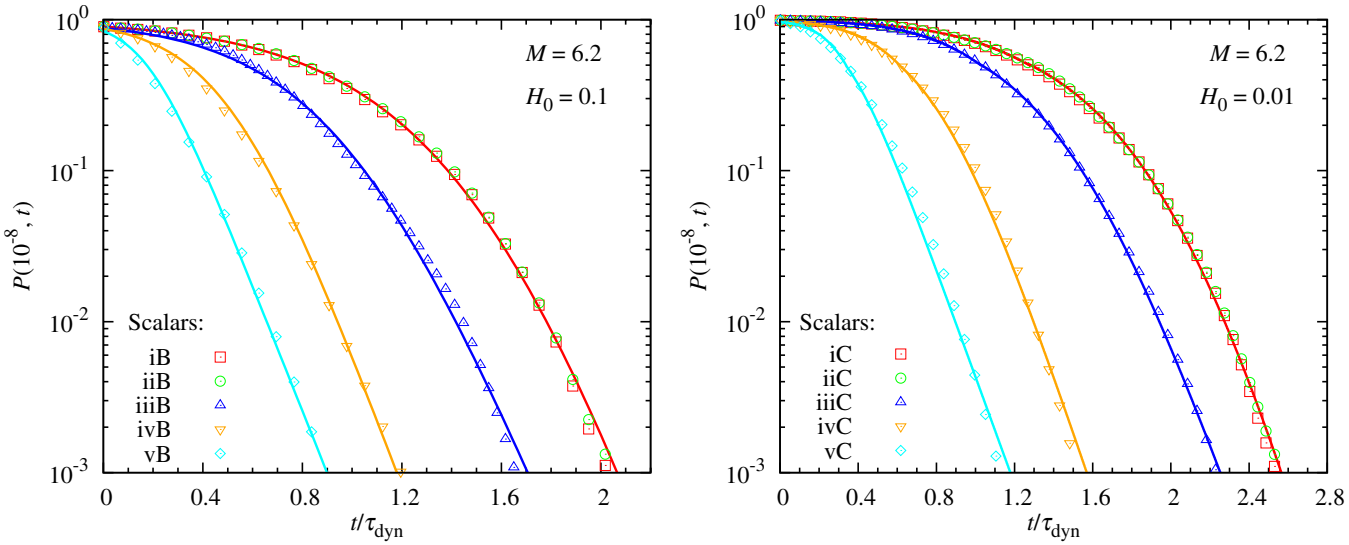

Figure 7. Dependence of the pristine fraction on the pollutant injection scale, L_p. The figure plots $P(10^{-8}, t)$ as a function of time for scalar fields with different pollutant shapes and spatial distributions in the Mach 6.2 flow. The left and right panels show B and C fields with $H_0 = 0.1$ and 0.01, respectively. The five cases in each panel are from the five categories listed in Table 1. The simulation data for scalar fields in categories i (single cubic pollutant) and ii (single spherical pollutant) almost coincide. The pollution of pristine gas becomes progressively faster as the pollutant injection length scale decreases. See the text for the description of the fitting lines.

(A color version of this figure is available in the online journal.)

parameters used for the B fields in the left panel are $n = 5, 3, 2,$ and 1, and $\tau_{con2} = 0.42, 0.32, 0.19,$ and $0.11\tau_{dyn}$, respectively, for the four lines from the right to the left.

The timescale τ_{con2} decreases by $\simeq$20% as L_p changes from $2\,L_f$ to L_f, and as L_p decreases further below L_f, the decrease of τ_{con2} is faster, dropping by $\simeq$40% for each factor of two in L_p. This trend is similar to the dependence of the variance decay timescale, τ_m, on L_p, which is controlled by the eddy turnover time at $\simeq L_p$ and decreases with decreasing L_p. This also explains the faster pollution of the pristine gas if the pollutants are injected at smaller scales. Recalling that τ_m was measured to be 0.72, 0.57, 0.48, and 0.34 τ_{dyn} for the same B fields in the Mach 6.2 flow with $L_p \simeq 2, 1, 0.5,$ and $0.25\,L_f$, respectively (see the middle panel of Figure 3), we see that τ_{con2} has a more sensitive dependence on L_p than τ_m. A possible reason for this is that the exposure of the pollutants to the pristine flow may be an important factor for the pollution efficiency, and with decreasing L_p, the number of pollutant blobs increases rapidly, leading to enhanced pollutant exposure.

The trend that n becomes smaller for scalars injected at smaller scales corresponds to broadening of the PDF tails with decreasing L_p found in Section 5.2. The PDF tails become broader because the flow structures "seen" by the scalars with smaller L_p are more intermittent, and thus the dependence of n on L_p is related to the higher degree of turbulent intermittency at smaller scales. If the turbulent flow is driven compressively, the decrease of n with decreasing L_p may be faster due to stronger intermittency of the flow. Note that broadening of the PDF tails makes the pristine fraction larger, but this effect is minor in comparison to the faster decrease of the pristine fraction caused by the smaller mixing timescale at smaller L_p. The decrease of n with decreasing L_p may also be understood from a more intuitive argument.

For scalar fields with a small L_p, each pollutant is stretched by a local velocity structure, and the mixing of each pollutant blob with the surrounding flow proceeds largely independently at early times. The pollution process is almost complete when the mixed areas by the pollutant blobs start to overlap (see the bottom panels of Figure 1), meaning that the PDF convolution occurs locally and independently in different regions of size L_p during most of the mixing process. As the injection scale decreases, the PDF convolution becomes more local, leading to a smaller value of n, which corresponds to a higher degree of spatial locality in the PDF convolution (see Section 3.1).

For C fields shown in the right panel, a two-phase scenario connecting at $t_{0.5}$ is used to obtain the fitting lines. In the early phase, the timescale, τ_{con1}, in the discrete convolution model is taken to be 0.30, 0.24, 0.17, and 0.1 τ_{dyn}, respectively, for the four fitting lines from right to left. The dependence of τ_{con1} is similar to that of τ_{con2} for the B cases. It is first reduced by 20%, as L_p decreases to L_f, and then decreases faster, by $\simeq$30%–40%, as L_p decreases further by each factor of two. For the late phase, we adopted the same values (5, 3, 2, and 1) of n as for the corresponding B cases shown in the left panel, and τ_{con2} is set to 0.43, 0.34, 0.22, and 0.12 τ_{dyn} for scalar fields with $L_p \simeq 2,\ 1,\ 0.5,$ and $0.25\,L_f$, respectively. Again, these values of τ_{con2} are close to those used in the fitting lines for the corresponding B cases. It is interesting to note that, for case vC, $n = 1$ is adopted in both the early and late phases, although the timescales $\tau_{con1} = 0.1\,\tau_{dyn}$ and $\tau_{con2} = 0.12\,\tau_{dyn}$ are slightly different.

We also examined the L_p dependence for all the other scalar fields including those in the other three flows. We found similar trends for the parameters, n, τ_{con1}, and τ_{con2}, with varying pollutant injection scale. The results are tabulated and further discussed in Section 5.4.6.

5.4.4. Dependence on the Threshold Metallicity

When presenting simulation results in earlier subsections, we set the threshold metallicity to $Z_c = 10^{-8}$ as a representative value, but as discussed in the Introduction, the threshold value for the transition to normal star formation is uncertain. We therefore need to study the dependence of the pristine fraction $P(Z_c, t)$ on the Z_c. In Figure 8, we plot $P(Z_c, t)$ at different threshold values for scalar iiiC in the Mach 6.2 flow. The two panels show the same figure on linear–linear and linear–log

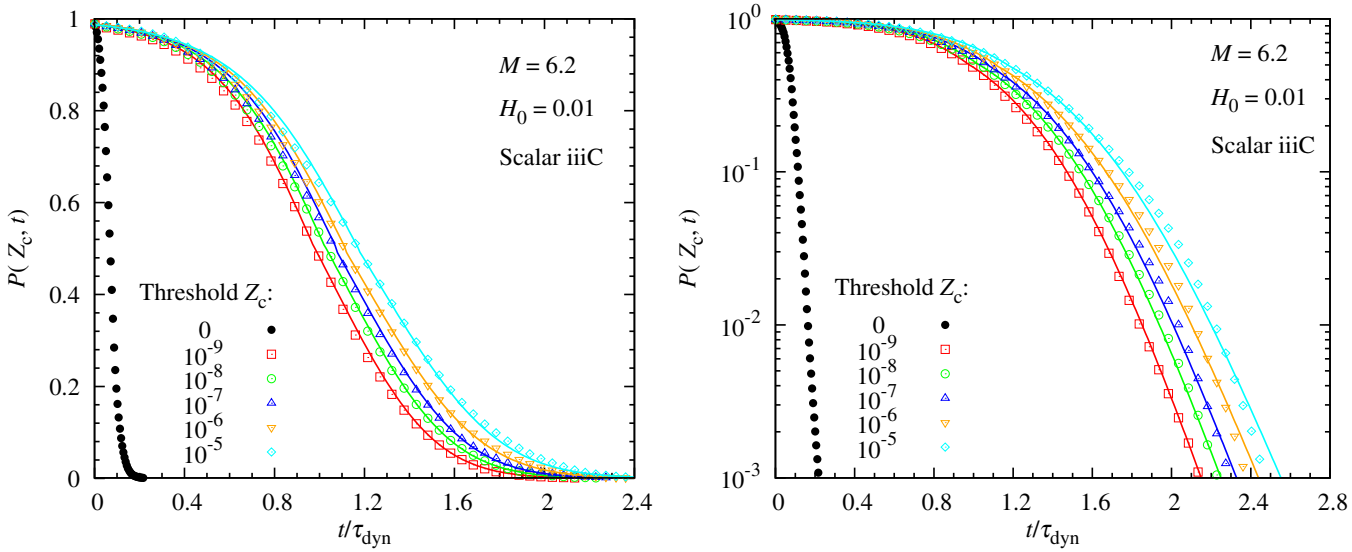

Figure 8. Dependence of the pristine fraction on the metallicity threshold, Z_c. The figure plots $P(Z_c, t)$, as a function of time for different values of Z_c. The scalar field shown here is iiiC in the Mach 6.2 flow. The left and right panels are the same figure plot on linear–linear and linear–log scales, respectively.
(A color version of this figure is available in the online journal.)

scales, respectively. We consider the scalar case C as an example, with which we can examine the Z_c dependence of both convolution timescales, τ_{con1} and τ_{con2}, for the early and late phases, respectively.

The filled circles in Figure 8 correspond to the fraction of exactly pristine flow material with $Z = 0$. This fraction decreases to zero almost instantaneously. This is caused by the effect of numerical diffusion. During each time step, any computational cell adjacent to one that contains pollutants or has been polluted by earlier mixing events will obtain a finite, but often extremely small concentration. This means that the exactly pristine flow material would be completely lost in a number of steps $\approx L_p/\Delta$ with L_p and Δ being the average pollutant separation and the computation cell size, respectively. The time step in our simulation is approximately given by Δ/v_{max}, where v_{max} is the maximum flow velocity at a given time. Therefore, the survival time of exactly pristine gas is L_p/v_{max}, which is much smaller than the flow dynamical time L_f/v_{rms} because $v_{max} \gg v_{rms}$. The almost immediate removal of exactly metal-free gas by numerical diffusion is analogous to the expectation in Section 3.2 that the molecular diffusivity alone tends to reduce the exactly pristine fraction $P(t)$ to zero instantaneously (see also PSS), although the numerical diffusion in our simulation probably has a different form and amplitude than the realistic molecular diffusivity.

The open symbols in Figure 8 show simulation data for finite, and more realistic, threshold values in the range from 10^{-9} to 10^{-5}. For Z_c in this range, the simulation data for $P(Z_c, t)$ can be fit by the self-convolution models. The fitting lines in Figure 8 are obtained using a two-phase scheme which combines the early and late behaviors at $t_{0.5}$. Fitting the early phase with the discrete convolution model, we find that the dependence of the timescale τ_{con1} on Z_c is very weak, with $\tau_{con1} = 0.226$, 0.233, 0.244, 0.253, and 0.271 τ_{dyn} for the five threshold values increasing from 10^{-9} to 10^{-5}. If we express the dependence as a power law, $\tau_{con1} \propto Z_c^{a_1}$, the exponent, a_1, would be very small, $\simeq$0.015. Note that the increase seems to be faster (by about 7%), as the threshold increases from 10^{-6} to 10^{-5}. For the late phase, we fixed the parameter n at 3 (the same as used before for this scalar), and adjusted the timescale τ_{con2} to match the data points for different threshold values. The best-fit value for τ_{con2} was found to be 0.33, 0.344, 0.355, 0.375, and 0.39 τ_{dyn} for $Z_c = 10^{-9}, 10^{-8}, 10^{-7}, 10^{-6}$, and 10^{-5}, respectively. On average, τ_{con2} increases by 4% as Z_c increases by each factor of 10, and the dependence can be roughly written as $\tau_{con2} \propto Z_c^{a_2}$ with $a_2 = 0.02$. A similar Z_c dependence of the convolution timescales was also found for other cases with different L_p and in flows at different M. There is also a general trend that the increase of the convolution timescale with the threshold becomes faster as Z_c increases to the highest value, 10^{-5}, considered in our study.

The weak power-law dependence of the convolution timescales, τ_{con1} and τ_{con2}, on Z_c may extend to a range of threshold values below 10^{-9}, although as $Z_c \to 0$, the numerical diffusion would finally be able to directly act to reduce $P(Z_c, t)$ and the scaling of the convolution timescale with Z_c given earlier would fail. The $Z_c \to 0$ limit may not be of practical interest, as the critical metallicity is likely to be higher than 10^{-9} by mass. In the other limit, with increasing Z_c, the weak power-law scaling will also break down eventually. As pointed out above, the increase of the convolution timescales is already faster as Z_c increases to 10^{-5}. In fact, if Z_c approaches the average concentration $\langle Z \rangle$, (0.01 for the scalar field shown in Figure 8), Equation (18), which was derived in the limit $Z_c \to 0$, will become invalid. For illustration, let us consider the case in which Z_c is exactly equal to $\langle Z \rangle$. In this case, the fraction $P(Z_c, t)$ would not decrease to zero in the long time limit; instead it would approach 1/2. A more extreme example is that, if Z_c is larger than $\langle Z \rangle$, $P(Z_c, t)$ would first decrease when the pollutants mix with a small amount of the flow material, and then increase and finally approach unity when the flow is completely homogenized. This situation may occur at very early times in the history of a galaxy, before heavy elements produced by supernova explosions increased the average metallicity to above the critical threshold. However, there is the possibility metals from the explosion of a single massive Pop III star could make $\langle Z \rangle > Z_c$ in a small high-redshift galaxy (Frebel et al. 2009). Even if the average metallicity in the entire ISM is larger than Z_c, there may exist local regions where the average metallicity is smaller than the threshold. One would need to deal with this

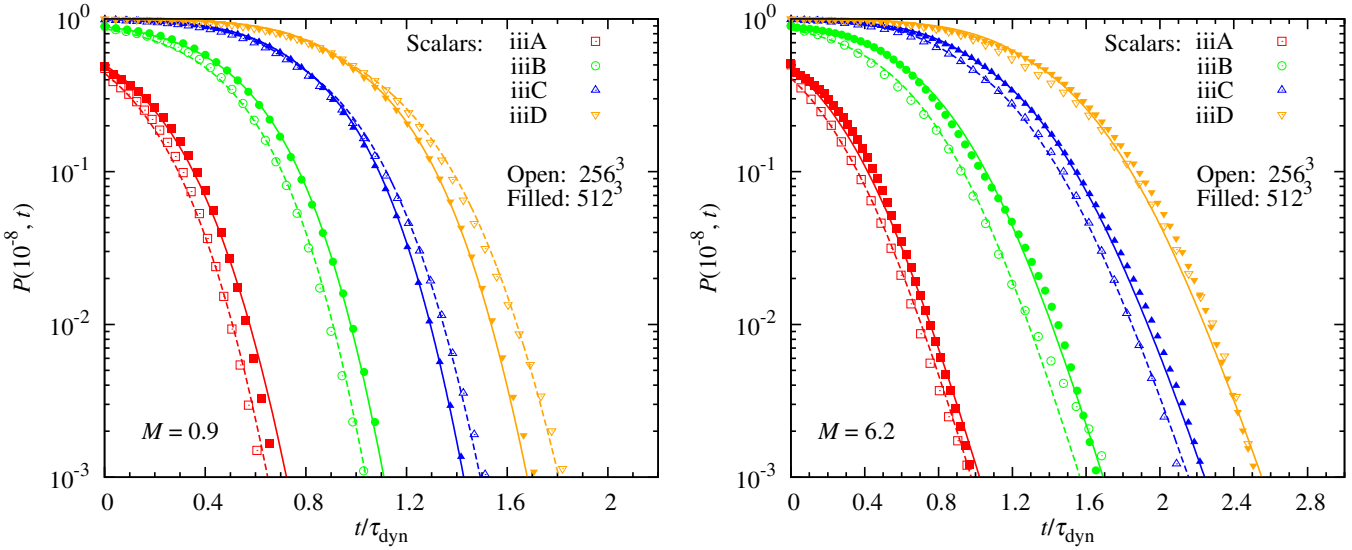

Figure 9. Pristine fraction, $P(Z_c, t)$, as a function of time from 256^3 (open) and 512^3 (filled) simulations. The scalar fields shown here are from category iii in the Mach 0.9 (left) and 6.2 (right) flows. The results from the 512^3 runs, already shown in Figures 4 and 5, are replotted here for a comparison with the 256^3 data. No model fit is given to the 256^3 data for case iiiD in the $M = 6.2$ flow because the points are close to the 512^3 result.

(A color version of this figure is available in the online journal.)

situation in a subgrid mode for the large-scale simulation for the primordial gas pollution in an early galaxy (see Section 7). In this work, we do not examine the evolution of $P(Z_c, t)$ for Z_c close to or even larger than $\langle Z \rangle$. We defer it to a later work. In the case of $\langle Z \rangle < Z_c$, a good approximation is perhaps to assume that $P(Z_c, t)$ is a constant ≈ 1.

Considering that $P(Z_c, t)$ would show qualitatively different behaviors as the ratio, $Z_c/\langle Z \rangle$, gets close to unity, it appears appropriate to take it as a function of $Z_c/\langle Z \rangle$, instead of the absolute value of Z_c. Another motivation is that, at a given ratio $Z_c/\langle Z \rangle$, $P(Z_c, t)$ samples a concentration range at a similar distance to the central part of the PDF. Thus, in Section 5.4.6, we tabulate the fitting parameters for the evolution of $P(Z_c, t)$ with $Z_c/\langle Z \rangle = 10^{-7}$ as functions of the flow Mach number and the pollutant injection scale. For other values of $Z_c/\langle Z \rangle$, the timescales, τ_{con1} and τ_{con2}, can be inferred using the weak power-law scaling given earlier, as long as $Z_c/\langle Z \rangle \lesssim 10^{-3}$.

5.4.5. Dependence on the Numerical Resolution

Finally, we examined the effect of numerical resolution. As discussed in Section 3.2, the timescale for the pollution of the pristine gas to a significant concentration level is mainly determined by the rate at which turbulence stretches the pollutants, and independent of the amplitude of the molecular or numerical diffusion if it is sufficiently small to allow a scale separation between the pollutant injection scale and the diffusion scale. To verify this expectation, we carried out 256^3 simulations and compared them with the results from 512^3 runs. The scale separation mentioned above exists at both resolutions, but the separation is limited for the 256^3 runs. We drive the flows in exactly the same pattern in the 256^3 and 512^3 runs. However, due to the "chaotic" nature of turbulence, the developed turbulent velocity field at given locations in the two runs are different. This means that, when released to the simulated flows at different resolutions, the pollutant blobs might encounter completely different velocity structures. In this sense, the comparison of our simulation results at two resolutions is somewhat different from the usual convergence check.

In Figure 9, we plot $P(Z_c, t)$ with $Z_c = 10^{-8}$ for scalar fields in category iii from the 256^3 (open symbols) and 512^3 (filled symbols) runs, with $M = 0.9$ and $M = 6.2$. The filled data points and the solid fitting curves for the 512^3 runs were already presented in Figures 4 and 5. Here, the early and late phases of cases iiiC and iiiD are connected at $t_{0.5}$. The fitting curves for the 256^3 data are obtained with the same fitting scenario as in the 512^3 case. In both the Mach 0.9 and 6.2 flows, the pristine fraction for the two scalar fields with $H_0 = 0.5$ (iiiA) and $H_0 = 0.1$ (iiiB) is smaller in the 256^3 runs. In fact, the fraction becomes smaller than in the 512^3 runs almost immediately after the pollutants are released into the flows. This can be explained by considering the action of numerical diffusion on the initial concentration field. Since our initial concentration field consists of pure pollutants ($C = 1$) and exactly pristine gas ($C = 0$), there exist sharp edges between the pollutant blobs and the pristine flow. Numerical diffusion may operate on the large concentration gradient at the edges, and a fraction of the flow material surrounding the pollutants would be polluted immediately. This results in an instantaneous drop in the pristine fraction. In the 512^3 runs, the effect was found to be weak, and the initial drop was slight. The drop is significantly larger in the 256^3 simulations due to the larger numerical diffusion, leading to smaller pristine fractions for scalars iiiA and iiiB in the 256^3 runs than in the 512^3 cases.

Recognizing this effect of initial drop, we adjusted the initial pristine fraction, P_0, to smaller values when fitting the 256^3 data. For scalar fields iiiA and iiiB, we used the same values of n (i.e., $n = 10$ and 3 for $M = 0.9$ and 6.2, respectively) as in the corresponding 512^3 cases. With the adjusted values of P_0, the best-fit timescales τ_{con2} for these two cases in the 256^3 runs differ slightly, only by $\lesssim 2\%$, from those used to fit the 512^3 data. This is the case for both Mach 0.9 and Mach 6.2 flows. Therefore, except for the initial drop, the numerical resolution does not affect how the pristine fraction evolves for the two fields with $H_0 \geqslant 0.1$, and one may claim a numerical convergence of the convolution timescale. Note that, in realistic interstellar turbulence, the effect of the initial drop would be minimal because the molecular diffusivity is much smaller

Table 2
The Convolution Timescale τ_{con1} for the Early-phase Evolution of $P(10^{-7}\langle Z\rangle, t)$ for Scalar Fields with Initial Pollutant Fraction $H_0 \lesssim 0.1$

M	$L_p = 2\,L_f$	$L_p = L_f$	$L_p = L_f/2$	$L_p = L_f/4$
0.9	0.25	0.18	0.12	0.075
2.1	0.30	0.20	0.14	0.085
3.5	0.29	0.22	0.14	0.09
6.2	0.28	0.23	0.15	0.09

Table 3
The Parameter n for the Pristine Fraction Evolution of Scalar Fields with $H_0 \gtrsim 0.1$ and for the Later-phase Evolution of $H_0 \lesssim 0.1$ Fields

M	$L_p = 2\,L_f$	$L_p = L_f$	$L_p = L_f/2$	$L_p = L_f/4$
0.9	∞	10	5	2.5
2.1	10	6	3	2
3.5	8	5	2.5	1.5
6.2	5	3	2	1

Table 4
The Convolution Timescale τ_{con2} for the Evolution of the Pristine Fraction $P(10^{-7}\langle Z\rangle, t)$ for Scalar Fields with $H_0 \geqslant 0.1$ and for the Later Phases of Scalar Cases with $H_0 \lesssim 0.1$

M	$L_p = 2\,L_f$	$L_p = L_f$	$L_p = L_f/2$	$L_p = L_f/4$
0.9	0.35	0.26	0.17	0.10
2.1	0.42	0.31	0.21	0.12
3.5	0.42	0.33	0.22	0.13
6.2	0.42	0.32	0.21	0.11

than the numerical diffusion in our simulations. Also the sharp pollutant-flow edges in the simulations are artificial and may not exist in reality.

The dependence on numerical resolution is more complicated for cases iiiC and iiiD with $H_0 = 0.01$ and $H_0 = 0.001$, respectively. As seen in Figure 9, the pristine fraction decay in the 256^3 runs can be either faster or slower than in the 512^3 simulations. The stronger initial drop in the 256^3 runs still exists in the early evolution phases. However, unlike scalar fields with $P_0 \geqslant 0.1$, it is not the dominant effect. The velocity field at a given location in the 256^3 and 512^3 simulations is different (see above), and thus the same pollutant blob may encounter very different velocity structures in the two runs. As discussed earlier, for cases with small H_0, the pollutant size is small, and the turbulent stretching rate around the blobs would show larger variations. Therefore, the stretching rate in the eddy across a small pollutant blob may deviate significantly from the mean value at that scale. Since the flow mass polluted by an individual blob scales nonlinearly with the local stretching rate, the overall pollution rate for scalar fields with tiny H_0 cannot be predicted by an average stretching rate, instead it depends on the distribution of the stretching rates over all the pollutant blobs. This is different from the case of $H_0 \gtrsim 0.1$ fields with large pollutant sizes, where the amplitude of the stretching rate fluctuations is smaller and the stretching rate for each blob is similar and equal to the average value. Thus, the pollution for scalar cases with small H_0 ($\lesssim$0.01) is more sensitive to the details of the stretching rates encountered by all the blobs. If the overall stretching rates in the eddies "seen" by the pollutant blobs in the 256^3 run is relatively higher, the pollution would proceed relatively faster than the 512^3 run and vice versa. It appears that the origin of the observed difference at late times is stochastic and has nothing to do with the numerical diffusion/resolution. The above picture also suggests that the difference may become larger as H_0 decreases further below 0.001.

When fitting the early phases of cases iiiC and iiiD in the 256^3 flows, we decreased P_0 to account for the initial drop. In the $M = 0.9$ flow, τ_{con1} for the early phases of these two cases are close to those used to fit the 512^3 data, and the difference is at the level of $\lesssim$5%. The best-fit timescales τ_{con2} for the late phases of the two scalars are larger (by $\simeq$10%) than for the 512^3 data. In the $M = 6.2$ flow, the fitting parameters for scalar iiiC in the 256^3 run are the same as in the corresponding 512^3 case, once the initial drop is accounted for. For case iiiD in the $M = 6.2$ flow, the data points from the 256^3 and 512^3 runs almost coincide, and we do not give a separate fit to the 256^3 data. It appears that the resolution dependence of the best-fit parameters is quite weak.

In summary, we find that the larger numerical diffusion in the 256^3 simulations causes a larger initial drop in the pristine fraction. This effect is successfully accounted by adjusting the value of P_0 in our model fits to the simulation results. The effect is expected to be negligibly weak in the interstellar gas where the molecular diffusivity is tiny. For scalar fields with small $H_0 \leqslant 0.01$, the timescales to fit the simulation data differ by $\lesssim$10% at the two resolutions, and numerical convergence may be claimed. The origin of the "random" dependence of the pristine fraction on the resolution for these fields is related to the larger fluctuations of turbulent stretching rate at smaller scales and suggests that a precise prediction of the pristine fraction in the case of tiny H_0 may require the detailed eddy conditions at the initial pollutant locations. We finally point out that numerical convergence would not exist at all if the resolution did not allow a separation between the pollution injection and the diffusion length scales.

5.4.6. Summary

We summarize our simulation results in Tables 2–4. The parameters listed in the tables are obtained by fitting the fraction $P(10^{-7}\langle Z\rangle, t)$ from simulation data for scalar fields from different categories and in different flows. Here, for each scalar, the threshold Z_c is set to $10^{-7}\langle Z\rangle$. The average concentration $\langle Z\rangle$ is equal to the initial pollutant fraction H_0 for a double-delta initial condition, Equation (6). For scalar fields A, B, C, and D, $H_0 = 0.5, 0.1, 0.01$, and 0.001, and we choose Z_c to be 5×10^{-8}, 10^{-8}, 10^{-9}, and 10^{-10}, respectively. The choice of a fixed ratio $Z_c/\langle Z\rangle$ is more convenient for practical applications. The timescales in Tables 2 and 4 are slightly different from those used in the figures in previous subsections, where (except in Section 5.4.4) the threshold was fixed at $Z_c = 10^{-8}$, for all values of H_0. The numbers in these two tables are in units of the flow dynamical time, τ_{dyn}. The first columns of Tables 2–4 show results for scalar fields with the injection scale L_p close to the box size or $\simeq 2\,L_f$. These parameters are measured from scalar cases in category i. Measuring the parameters using category ii fields with the same L_p would give essentially the same results.

Table 2 lists the timescale, τ_{con1}, for the early phase of scalar fields with $H_0 \leqslant 0.01$. In this phase, the pristine fraction evolution is fit by the "discrete" convolution model with $n = 1$. For scalar cases in each category (L_p) and each flow (M), we measured τ_{con1} for the early phases of fields C (with $H_0 = 0.01$) and D (with $H_0 = 0.001$), and the number given in Table 2 is the average of the measured values for these two fields. As found in Section 5.4.2, at a given injection scale, τ_{con1} first increases as M increases from 0.9 to 2–3, and then saturates for larger M. The overall increase in τ_{con1} is about 20% for M in the range

from 0.9 to 6.2. This is in general agreement with the trend of the mixing timescale τ_m with M found in PS10. At a given Mach number, τ_{con1} decreases with decreasing injection length scale L_p. As L_p decreases from $2\,L_f$ to L_f, τ_{con1} is smaller by ∼25%. The decrease is faster for smaller L_p, and a further decrease of L_p by each factor of two reduces τ_{con1} by ≃35%. If we express the L_p dependence of τ_{con1} roughly as a power law for $L_p \lesssim L_f$, we have $\tau_{con1} \propto L_p^{0.62}$.

Tables 3 and 4 give the parameters n and τ_{con2} as functions of M and L_p. These are measured for the pristine fraction evolution of scalar fields with $H_0 \geqslant 0.1$ or the late-time behavior of scalars with smaller H_0. For a given category (L_p) and a given flow (M), we choose a single value of n, with which the self-convolution model prediction can well match the simulation data simultaneously for both the two scalar cases with $H_0 \geqslant 0.1$ and the late phases of the other two cases with $H_0 \leqslant 0.01$. In Table 3, the parameter n is taken to be ∞ for scalar fields with $L_p \simeq 2\,L_f$ in the Mach 0.9 flow, which corresponds to the continuous-convolution model (Equation (20)). PSS showed that the continuous model can be used to obtain successful fits to category i scalars in the $M = 0.9$ flow. We find that, for a given τ_{con2}, the predicted pristine fraction by the convolution model barely changes with increasing n once n exceeds ∼20. This means that replacing ∞ in Table 3 by any number larger than 20 would also work for category i (or ii) fields in the Mach 0.9 flow.

From Table 3, we see that n decreases with increasing Mach number and decreasing L_p. This is due to the higher degree of flow intermittency at larger M (Pan & Scannapieco 2011) or smaller L_p, which causes broader concentration PDF tails. As described previously, a smaller n indicates a more local PDF convolution.

After fixing the parameter n for each L_p and M, we measure the timescale, τ_{con2}, for scalar cases A and B and the late phases of cases C and D. The measured values for the four cases are not exactly the same, but show slight variations. The variations are stronger at larger M or smaller L_p. We found that the amplitude of the variations is smaller when using a fixed $Z_c/\langle Z\rangle$ ratio rater than a fixed threshold Z_c. This also justifies taking the pristine fraction as a function of $Z_c/\langle Z\rangle$. The numbers given in Table 4 are the averages of the best-fit values for the four scalar cases in each category and each flow. The dependence of τ_{con2} on M and L_p is very similar to that of τ_{con1} shown in Table 2. Again, it increases by about 20% as M increases from 0.9 to 2–3, and then stays constant at larger M. Like τ_{con1}, the decrease of τ_{con2} with decreasing L_p also appears to be faster at smaller L_p. It is reduced by 25%, 35%, and 40%, respectively, as L_p decreases by each factor of two from $2L_f$ to $L_f/4$. Roughly, τ_{con2} scales with the injection scale as $\tau_{con2} \propto L_p^{0.65}$ for $L_p \lesssim L_f$.

We point out that, when measuring the model parameters from all the scalar fields with $H_0 \leqslant 0.01$, we connected the early and late phases at the time $t_{0.5}$ as the pristine fraction decreases to 0.5. However, as discussed in Section 5.4.1, one can still use the parameters given in Tables 2–4 if a connection at an earlier time, $t_{0.9}$, is preferred in a particular application.

Tables 2–4 can be used for practical applications. One may first fix the three parameters, τ_{con1}, n, and τ_{con2}, by interpolating the tabulated values according to the flow Mach number, M, and the pollutant injection scale, L_p, and for interpolation purposes, one can replace $n \to \infty$ by, say, $n = 20$ for the case with $M = 0.9$ and $L_p = 2\,L_f$. For subsonic flows with $M < 0.9$, we expect the parameters to be very close to those measured here for the $M = 0.9$ flow. As shown in PS10 and Pan & Scannapieco (2011), the velocity structures at all orders in the Mach 0.9 flow are essentially the same as in incompressible turbulence (corresponding to the limit $M \to 0$). In the other limit of large M, the timescales would not change with M for $M \gtrsim 6$, since they already saturate at $M = 2$–3. The parameter n may keep decreasing as M increases above 6.2, and in that case one may obtain n by extrapolation, with the expectation that n has a minimum value of 1, corresponding to the highest degree of spatial locality in the PDF convolution. For the dependence of the timescales on L_p, we can use the approximate power-law scalings given above for $L_p \lesssim L_f$. Next, depending on the initial pollutant fraction H_0, one may decide whether to start with an early phase using the discrete convolution model. For different values of the ratio $Z_c/\langle Z\rangle$, n does not change, and the timescales τ_{con1} and τ_{con2} may be obtained from the weak power-law scaling with Z_c given in Section 5.4.4. The scaling applies for $Z_c/\langle Z\rangle \lesssim 10^{-3}$.

For convenience, we have computed fits to τ_{con1}, n, and τ_{con2}, which can be used in place of interpolating along the table. Because the regime in which $L_p \leqslant L_f$ is the most important one for most astrophysical systems, we have focused on this case when computing our L_p dependence, and furthermore, because of the statistical noise in our measurements, we have taken an average scaling of $L_p^{0.63}$ for both τ_1 and τ_2. Imposing a strict floor of $n \geqslant 1$ and the Z_c scaling measured above, we find

$$\tau_{con1} = [0.225 - 0.055\exp(-M^{3/2}/4)] \times \left(\frac{L_p}{L_f}\right)^{0.63} \left(\frac{Z_c}{10^{-7}\langle Z\rangle}\right)^{0.015}, \quad (22)$$

$$\tau_{con2} = [0.335 - 0.095\exp(-M^{2}/4)] \times \left(\frac{L_p}{L_f}\right)^{0.63} \left(\frac{Z_c}{10^{-7}\langle Z\rangle}\right)^{0.02}, \quad \text{and} \quad (23)$$

$$n = 1 + 11\,\exp(-M/3.5)\left(\frac{L_p}{L_f}\right)^{1.3}, \quad (24)$$

which provides good fits for all Mach numbers and pollution properties, as long as $Z_c/\langle Z\rangle \lesssim 10^{-3}$ and $L_p \leqslant L_f$. We finally point out that the parameters may have a dependence on how the turbulent flow is driven. For example, in a compressively driven flow at the same Mach number, n may be smaller than measured from our simulations (see Section 5.4.2).

6. APPLICATION TO THE POLLUTION OF PRIMORDIAL GAS IN EARLY GALAXIES

6.1. The Global Pristine Fraction

In previous sections, we have focused on understanding the fundamental physics of the pollution of pristine flow material by turbulent mixing. We now describe how our results can be applied to investigate the pollution of primordial gas in the ISM of high-redshift galaxies. In this section, we discuss using our results to obtain a qualitative estimate of the pollution timescale in early galaxies, similar to the formalism of Tinsley (1980) in which the evolution within a galaxy is reduced to a few general parameters. A more accurate approach based on LESs and subgrid modeling will be presented in the next section.

To study the mixing of heavy elements in interstellar turbulence, we need to specify the source term in the PDF equation (2), which can be evaluated by considering how the

pollutants, including fresh metals from supernova explosions and low-metallicity or pristine infall gas, affect the metallicity PDF (see Section 2.2). If the supernova rate per unit volume in a given region of a galaxy is $\dot{n}_{\rm SN}(\mathbf{x}, t)$, the source term due to new metals from supernovae would be $\dot{n}_{\rm SN} m_{\rm ej}[\delta(Z - Z_{\rm ej}) - \Phi(Z; \mathbf{x}, t)]$, where it is assumed that, on average, each supernova produces an ejecta mass of $m_{\rm ej}$ with a mass fraction of metals $Z_{\rm ej}$, and that Rayleigh–Taylor and Kelvin–Helmholtz instabilities arising during the explosion mix the fresh metals with the envelope material. In reality, the source term by supernovae may have a finite width instead of being a delta function, because the ejecta mass and the heavy element yield vary with the mass of the progenitor star. One can refine the form of the source term by using nucleosynthesis results for the ejecta mass and metal yield as functions of the progenitor mass (e.g., Maeder 1992; Woosley & Weaver 1995; Heger & Woosley 2002) and accounting for the initial stellar mass function. The $-\Phi$ term corresponds to the replacement of the existing PDF in a fraction of the interstellar gas by $\delta(Z - Z_{\rm ej})$ due to the release of new metals from supernovae, and it guarantees the source term conserves the total probability.

During the formation of an early galaxy, there may exist an infall of primordial gas that continuously flows from the halo into the galaxy. This provides another source term, $\dot{m}_{\rm I}[\delta(Z) - \Phi(Z; \mathbf{x}, t)]$, where $\dot{m}_{\rm I}(\mathbf{x}, t)$ denotes the local infall rate. The infall rate should be taken to be zero except at the boundary, where the pristine gas enters the galaxy. Again the $-\Phi$ term is to ensure the conservation of the total probability. Clearly, new metals from supernovae and the pristine infall gas force spikes at high and low concentration levels in the PDF, respectively.

We define a global pristine fraction as $P_{\rm g}(Z_{\rm c}, t) = \int_0^{Z_{\rm c}} dZ \int_V dx^3 \langle\rho(\mathbf{x}, t)\rangle \Phi(Z; \mathbf{x}, t)/M_{\rm g}$ where V is the total volume of the galaxy and $M_{\rm g} = \int_V \langle\rho\rangle dx^3$ is the total mass of the interstellar gas. An equation for $P_{\rm g}$ can be derived by performing a double integration of Equation (2) over space and concentration. The advection term vanishes when integrated over space, and the double integral of the supernova source term gives $-(\dot{N}_{\rm SN} m_{\rm ej}/M_{\rm g}) P_{\rm g}(Z_{\rm c}, t)$, where $\dot{N}_{\rm SN}$ is the total supernova rate in the galaxy. Clearly, the contribution from supernovae is always negative. On the other hand, the infall of primordial gas contributes a positive term $(\dot{M}_{\rm I}/M_{\rm g})[1 - P_{\rm g}(Z_{\rm c}, t)]$, where $\dot{M}_{\rm I}$ is the global infall rate. Using the self-convolution model for the diffusivity term in the $P_{\rm g}$ equation, we obtain

$$\frac{dP_{\rm g}}{dt} = -\frac{n}{\tau_{\rm con}} P_{\rm g}\left(1 - P_{\rm g}^{1/n}\right) - \frac{\dot{N}_{\rm SN} m_{\rm ej}}{M_{\rm g}} P_{\rm g} + \frac{\dot{M}_{\rm I}}{M_{\rm g}}(1 - P_{\rm g}). \quad (25)$$

A similar equation with $n = 1$, and without the infall term was first given in Pan & Scalo (2007).

When writing Equation (25), we have made an implicit assumption of statistical homogeneity, which may break down for several reasons. First, the prediction of the self-convolution model for the pristine fraction evolution is tested and verified only in statistically homogeneous flows, and it may not be valid for a system with large-scale inhomogeneities. Second, Equation (25) adopts single values for the parameters n and $\tau_{\rm con}$, equivalent to assuming similar turbulence conditions everywhere in the interstellar gas. Finally, the first (mixing) term on the right-hand side is nonlinear with $P_{\rm g}$, and this nonlinearity would affect the prediction accuracy, if, for example, the star formation and hence the metallicity have a large-scale gradient. The parameters in Equation (25) should be viewed as the effective averages over the turbulence and metallicity conditions of the entire galaxy. These suggest that the solution of Equation (25) only provides a rough estimate for the global pristine fraction, which can be improved by accounting for realistic complexities. Nevertheless, the equation is a useful guideline for the study of the primordial gas pollution in early galaxies.

The turbulence conditions in the ISM of early galaxies are essentially unknown, and thus the parameters in Equation (25) cannot be estimated with certainty. Here, we will make various assumptions for the turbulence parameters, and discuss how the pollution of the pristine gas proceeds under different conditions. Future observations will help constrain the parameter space and give a clearer picture of the mixing process in high-redshift galaxies.

6.2. The Pollution Timescale

A crucial parameter for mixing in the interstellar gas is the driving length scale of the interstellar turbulence, $L_{\rm f}$. If the turbulence is driven at the largest scales, e.g., by the collapse of the baryonic matter into the potential well of the dark matter halo, then $L_{\rm f}$ is close to the size of the galaxy, $L_{\rm G}$. In this case, the primary energy source for turbulence is the gravitational energy, and the driving force of the interstellar turbulence is associated with the source term in Equation (25) for the pristine infall. The driving scale may also remain close to $L_{\rm G}$ at late times if the infall from the halo is persistent during the galaxy evolution. On the other hand, if the primary energy source for interstellar turbulence is the explosion energy of supernovae, then $L_{\rm f}$ is likely on the order of the typical size of supernova remnants, $L_{\rm SNR}$. In general, we expect $L_{\rm SNR} \lesssim L_{\rm f} \lesssim L_{\rm G}$, and depending on how $L_{\rm f}$ compares with $L_{\rm G}$, the pollution will proceed in qualitatively different ways.

We first consider the case where the turbulent driving scale, $L_{\rm f}$, is close to the galaxy size, $L_{\rm G}$. With $L_{\rm f} \simeq L_{\rm G}$, we may roughly think of the entire ISM as corresponding to our simulation box, and the dynamical time, $\tau_{\rm dyn}$, may be calculated by dividing $L_{\rm G}$ by the rms turbulent velocity. As new metals from supernovae are released to the interstellar turbulence, the supernova source term in Equation (25) reduces the pristine fraction, $P_{\rm g}$. We can start applying the self-convolution model in Equation (25) to calculate $P_{\rm g}$, once the average metallicity exceeds the threshold value, $Z_{\rm c}$. The parameters n and $\tau_{\rm con}$ can be estimated based on our simulation results tabulated in Section 5.4.6. With more supernovae exploding, the pollution process would become faster due to the increased amount of pollutants. Also, the average pollutant separation and hence the injection scale, $L_{\rm p}$, will decrease with the total number of supernovae, $N_{\rm SN}(t)$. Assuming a random supernova distribution, $L_{\rm p}$ scales like $N_{\rm SN}^{-1/3}$. The convolution timescale $\tau_{\rm con}$ would thus decrease with time, according to the power-law scaling of $\tau_{\rm con}$ with $L_{\rm p}$ resulting in a faster pollution rate. A subtle and minor effect is that the increase of the average metallicity reduces the threshold to average ratio, $Z_{\rm c}/\langle Z\rangle$, leading to a slight additional decreases in $\tau_{\rm con}$. This may be accounted for using the $Z_{\rm c}$-dependence of $\tau_{\rm con}$ given in Section 5.4.4. If the infall of pristine gas is persistent, the infall term in Equation (25) provides a continuous source for the pristine fraction, and there may exist a quasi-steady state for $P_{\rm g}$ (see Pan & Scalo 2007), which is controlled by three timescales, the convolution timescale, $\tau_{\rm con}$, the timescale for supernova sources, $M_{\rm g}/(\dot{N}_{\rm SN} m_{\rm ej})$, and the timescale for the mass accretion by infall, $M_{\rm g}/\dot{M}_{\rm I}$.

The estimate of $P_{\rm g}$ is more complicated if the driving scale, $L_{\rm f}$, is much smaller than $L_{\rm G}$. If $L_{\rm f} \ll L_{\rm G}$, the correlation length

scale of the turbulent velocity field is much smaller than the size of the entire ISM, and one may view the ISM as a collection of many "independent" turbulent regions of size $\sim L_{\rm f}$. The pollution process in each region would be similar to that in our simulation box, with a timescale determined by the local stretching/convolution timescale, $\sim\tau_{\rm dyn}$ ($\equiv L_{\rm f}/v_{\rm rms}$). However, the pollution in the entire ISM may not be simply described by a self-convolution model or Equation (25) with a local convolution timescale. This is because the situation in individual regions of size $L_{\rm f}$ may be completely different. For example, the regions that had supernova explosions at early times may have already been significantly polluted, while the pollution process may have not yet started in the regions that had not experienced supernovae or received any heavy elements. Thus, the mixing/pollution timescale over the entire galaxy may depend on the large-scale turbulent transport of pollutants between the "independent" regions. Assuming a random walk model for turbulent transport at scales $\gg L_{\rm f}$, the transport timescale at the galactic scale may be roughly estimated as $\tau_{\rm trans} \equiv L_{\rm G}^2/(L_{\rm f} v_{\rm rms})$, which is much larger than the local stretching timescale $L_{\rm f}/v_{\rm rms}$ and the timescale $L_{\rm G}/v_{\rm rms}$.

If $L_{\rm f} \ll L_{\rm G}$, another timescale of interest is $\tau_{\rm SN}$, defined as the time needed for the average separation between the supernova remnant locations to decrease below $\simeq L_{\rm f}$. In other words, $\tau_{\rm SN}$ represents the time for supernovae to populate the ISM at a level of about one per region of size $L_{\rm f}$. If the supernovae are randomly distributed, $\tau_{\rm SN}$ can be estimated from $N_{\rm SN}(\tau_{\rm SN}) \simeq (L_{\rm G}/L_{\rm f})^3$, where $N_{\rm SN}(t)$ is the total number of supernovae exploded before time t. At $t \ll \tau_{\rm SN}$, only a smaller number of supernovae occur, and the supernova sources would be statistically inhomogeneous at the scale $L_{\rm f}$. In that case, Equation (25) is not directly applicable as it implicitly assumes statistical homogeneity (see above).

Thus, the pristine fraction evolution in the $L_{\rm f} \ll L_{\rm G}$ case depends on a comparison of three timescales, $\tau_{\rm dyn}$, $\tau_{\rm SN}$, and $\tau_{\rm trans}$. From their definitions, $\tau_{\rm dyn} \equiv L_{\rm f}/v_{\rm rms} \ll \tau_{\rm trans} \equiv L_{\rm G}^2/(L_{\rm f} v_{\rm rms})$, and the amplitude of $\tau_{\rm SN}$ relative to these two timescales is crucial for how the pollution proceeds. If the star formation or supernova rate is so high that $\tau_{\rm SN} \ll \tau_{\rm dyn}$, the supernovae fill the ISM quickly, and its spatial distribution would appear more or less homogeneous at the scale $L_{\rm f}$ before each region of size $L_{\rm f}$ is significantly polluted. This suggests that the pollution in all the "independent" regions would roughly proceed at a similar pace, and the pristine fraction evolution in each region may approximately reflect the global pristine fraction. Therefore, at $t \gtrsim \tau_{\rm SN}$, one may apply Equation (25) to estimate the global pristine fraction using n and $\tau_{\rm con}$ corresponding to the physical conditions at the scale $L_{\rm f}$. In this case, the timescale for the decay of $P_{\rm g}$ would be $\simeq\tau_{\rm dyn}$.

If $\tau_{\rm dyn} \ll \tau_{\rm SN} \ll \tau_{\rm trans}$, the mixing of fresh metals from a supernova with the surrounding region of size $L_{\rm f}$ is fast with a relatively short timescale ($\sim\tau_{\rm dyn}$), and the ISM would have been completely polluted if, on average, each region of size $L_{\rm f}$ in the galaxy had one supernova explosion. This is expected to occur at time $t \simeq \tau_{\rm SN}$, and thus the pollution timescale in the entire galaxy is on the order $\sim\tau_{\rm SN}$.

Finally, if the star formation rate is very low and $\tau_{\rm SN}$ is significantly larger than $\tau_{\rm trans}$, then the turbulent transport at large scales ($\gg L_{\rm f}$) plays a crucial role in the pollution process. The delivery of heavy elements by the large-scale transport provides the entire galaxy with pollutants before the metal deposit by supernova events covers most of the ISM. The pollution in the galaxy would be completed at $\tau_{\rm trans}$. In this case, modeling the effect of the large-scale turbulent transport is essential.

One interesting limiting case is when the interstellar turbulence is completely driven by supernova explosions, and turbulent motions are weak outside the influence radius $L_{\rm SNR}$ of each supernova. In that case, we have $L_{\rm f} \simeq L_{\rm SNR}$ in regions affected by supernovae, and the transport of metals in between supernova locations would be slow with a large timescale $\tau_{\rm trans}$. From the discussion above, the pollution timescale would be determined by the maximum of the two timescales, $\tau_{\rm dyn}$ and $\tau_{\rm SN}$. We note that a quantitatively accurate prediction for this case may need to carefully account for the correlation between the metal injection and the turbulence driving force.

While Equation (25) provides a rough estimate for the pollution of primordial gas in early galaxies, perhaps the best tool for a quantitative prediction is a large-scale numerical simulation that can include complexities, such as large-scale velocity and metallicity inhomogeneities of the ISM, and the effect of large-scale transport. So far we have ignored the advection term in the PDF equation (2), which is responsible for the transport of the local PDF by the velocity field. The transport effect on the primordial gas pollution is substantial under certain circumstances, as seen earlier in the pollution timescale estimate. In the next section, we will establish a formulation for large-scale simulations of the pristine gas pollution in early galaxies. In the context of LESs, the advection term corresponds to the local PDF or pristine fraction exchange between neighboring computational cells due to both the large-scale velocity and the subgrid turbulent motions. Modeling the advection term in the PDF equation is crucial in these simulations, and we will adopt a commonly used subgrid closure for the transport effect by subgrid turbulent motions.

7. LARGE-EDDY SIMULATIONS AND SUBGRID MODELING

The complexities present in a realistic high-redshift galaxy can only be dealt with in detail through direct numerical simulations of the pollution of pristine gas in the ISM of a high-redshift galaxy. However, it is prohibitively expensive for such simulations to resolve the scale at which homogenization by molecular diffusivity occurs in interstellar turbulence. Limited resolution implies significant numerical diffusion, which causes artificial mixing, erasing any metallicity fluctuations that would exist below the size of a computational cell. In fact, due to the vast range of scales existing in the problem, resolving any inertial-range scales at all is extremely challenging (e.g., Scannapieco & Brüggen 2010). This results in an underestimate in the degree of metallicity fluctuations/inhomogeneity in the interstellar gas. Nevertheless, large-scale simulations still provide useful estimates for the low-order metallicity statistics, such as the metallicity variance, if they manage to resolve a small portion of inertial range, since the majority of the scalar fluctuation power is at large scales.

On the other hand, the problem is much more severe for the pollution of the primordial gas, which corresponds to high-order statistics of the metallicity fluctuations. Since the threshold metallicity $Z_{\rm c}$ for the transition to Pop II star formation is tiny, a computational cell would essentially lose all the pristine gas once it is subject to the pollution by even a small amount of heavy elements. A significant underestimate in the pristine mass fraction is therefore expected in simulations that do not resolve a considerable inertial range.

Here, we propose to approach the problem using LESs that keep track of the concentration fluctuations at subgrid scales. In such simulations, the flow at large scales is directly computed, while the effects of turbulent motions at subgrid scales are modeled. The existence of scale invariance in the inertial range of turbulent flows is crucial for subgrid modeling (Meneveau & Katz 2000), which justifies using the resolved flow structures to infer the feedback effect of small-scale fluctuations.

In this section, we outline an LES scenario for simulating the pollution of pristine gas in early galaxies. In Section 7.1, we first derive the LES equations for the interstellar turbulent flow and introduce subgrid models to close the equations, taking the so-called one-equation subgrid model (e.g., Lilly 1966), which evolves the turbulent kinetic energy at subgrid scales, as an illustrative example. In Section 7.2, we develop an LES formulation for the pristine fraction based on an equation for the local concentration PDF filtered at the resolution scale, using the self-convolution PDF models. The model parameters can be determined with the simulation results summarized in Section 5.4.6. By retaining the subgrid concentration fluctuations, the model provides a remedy to the overpollution by numerical diffusion, and is expected to significantly improve the predicting power of large-scale simulations for the primordial gas pollution in high-redshift galaxies.

7.1. Subgrid Modeling of the Interstellar Turbulent Flow

We start by introducing the basic filtering procedure used to derive the governing flow equations at resolved scales in LES. The procedure employs a low-pass filter function, $G(\mathbf{x}-\mathbf{x}')$, which eliminates fluctuations below the resolution scale of the simulation grid, Δ. Examples of the filtering function are a window function of width Δ or a Gaussian function with variance Δ^2. For any flow variable, $A(\mathbf{x},t)$, the filtered quantity $\overline{A}(\mathbf{x},t)$ is defined as

$$\overline{A}(\mathbf{x},t)=\int_V A(\mathbf{x}',t)G(\mathbf{x}-\mathbf{x}')dx'^3, \tag{26}$$

and it represents the variable at the resolved scales. From Equation (26), we have

$$\overline{\left(\frac{\partial A}{\partial t}\right)}=\frac{\partial \overline{A}}{\partial t},\qquad \overline{\left(\frac{\partial A}{\partial x_i}\right)}=\frac{\partial \overline{A}}{\partial x_i}, \tag{27}$$

where integration by parts is used to obtain the second equality. For compressible flows, it is more convenient to use the Favre filtering (e.g., Speziale et al. 1988; Moin et al. 1991; Erlebacher et al. 1992), defined as

$$\widetilde{A}(\mathbf{x},t)=\frac{\overline{\rho A}}{\overline{\rho}}, \tag{28}$$

where a density-weighted factor is included.

Applying the filtering procedure to the continuity and momentum equations gives

$$\frac{\partial \overline{\rho}}{\partial t}+\frac{\partial}{\partial x_i}(\overline{\rho}\,\widetilde{v}_i)=0, \tag{29}$$

and

$$\frac{\partial(\overline{\rho}\,\widetilde{v}_i)}{\partial t}+\frac{\partial(\overline{\rho}\,\widetilde{v}_i\,\widetilde{v}_j)}{\partial x_j}=-\frac{\partial(\overline{\rho}\,\tau_{ij})}{\partial x_j}-\frac{\partial \overline{p}}{\partial x_i}+\frac{\partial \overline{\sigma}_{ij}}{\partial x_j}+\overline{\rho}\,\widetilde{f}_i, \tag{30}$$

where τ_{ij}, called the subgrid-scale stress tensor, is defined as

$$\tau_{ij}=\widetilde{v_i v_j}-\widetilde{v}_i\,\widetilde{v}_j. \tag{31}$$

This tensor cannot be evaluated exactly because of the closure problem, and developing an adequate model for it is essential for LESs. The filtered pressure can be written as $\overline{p}=\overline{\rho}R\widetilde{T}$, where T is the gas temperature, and $R=k_{\rm B}/(\mu_{\rm H}m_{\rm H})$ is the ideal gas constant with $k_{\rm B}$, $\mu_{\rm H}$, and $m_{\rm H}$ being the Boltzmann constant, the molecular weight, and the atomic mass unit, respectively. The viscous stress tensor, σ_{ij}, in Equation (30) is given by $\sigma_{ij}=2\rho\nu(S_{ij}-(1/3)\delta_{ij}S_{kk})$, where ν is the kinematic viscosity and $S_{ij}=(1/2)(\partial_i v_j+\partial_j v_i)$ is the rate of strain tensor. We approximate the filtered viscous stress by $\overline{\sigma}_{ij}=2\overline{\rho}\nu(\widetilde{S}_{ij}-(1/3)\widetilde{S}_{kk}\delta_{ij})$, where $\widetilde{S}_{ij}\equiv(1/2)(\partial_i\widetilde{v}_j+\partial_j\widetilde{v}_i)$ is the strain tensor at the resolution scale. For interstellar turbulence, various sources contribute to the driving force, f_i, in the momentum equation, including, e.g., gravity and the acceleration by supernovae.

To evaluate the pressure term in Equation (30), one needs to consider the filtered energy or temperature equation, which reads (e.g., Garnier et al. 2009)

$$\begin{aligned}C_{\rm V}\frac{\partial(\overline{\rho}\,\widetilde{T})}{\partial t}+C_{\rm V}\frac{\partial(\overline{\rho}\,\widetilde{T}\,\widetilde{v}_i)}{\partial x_i}&=-\overline{\rho}R\widetilde{T}\,\frac{\partial \widetilde{v}_i}{\partial x_i}+\widetilde{S}_{ij}\,\overline{\sigma}_{ij}\\&+\frac{\partial}{\partial x_i}\left(\overline{\kappa}\frac{\partial \widetilde{T}}{\partial x_i}\right)-C_{\rm V}\frac{\partial(\overline{\rho}q_i)}{\partial x_i}\\&-\left(\overline{p\frac{\partial v_i}{\partial x_i}}-\overline{p}\,\frac{\partial \widetilde{v}_i}{\partial x_i}\right)+(\overline{S_{ij}\sigma_{ij}}-\widetilde{S}_{ij}\,\overline{\sigma}_{ij})\\&+\overline{\rho}\,\widetilde{\Gamma}-\overline{\rho}\,\widetilde{\Lambda},\end{aligned} \tag{32}$$

where $C_{\rm V}$ is the heat capacity of the flow material, equal to $3R/2$ for a monoatomic gas. The first term on the second line represents thermal conduction with κ being the thermal conductivity, where we assume $\overline{\kappa\,\partial_i T}\simeq\overline{\kappa}\,\partial_i\widetilde{T}$. The second term on the second line is the heat transport by subgrid turbulent motions, and the temperature flux q_i is defined as

$$q_i=\widetilde{T v_i}-\widetilde{T}\,\widetilde{v}_i. \tag{33}$$

The two terms on the third line of Equation (32) correspond to the effects of pdV work and heating by viscous dissipation at subgrid scales, which will be modeled later in this section. The last two terms, Γ and Λ, in the equation are the heating rate by external sources and the cooling rate by radiation, respectively.

A variety of subgrid models have been developed to approximate τ_{ij} (see reviews by Lesieur & Metais 1996; Meneveau & Katz 2000 for LES of incompressible flows). A major class of models adopt an eddy-viscosity assumption, relating the deviatoric part of τ_{ij} to the resolved strain tensor,

$$\tau_{ij}-\frac{1}{3}\tau_{kk}\delta_{ij}=-2\nu_{\rm t}\left(\widetilde{S}_{ij}-\frac{1}{3}\widetilde{S}_{kk}\delta_{ij}\right), \tag{34}$$

where the eddy viscosity, $\nu_{\rm t}$, is usually constructed as the product of a length scale ($\simeq\Delta$) and a velocity scale characteristic of the subgrid turbulent motions. In an LES for interstellar turbulence, $\nu_{\rm t}$ is typically much larger than the kinematic viscosity ν, and the viscous stress term in Equation (30) may be neglected. For incompressible flows, $\widetilde{S}_{kk}$ in Equation (34) vanishes because $\partial_i\widetilde{v}_i=0$, and the isotropic part, $(1/3)\tau_{kk}\delta_{ij}$, of the subgrid stress can be absorbed in the pressure term. Therefore, one obtains

a complete subgrid model for LES of incompressible flows by setting $\tau_{ij} = -2\nu_t \widetilde{S}_{ij}$. On the other hand, in compressible flows, the isotropic part must be modeled explicitly. This part behaves like a pressure term, and is sometimes named "turbulent pressure." Note that $\tau_{kk} = \widetilde{v_k v_k} - \widetilde{v}_k \widetilde{v}_k = 2K$, with K being the turbulent kinetic energy per unit mass at subgrid scales. Similar to the eddy-viscosity model for the subgrid stress, one may adopt an eddy-diffusivity assumption for the temperature flux, q_i, caused by subgrid turbulent motions,

$$q_i = -\alpha_t \frac{\partial \widetilde{T}}{\partial x_i}, \tag{35}$$

where the "eddy conductivity" α_t is of the same order as ν_t, and is usually parameterized by a subgrid Prandtl number, $\alpha_t = \nu_t / Pr_t$, where Pr_t is typically taken to be $\simeq 0.7$ (e.g., Eidson 1985; Erlebacher et al. 1992; Jaberi et al. 1999).

Eddy-viscosity models differ in how ν_t is evaluated. In the Smagorinsky (1963) model, ν_t is calculated by $(C_s\Delta)^2|\widetilde{S}|$ with $|\widetilde{S}| = (2\widetilde{S}_{ij}\widetilde{S}_{ij})^{1/2}$, which essentially assumes the amplitude of the subgrid velocity fluctuations goes like $\propto \Delta|\widetilde{S}|$. The Smagorinsky model has also been used in the LES of compressible flows (e.g., Moin et al. 1991; Erlebacher et al. 1992; Vreman et al. 1997). For compressible flows, Yoshizawa (1986) proposed to set $\tau_{kk} \equiv 2K = 2C_I\Delta^2|\widetilde{S}|^2$ for the isotropic part of the subgrid stress, which appears to underestimate subgrid kinetic energy (Park & Mahesh 2007).

A variant of the eddy-viscosity model is the so-called one-equation model, where an equation for the subgrid kinetic energy, K, is derived, modeled, and solved (e.g., Lilly 1966; Schumann 1975; Moeng 1984; Ghosal et al. 1995; Menon & Kim 1996, for one-equation models of compressible flows, see, e.g., Schmidt et al. 2006; Park & Mahesh 2007; Genin & Menon 2010; Chai & Mahesh 2012). Using the solved subgrid kinetic energy, the eddy-viscosity is then estimated by

$$\nu_t = C_\nu \Delta \sqrt{2K}. \tag{36}$$

In this paper, we will consider the one-equation model primarily as an example to illustrate the construction of an LES for the pollution of primordial gas in interstellar turbulence. For a compressible flow, the subgrid kinetic energy equation is given by

$$\begin{aligned}
&\frac{\partial(\overline{\rho}\,K)}{\partial t} + \frac{\partial(\overline{\rho}K\widetilde{v}_i)}{\partial x_i} = -\overline{\rho}\widetilde{S}_{ij}\tau_{ij} \\
&+ \left(\overline{p\frac{\partial v_i}{\partial x_i}} - \overline{p}\frac{\partial \widetilde{v}_i}{\partial x_i}\right) - (\overline{S_{ij}\sigma_{ij}} - \widetilde{S}_{ij}\overline{\sigma}_{ij}) \\
&+ \frac{\partial}{\partial x_i}\Bigg[\overline{\rho}\,\widetilde{v}_j\tau_{ij} + (\overline{v_j\sigma_{ij}} - \widetilde{v}_j\,\overline{\sigma}_{ij}) \\
&- \frac{1}{2}\overline{\rho}\,(\widetilde{v_j v_j v_i} - \widetilde{v_j v_j}\,\widetilde{v}_i) - (\overline{pv_i} - \overline{p}\,\widetilde{v}_i)\Bigg] \\
&+ \overline{\rho}(\widetilde{v_i f_i} - \widetilde{v}_i\,\widetilde{f}_i),
\end{aligned} \tag{37}$$

where the first term on the right-hand side represents the production of subgrid kinetic energy by the cascade from resolved scales. The two terms on the second line of the equation appeared earlier in the filtered temperature equation, corresponding to the pdV work (or pressure-dilation) and the viscous dissipation at subgrid scales. The pressure-dilation term is sometimes neglected for weakly compressible flows because it is difficult to model (e.g., Moin et al. 1991; Erlebacher et al. 1992), but in highly compressible flows the pdV work is not negligible and needs to be accounted for. Using direct numerical simulations of supersonic turbulence, PS10 showed that, despite its reversible nature, the pdV work tends to convert kinetic energy to thermal energy, and thus acts as a significant kinetic energy sink in addition to the viscous dissipation. Based on their results, one can model the pressure-dilation and viscous-dissipation terms together as $C_{\rm diss}\overline{\rho}K/\tau_{\rm sdyn} = C_{\rm diss}\sqrt{2}\overline{\rho}K^{3/2}/\Delta$, where the subgrid dynamical time, $\tau_{\rm sdyn}$, is assumed to be $\Delta/\sqrt{2K}$. Here, we have implicitly assumed that the filter size lies in the inertial range of the real flow and also assumed that the flow "driving" length at subgrid scales is $\simeq\Delta$. This may not be true if, for example, the supernova explosion is the main energy source for turbulence and the resolution scale is significantly larger than the size of supernova remnants. We do not consider this complexity here, as the one-equation subgrid model is used largely for an illustration purpose. The dimensionless parameter $C_{\rm diss}$ is expected to be a function of the subgrid Mach number, $M_s \equiv (2K/R\widetilde{T})^{1/2}$, and the dependence of $C_{\rm diss}$ on M_s may be determined using the simulation results of PS10.

The last of line of Equation (37) corresponds to the addition of kinetic energy at subgrid scales by the driving force, f_i. If the characteristic length scale of f_i is much larger the filter size, $f_i \simeq \widetilde{f}_i$, and $(\widetilde{v_i f_i} - \widetilde{v}_i\,\widetilde{f}_i)$ would be negligible, meaning that the driving force stores kinetic energy mainly at the resolved scales. On the other hand, a significant fraction of energy input from supernova explosions may be deposited primarily as subgrid kinetic energy, if the simulation does not resolve the typical size of supernova remnants (Scannapieco & Brüggen 2010). In that case, $\widetilde{f}_i \simeq 0$ for isotropically expanding supernova remnants, and the subgrid kinetic energy input can be estimated as the product of the supernova explosion energy and the local supernova rate per unit volume.

The four transport (or flux) terms in the third and fourth lines of Equation (37) are usually grouped and modeled together as a diffusion of the subgrid kinetic energy (Lilly 1966; Schumann 1975; Moeng 1984; Ghosal et al. 1995; Schmidt et al. 2006; Genin & Menon 2010; see, however, Chai & Mahesh 2012 for separate treatment of each individual term). Here, we adopt an eddy-diffusion assumption for the first three flux terms and approximate them together by $(\nu+\nu_k)\partial_i K$, where $\nu_k = C_k\Delta\sqrt{2K}$. The parameter C_k is sometimes set to be equal to C_ν in Equation (36) for the subgrid stress tensor (e.g., Kim & Menon 1999). In general, they may be different and need to treated separately (e.g., Schmidt et al. 2006). The last flux term on the fourth line of Equation (37) can be written as $\overline{\rho}R(\widetilde{T}v_i - \widetilde{T}\,\widetilde{v}_i) = \overline{\rho}Rq_i$, where the temperature flux, q_i, by subgrid motions is modeled by Equation (35). With these assumptions, we have (see Genin & Menon 2010)

$$\begin{aligned}
&\frac{\partial(\overline{\rho}\,K)}{\partial t} + \frac{\partial(\overline{\rho}K\widetilde{v}_i)}{\partial x_i} = -\overline{\rho}\widetilde{S}_{ij}\tau_{ij} - C_{\rm diss}\frac{\sqrt{2}\overline{\rho}K^{3/2}}{\Delta} \\
&+ \frac{\partial}{\partial x_i}\left[\overline{\rho}(\nu+\nu_k)\frac{\partial K}{\partial x_i} + \overline{\rho}R\frac{\nu_t}{Pr_t}\left(\frac{\partial \widetilde{T}}{\partial x_i}\right)\right] + \overline{\rho}(\widetilde{v_i f_i} - \widetilde{v}_i\,\widetilde{f}_i),
\end{aligned} \tag{38}$$

which is in a closed form and can be evolved to obtain the subgrid turbulent energy.

We next consider the filtered temperature equation (32). We use the eddy-diffusivity model, Equation (35), for the temperature flux, q_i, on the second line, and model the

pressure-dilation and viscous-dissipation terms as in Equation (38). With these assumptions, we obtain

$$C_{\rm V}\frac{\partial(\overline{\rho}\,\widetilde{T})}{\partial t}+C_{\rm V}\frac{\partial(\overline{\rho}\,\widetilde{T}\,\widetilde{v}_i)}{\partial x_i}=-\overline{\rho}R\widetilde{T}\,\frac{\partial\widetilde{v}_i}{\partial x_i}+\widetilde{S}_{ij}\,\overline{\sigma}_{ij}+\frac{\partial}{\partial x_i}\left(\overline{\kappa}\frac{\partial\widetilde{T}}{\partial x_i}\right)+C_{\rm V}\frac{\partial}{\partial x_i}\left(\overline{\rho}\frac{\nu_{\rm t}}{Pr_{\rm t}}\frac{\partial\widetilde{T}}{\partial x_i}\right)+C_{\rm diss}\frac{\sqrt{2}\overline{\rho}K^{3/2}}{\Delta}+\overline{\rho}\,\widetilde{\Gamma}-\overline{\rho}\,\widetilde{\Lambda},\quad(39)$$

where the thermal conductivity term can be neglected if $\overline{\kappa}\ll\overline{\rho}C_{\rm V}\alpha_{\rm t}$. An alternative approach to obtain $\widetilde{T}$ is to model and evolve the equation of the filtered total energy, $\widetilde{E}(\equiv(12)\widetilde{v}_i\widetilde{v}_i+K+C_{\rm V}\widetilde{T})$, per unit mass (e.g., Vreman et al. 1997; Kosovic et al. 2002; Schmidt et al. 2006; Park & Mahesh 2007; Genin & Menon 2010; Scannapieco & Brüggen 2010; Chai & Mahesh 2012).

To solve the LES and K equations, one needs to determine four parameters, C_ν, $Pr_{\rm t}$, $C_{\rm diss}$, and $C_{\rm k}$. Traditionally, these are assumed to be positive constants and specified a priori and then tuned by testing against experiments or numerical simulations. On the other hand, this approach has the weaknesses of failing to fully account for the flow-dependence of these parameters, as well as not allowing the backscatter of the subgrid kinetic energy to the resolved scales, which does occur in some local regions of a turbulent flow (Piomelli et al. 1991). These limitations motivated a dynamic procedure for subgrid modeling where the model coefficients are computed in a localized and adaptive way using the flow structures at resolved scales and the assumption of scale invariance (e.g., Germano et al. 1991; Moin et al. 1991; Germano 1992; Lilly 1992; Ghosal et al. 1995; Kim & Menon 1999; Schmidt et al. 2006; Park & Mahesh 2007; Genin & Menon 2010; Chai & Mahesh 2012).

Here, we have restricted our attention to the eddy-viscosity models and focused particularly on the one-equation model. The interested reader is referred to, e.g., Vreman et al. (1997), Meneveau & Katz (2000), and De Stefano et al. (2008), for non-eddy-viscosity subgrid models and their dynamic versions. Two-equation subgrid models have also been developed, which, in addition to the subgrid kinetic energy, evolve another subgrid quantity, such as the dissipation rate (e.g., Gallerano et al. 2005) or the characteristic length scale of subgrid turbulent motions (e.g., Fang & Menon 2006; Dimonte & Tipton 2006; Scannapieco & Brüggen 2010).

7.2. Subgrid Model for Turbulent Mixing and the Pollution of Pristine Gas

In this subsection, we construct a subgrid model for the pollution of primordial gas in early galaxies. We first consider the equation for the filtered concentration field, which provides a general illustration for subgrid modeling of turbulent mixing. Applying the filtering procedure to the advection-diffusion equation (1) gives

$$\frac{\partial(\overline{\rho}\,\widetilde{C})}{\partial t}+\frac{\partial(\overline{\rho}\,\widetilde{v}_i\widetilde{C})}{\partial x_i}=-\frac{\partial(\overline{\rho}g_i)}{\partial x_i}+\frac{\partial}{\partial x_i}\left(\overline{\rho\gamma\frac{\partial C}{\partial x_i}}\right)+\overline{\rho}\widetilde{S},\quad(40)$$

where $g_i=\widetilde{v_iC}-\widetilde{v}_i\widetilde{C}$ is the concentration flux caused by subgrid turbulent motions. The equation is similar to the temperature equation (32) except for the pressure-dilation and viscous-dissipation terms. Analogous to the subgrid temperature flux, q_i, one may adopt an eddy-diffusivity assumption for the concentration flux, $g_i=-\gamma_{\rm t}\partial_i\widetilde{C}$, yielding

$$\frac{\partial(\overline{\rho}\,\widetilde{C})}{\partial t}+\frac{\partial(\overline{\rho}\,\widetilde{v}_i\widetilde{C})}{\partial x_i}=\frac{\partial}{\partial x_i}\left(\overline{\rho}(\gamma+\gamma_{\rm t})\frac{\partial\widetilde{C}}{\partial x_i}\right)+\overline{\rho}\widetilde{S},\quad(41)$$

where we also assumed $\overline{\rho\gamma\partial_iC}\simeq\overline{\rho}\gamma\partial_i\widetilde{C}$. The eddy diffusivity, $\gamma_{\rm t}$, is of the same order as the eddy viscosity, and the subgrid Schmidt number $Sc_{\rm t}(\equiv\nu_{\rm t}/\gamma_{\rm t})$ is sometimes set to be the same as the subgrid Prandtl number $Sc_{\rm t}=Pr_{\rm t}\approx0.7$ (e.g., Jaberi et al. 1999). Somewhat smaller values, $Sc_{\rm t}\simeq0.3$–0.4, have also been proposed (e.g., Pitsch & Steiner 2000; Jimenez et al. 2001). $Sc_{\rm t}$ can also be computed from the local flow structures using the dynamic procedure discussed above (see, e.g., Moin et al. 1991; Pierce & Moin 1998). For the LES of interstellar turbulence, $\gamma_{\rm t}$ is expected to be much larger than the molecular diffusivity γ.

Similar to the subgrid kinetic energy, we can derive an equation for the subgrid concentration variance, defined as $\widetilde{(\delta C)^2}=\widetilde{C^2}-(\widetilde{C})^2$. The equation reads

$$\begin{aligned}&\frac{\partial(\overline{\rho}\,\widetilde{(\delta C)^2})}{\partial t}+\frac{\partial(\overline{\rho}\,\widetilde{v}_i\,\widetilde{(\delta C)^2})}{\partial x_i}\\&=-2\overline{\rho}\,g_i\frac{\partial\widetilde{C}}{\partial x_i}-2\left[\overline{\rho\gamma\left(\frac{\partial C}{\partial x_i}\right)^2}-\overline{\rho\gamma\left(\frac{\partial C}{\partial x_i}\right)}\frac{\partial\widetilde{C}}{\partial x_i}\right]\\&\quad+\frac{\partial}{\partial x_i}\left[2\overline{\rho}\,\widetilde{C}\,g_i+\left(\overline{\rho\gamma\frac{\partial C^2}{\partial x_i}}-2\widetilde{C}\,\overline{\rho\gamma\frac{\partial C}{\partial x_i}}\right)-\overline{\rho}(\widetilde{C^2v_i}-\widetilde{C^2}\,\widetilde{v}_i)\right]\\&\quad+2\overline{\rho}(\widetilde{SC}-\widetilde{S}\,\widetilde{C}),\end{aligned}\quad(42)$$

which is in close analogy to Equation (37). The term $-2\overline{\rho}g_i\partial_i\widetilde{C}$ represents the production of the concentration variance by the scalar cascade from the resolved scales. The second term on the second line corresponds to the subgrid scalar dissipation by molecular diffusivity. We model the dissipation term as $\overline{\rho}\widetilde{(\delta C)^2}/\tau_{\rm sm}$ (see Equation (7)), where the subgrid mixing timescale $\tau_{\rm sm}$ is expected to scale with the subgrid dynamical time, $\tau_{\rm sdyn}\equiv\Delta/\sqrt{2K}$. Parameterizing $\tau_{\rm sm}$ with respect to $\tau_{\rm sdyn}$, we set the dissipation term to $C_{\rm m}\overline{\rho}\sqrt{2K}\widetilde{(\delta C)^2}/\Delta$, where $C_{\rm m}=\tau_{\rm sdyn}/\tau_{\rm m}$. The parameter $C_{\rm m}$ depends on the local subgrid Mach number, $M_{\rm s}=(2K/RT)^{1/2}$, and also on the subgrid length scale $L_{\rm sp}$ at which the pollutants are injected, and it can be calibrated using the simulation results of PS10, who tabulated the mixing timescale of passive scalars forced at different length scales in turbulent flows at a range of Mach numbers. If the pollutants are forced at large scales and the subgrid fluctuations are contributed primarily by the cascade from resolved scales, and it is appropriate to set $L_{\rm sp}=\Delta$. However, $L_{\rm sp}$ could be smaller than the resolution scale, Δ, if, for example, multiple supernovae explode in a single computational cell (e.g., Scannapieco & Brüggen 2010). Finally, we model the transport term on the third line of Equation (42) together as a diffusion term, $\partial_i((\gamma+\gamma_{t2})\overline{\rho}\partial_i\widetilde{\delta C^2})$. The eddy diffusivity, γ_{t2}, here is likely to be close to $\gamma_{\rm t}$ in the $\widetilde{C}$ equation, although it is not clear if they are exactly equal (see below). These assumptions result in a closed variance equation (cf. Jimenez et al. 2001),

$$\begin{aligned}&\frac{\partial(\overline{\rho}\,\widetilde{(\delta C)^2})}{\partial t}+\frac{\partial(\overline{\rho}\,\widetilde{v}_i\widetilde{(\delta C)^2})}{\partial x_i}=2\overline{\rho}\gamma_{\rm t}\left(\frac{\partial\widetilde{C}}{\partial x_i}\right)^2-C_{\rm m}\overline{\rho}\frac{\sqrt{2K}\widetilde{(\delta C)^2}}{\Delta}\\&\quad+\frac{\partial}{\partial x_i}\left[\overline{\rho}(\gamma+\gamma_{t2})\frac{\partial\widetilde{(\delta C)^2}}{\partial x_i}\right]+2\overline{\rho}(\widetilde{SC}-\widetilde{S}\widetilde{C}),\end{aligned}\quad(43)$$

which illustrates the basic picture for modeling the subgrid concentration fluctuations, and provides a useful guideline for formulating a subgrid model for the pollution of pristine gas. A dynamic procedure for the subgrid scalar variance and dissipation was developed in Pierce & Moin (1998).

The subgrid model we construct for the pollution of pristine gas is based on the PDF formulation in the context of LES. Applying a Favre filter, Equation (28), to the fine-grained concentration PDF $\phi = \delta(Z - C(\mathbf{x}, t))$, we define a density-weighted PDF at the resolution scale,

$$\widetilde{\phi}(Z; \mathbf{x}, t) = \frac{\overline{\rho\phi(Z; \mathbf{x}, t)}}{\overline{\rho}}. \tag{44}$$

An exact equation for the filtered PDF, $\widetilde{\phi}$, is derived in the Appendix,

$$\begin{aligned}\frac{\partial(\overline{\rho}\,\widetilde{\phi})}{\partial t} + \frac{\partial}{\partial x_i}(\overline{\rho}\,\widetilde{\phi}\,\widetilde{[v_i|C=Z]}_\rho) &= \frac{\partial}{\partial x_i}\left(\overline{\rho\gamma\frac{\partial\phi}{\partial x_i}}\right) \\ &- \frac{\partial^2}{\partial Z^2}\left(\overline{\rho}\,\widetilde{\phi}\left[\gamma\left(\frac{\partial C}{\partial x_i}\right)^2 \middle| C = Z\right]_\rho\right) \\ &- \frac{\partial}{\partial Z}(\overline{\rho}\,\widetilde{\phi}\,\widetilde{[S|C=Z]}_\rho),\end{aligned} \tag{45}$$

where $\widetilde{[\cdots|C=Z]}_\rho$ denotes density-weighted filtering conditioned on the local concentration value. The definition of the conditional filtering is given in the Appendix.

Equation (45) is essentially identical to Equations (2) and (4) for the ensemble-defined PDF, Φ. This implies that, first, the same closure problem exists for the advection and diffusivity terms in Equation (45), and second, the PDF closure models in the ensemble context can be applied to the filtered PDF equation. Although our primary goal is not to solve the equation for the entire filtered PDF, we give an outline for modeling the PDF equation, which is helpful for understanding our LES approach for the pristine fraction. We first consider the advection term, which is responsible for the transport of the PDF between different regions by the turbulent velocity. We write it in two terms, $\widetilde{\phi}\,\widetilde{[v_i|C=Z]}_\rho = \widetilde{\phi}\,\widetilde{v}_i + \widetilde{\phi}(\widetilde{[v_i|C=Z]}_\rho - \widetilde{v}_i)$, and then modeling the second term with an eddy-diffusivity assumption gives $\widetilde{\phi}\,\widetilde{[v_i|C=Z]}_\rho = \widetilde{\phi}\,\widetilde{v}_i - \gamma_{t\phi}\partial_i\widetilde{\phi}$, where $\gamma_{t\phi}$ is the eddy diffusivity for the PDF flux by the subgrid motions (see, e.g., Gao & O'Brien 1993; Colucci et al. 1998; Jaberi et al. 1999). The filtered PDF equation then becomes

$$\begin{aligned}\frac{\partial(\overline{\rho}\,\widetilde{\phi})}{\partial t} + \frac{\partial}{\partial x_i}(\overline{\rho}\,\widetilde{\phi}\,\widetilde{v}_i) &= \frac{\partial}{\partial x_i}\left(\overline{\rho}(\gamma_{t\phi}+\gamma)\frac{\partial\widetilde{\phi}}{\partial x_i}\right) \\ &- \frac{\partial^2}{\partial Z^2}\left(\overline{\rho}\,\widetilde{\phi}\left[\gamma\left(\frac{\partial C}{\partial x_i}\right)^2 \middle| C = Z\right]_\rho\right) \\ &- \frac{\partial}{\partial Z}(\overline{\rho}\,\widetilde{\phi}\,\widetilde{[S|C=Z]}_\rho),\end{aligned} \tag{46}$$

where we also assumed that $\overline{\rho\gamma\,\partial_i\phi} \simeq \overline{\rho}\gamma\,\partial_i\widetilde{\phi}$ (see, e.g., Jaberi et al. 1999). Taking the first-order moment of Equation (46) gives an equation for the filtered concentration $\widetilde{C}$, which is the same as Equation (41) except that γ_t is replaced by $\gamma_{t\phi}$. This suggests that $\gamma_{t\phi} \simeq \gamma_t$ (Gao & O'Brien 1993). Also, using the second-order moment of Equation (46), we can derive an equation for the subgrid variance, $\widetilde{(\delta C)^2}$, which is the same as Equation (43) except that $\gamma_{t\phi}$ replaces both γ_t and γ_{t2}. This indicates that the eddy diffusivities for the concentration mean (γ_t) and variance (γ_{t2}) are automatically set to be equal if one models the advection term in the PDF equation with an eddy-diffusivity closure.

The term on the second line of Equation (46) represents homogenization by molecular diffusivity, and can be modeled using established PDF closure approximations for turbulent mixing, such as those discussed in Section 3.1. In Section 6.1, we derived an expression for the source term in the ensemble PDF equation. Using the same method, we estimate the source term in Equation (46) for the filtered PDF. The source term for new metals from supernovae is $\overline{\dot{n}}_{\rm SN} m_{\rm ej}(\delta(Z - Z_{\rm ej}) - \widetilde{\phi})$, where $\overline{\dot{n}}_{\rm SN}(\mathbf{x}, t)$ is the filtered number rate of supernova explosions per unit volume, and ejecta from each supernova is assumed to have the same mass $m_{\rm ej}$, with metallicity $Z_{\rm ej}$. Again the $-\widetilde{\phi}$ term ensures the conservation of the total probability. With the supernova source term in the filtered PDF equation, it is straightforward to calculate the source terms in the filtered concentration and variance equations (41) and (43). We find that the source terms are $\overline{\dot{n}}_{\rm SN} m_{\rm ej}(Z_{\rm ej} - \widetilde{C})$ and $\overline{\dot{n}}_{\rm SN} m_{\rm ej}[(Z_{\rm ej} - \widetilde{C})^2 - \widetilde{\delta C^2}]$ in the $\widetilde{C}$ and $\widetilde{\delta C^2}$ equations, respectively. If a continuous infall of pristine gas from the halo exists during the formation and evolution of a galaxy, one can maintain a mass flux at the boundary of the simulation box and set $\widetilde{\phi} = \delta(Z)$ as the boundary condition for the (filtered) concentration PDF.

We finally consider modeling the pollution of the primordial gas in an LES. Clearly, the fine-grained pristine fraction, $P(Z_{\rm c}; \mathbf{x}, t)$, at a given point is an integral of the fine-grained PDF, $\phi(Z; \mathbf{x}, t)$, from $Z = 0$ to the threshold, $Z_{\rm c}$, and similarly, the filtered pristine fraction, $\widetilde{P}$, at the resolution scale is given by

$$\widetilde{P}(Z_{\rm c}; \mathbf{x}, t) = \int_0^{Z_{\rm c}} \widetilde{\phi}(Z; \mathbf{x}, t) dZ. \tag{47}$$

We can therefore derive an equation for $\widetilde{P}$ by integrating the filtered PDF Equation (45) from 0 to $Z_{\rm c}$. Performing such an integration for the advection term in Equation (45) yields $\widetilde{Pv_i}$, which corresponds to the flux of the pristine fraction into and out of a computational cell due to the transport/advection of the turbulent velocity (see Section 2.1). The term can be rewritten as $\widetilde{P}\,\widetilde{v}_i + (\widetilde{Pv_i} - \widetilde{P}\,\widetilde{v}_i)$, where the term in the brackets is the pristine fraction flux caused by the subgrid turbulent motions. We model this subgrid flux with an eddy-diffusion assumption,

$$\widetilde{Pv_i} - \widetilde{P}\widetilde{v}_i = -\gamma_{\rm P}\partial_i\widetilde{P}, \tag{48}$$

where $\gamma_{\rm P}$ is the eddy diffusivity for the pristine fraction. We use the self-convolution models (Section 3.2) for the effect of the diffusivity term on the pristine fraction. Integrating the supernova source term from 0 to $Z_{\rm c}$ gives $-\overline{\dot{n}}_{\rm SN} m_{\rm ej}\widetilde{P}$. With these models and assumptions, we obtain

$$\begin{aligned}\frac{\partial(\overline{\rho}\,\widetilde{P})}{\partial t} + \frac{\partial}{\partial x_i}(\overline{\rho}\,\widetilde{P}\,\widetilde{v}_i) &= \frac{\partial}{\partial x_i}\left(\overline{\rho}(\gamma+\gamma_{\rm P})\frac{\partial\widetilde{P}}{\partial x_i}\right) \\ &- \frac{n_{\rm s}}{\tau_{\rm scon}}\widetilde{P}(1 - \widetilde{P}^{1/n_{\rm s}}) - \overline{\dot{n}}_{\rm SN} m_{\rm ej}\widetilde{P},\end{aligned} \tag{49}$$

where it is also assumed $\overline{\rho\gamma\,\partial_i P} = \overline{\rho}\gamma\widetilde{P}$, and $n_{\rm s}$ and $\tau_{\rm scon}$ correspond to the parameters, n and $\tau_{\rm con}$, in the self-convolution

models discussed in Section 3. As γ is likely much smaller than γ_P, the pristine fraction flux due to the molecular diffusivity can be neglected. The choice for n_s and τ_{scon} according to the turbulence and pollutant conditions at subgrid scales will be described and discussed below. If a pristine mass flux is enforced at the boundary of the simulation box to imitate the primordial infall gas, one should set $\widetilde{P} = 1$ as a boundary condition.

A comparison of Equation (49) with Equation (43) shows that both equations have transport or flux terms, a mixing/homogenization term by the molecular diffusivity, and a source term. A similar analogy also exists with the equation for the subgrid kinetic energy, Equation (38). There is, however, an interesting difference. The concentration variance equation has a term that tends to increase the subgrid variance, representing the scalar cascade from the resolved scales. On the other hand, there is no such production term in the $\widetilde{P}$ equation, because no mechanism exists in the mixing process that can produce pristine gas at subgrid scales.

To derive the equation for the filtered pristine fraction, we could also have started from Equation (46) for the filtered PDF, where the advection term is already modeled by an eddy-diffusion assumption. In that case, we would have found that the primordial flux due to subgrid turbulent motions is given by $-\gamma_{t\phi}\partial_i \widetilde{P}$. This suggests that, when applying an eddy-diffusivity closure to the advection term in the filtered PDF equation, it is implicitly assumed that the three eddy diffusivities, γ_t, γ_{t2}, and γ_P, respectively, for the mean, variance, and the pristine fraction, are the same and all equal to $\gamma_{t\phi}$. The quantitative accuracy of this assumption is not clear, although all the eddy diffusivities are expected to be of the same order. A simple estimate for γ_P is to scale it with the eddy viscosity as, $\gamma_P = \nu_t/Sc_P$, with the Schmidt number Sc_P for the pristine fraction in the range from 0.3 to 0.7, as in the case of γ_t discussed earlier (see the text below Equation (41)).

To implement Equation (49) in an LES for the pollution of primordial gas in early galaxies, we now only need to specify the two parameters, n_s and τ_{scon}, from the self-convolution model. When using the convolution model in Equation (49), we have implicitly assumed that statistical homogeneity is restored at the resolution scale, Δ, because the applicability of the model is tested and confirmed only in statistically homogeneous turbulent flows. With this assumption, n_s and τ_{scon} can be determined using our simulation results. These parameters are functions of the flow Mach number and the pollutant injection scale relative to the flow driving scale. The subgrid Mach number, M_s, can be easily computed by $(2K/R\widetilde{T})^{1/2}$ in the one-equation model, where K and $\widetilde{T}$ are, respectively, the subgrid kinetic energy and the filtered gas temperature. The subgrid source injection scale, L_{sp}, in a computational cell would be close to the cell size, Δ, if the pollutant source was transported into the cell by advection, or if only one supernova exploded in the cell. In that case, it is appropriate to set $L_{sp} = \Delta$. On the other hand, if multiple supernova explosions occurred in a single cell, then L_{sp} would roughly go like the number of supernovae to $-1/3$ power, assuming a random distribution. We assume that the subgrid flow "driving" scale, L_{sf}, is roughly given by the cell size, Δ.

With M_s and the ratio L_{sp}/L_{sf}, one can fix the parameters, n_s and τ_{scon}, by interpolating Tables 2–4 in Section 5.4.6, or using the fits given in Equations (22)–(24). The timescales τ_{con1} and τ_{con2} given in Tables 2 and 4 are normalized to the flow dynamical time, therefore the values for τ_{scon} are in units of the subgrid dynamical time, $\tau_{sdyn}(\equiv \Delta/\sqrt{2K})$. We point out that there is an uncertainty in the applicability of our tabulated parameters to computation cells with supernova explosions. In these cells, the effective driving is likely better described by a pure compressive force rather than solenoidal. As discussed earlier, this may affect the parameters in the convolution model. Future simulations are needed to investigate the potential dependence of the parameters with the compressibility of the driving force. The convolution timescale also has a dependence on the threshold metallicity, Z_c, relative to the mean concentration (see Section 5.4.4). Thus, to determine τ_{scon}, we need to compute the ratio, $Z_c/\widetilde{C}$, of the threshold to the mean, $\widetilde{C}$, in a cell. For that purpose, it is necessary to solve the filtered concentration equation (41) to keep track of $\widetilde{C}$ in all computational cells. As mentioned earlier, the source term in this equation is given by $\overline{\dot{n}}_{SN} m_{ej}(Z_{ej} - \widetilde{C})$. Based on our results in Section 5.4.4, for small values of $Z_c/\widetilde{C}$ ($\lesssim 10^{-3}$), one can use a weak power-law scaling (see Section 5.4.4) to rescale the convolution timescales listed in Tables 2 and 4. However, it is possible that $\widetilde{C}$ in a computational cell is close to or even smaller than Z_c. As discussed in Section 5.4.4, in the extreme case with $\widetilde{C} \lesssim Z_c$, the evolution of $\widetilde{P}$ in a cell would be qualitatively different from the prediction of the self-convolution models. A careful treatment is thus needed for cells with $\widetilde{C}$ close to or smaller than Z_c. How the fraction, $\widetilde{P}$, evolves under this situation is not explored in the current work, and we defer it to a future paper.

In the subgrid model outlined above for the pristine fraction, we adopted a simple approach to fix the model parameters, prescribing them based on our simulation results and previous work on LES. An interesting question is whether the parameters can be determined dynamically using the resolved local flow and scalar structures. It seems highly uncertain whether the dynamic procedure is applicable at all to the problem of how the pristine gas is polluted in a turbulent flow. As mentioned earlier, the validity of the dynamical procedure relies on the existence of scale invariance. This can be justified, e.g., for the cascade of kinetic energy or the concentration variance, based on Kolmogorov's similarity theory of turbulence. However, unlike kinetic energy or the scalar variance, which are second-order statistical measures, the pristine fraction corresponds to the extreme PDF tail, and it is unknown whether scale invariance exists for such a high-order quantity. Exploring the possibility of developing a dynamic subgrid model for the pristine gas fraction would be an interesting topic for a future study.

8. CONCLUSIONS

The shift from Pop III to normal star formation is a global transition of the universe that is dependent on mixing on scales smaller than a parsec (Pan & Scalo 2007). This means that numerical simulations of this process will only be possible if we first develop a deep understanding of the fundamental physics of how the pristine material is polluted in turbulent flows. In an earlier paper (PSS), we developed a theoretical approach to modeling this process based on the PDF method for passive scalar mixing in statistically homogeneous turbulence, and we explored the evolution of the pristine fraction, $P(Z_c, t)$, defined as the mass fraction of the flow with pollutant concentration below a tiny threshold Z_c. Then we used numerical simulations to show that a class of PDF models, called self-convolution models, provide successful fitting functions to the solution of $P(Z_c, t)$, which corresponds to the far left tail of the concentration PDF.

The convolution models are based on the physical picture of turbulence stretching pollutants and causing a cascade of

concentration structures toward small scales. Mixing then occurs as the scale of the structures becomes sufficiently small for molecular diffusivity to operate efficiently, and the homogenization between neighboring structures corresponds to a convolution of the concentration PDF. The picture suggests that the mixing/pollution timescale is determined by the turbulent stretching rate at the scale where the pollutants are injected, and the main result of PSS was the prediction for the pristine fraction evolution, i.e., Equation (15), by the generalized self-convolution model. For convenience, we repeat Equation (15) here,

$$\frac{dP(Z_c,t)}{dt} = -\frac{n}{\tau_{con}} P(1-P^{1/n}), \tag{50}$$

where τ_{con} is the timescale for the PDF convolution, and the parameter n is interpreted as an indicator of the degree of spatial locality of the PDF convolution process. A smaller n corresponds to more local convolution and broader PDF tails.

In the present work, we briefly reviewed the formulation of PSS, and conducted a systematic numerical study of the turbulent pollution process, exploring an extended parameter space. We simulated four statistically homogeneous turbulent flows with rms Mach number M ranging from 0.9 to 6.2. In each flow, we evolved 20 decaying scalars with different initial pollutant fractions, H_0, and different pollutant injection scales, L_s. The simulation data further confirmed the validity of the convolution model and allowed us to measure the model parameters, n and τ_{con}, in Equation (50) over a wide range of turbulence and pollutant conditions. Consistent with PSS, we find that, if the initial pollutant fraction $H_0 \gtrsim 0.1$, the simulation results for the pristine fraction can be well fit by the convolution model prediction, Equation (50), with properly chosen parameters. Equation (50) is solved by

$$P(Z_c,t) = \frac{P_0}{\left[P_0^{1/n} + \left(1-P_0^{1/n}\right)\exp\left(t/\tau_{con2}\right)\right]^n}, \tag{51}$$

where P_0 is the initial pristine fraction, and we have denoted the convolution timescale as τ_{con2} for these scalar fields. Using Equation (51) to fit the simulation data yielded best-fit parameters n and τ_{con2}. On the other hand, if $H_0 \lesssim 0.1$, the evolution of $P(Z_c,t)$ shows different behaviors at early and late times. In the early phase, the PDF convolution occurs locally in space due to the limited amount of pollutants, and the pristine fraction evolution follows the prediction of the "discrete" convolution model with $n = 1$, i.e.,

$$P(Z_c,t) = \frac{P_0}{P_0 + (1-P_0)\exp\left(t/\tau_{con1}\right)}, \tag{52}$$

where the convolution timescale for the early phase is denoted as τ_{con1}. Once a significant fraction (0.2–0.3) of flow is polluted, the pristine fraction evolves in the same way as the scalar fields with $H_0 \gtrsim 0.1$. We therefore named the convolution timescale as τ_{con2} for both scalars with $H_0 \gtrsim 0.1$ and the late phases of $H_0 \lesssim 0.1$ scalars (see Section 5.4). A successful two-phase fitting scenario was adopted for scalars fields with $H_0 \lesssim 0.1$, which connects Equations (52) and (51) for early and late times.

We examined the dependence of the model parameters on the flow Mach number, M. We found that the convolution timescales, τ_{con1} and τ_{con2}, normalized to the flow dynamical time increase by $\simeq$20% as M goes from 0.9 to 2.1 and then saturates at $M \gtrsim 2$. This is similar to the behavior of the variance decay timescale, τ_m, as a function of M. For $H_0 \gtrsim 0.1$ scalars or the late phase of scalars with $H_0 \lesssim 0.1$, the parameter n decreases with increasing M, indicating that the PDF convolution proceeds more locally in supersonic turbulence with larger M. The decrease of n is related to broader concentration PDF tails at higher M, corresponding to a larger pristine fraction at the same concentration variance.

The pristine fraction evolution also depends on the pollutant injection scale L_s. As L_s deceases, the pollution of the pristine gas is faster and the timescales, τ_{con1} and τ_{con2}, decrease. This is expected as the mixing timescale scales with the eddy turnover time at L_s. For scalars with $H_0 \gtrsim 0.1$ or the late phase of $H_0 \lesssim 0.1$ scalars, the parameter n becomes smaller as L_s decreases because, intuitively, the convolution is more local if the pollutants are injected at smaller scales.

The dependence of the model parameters, n, τ_{con1}, and τ_{con2}, on the turbulence and pollutant properties is summarized in Tables 2–4, and for convenience we have fit these results with simple functions as

$$\tau_{con1} = [0.225 - 0.055\exp(-M^{3/2}/4)] \times \left(\frac{L_p}{L_f}\right)^{0.63}\left(\frac{Z_c}{10^{-7}\langle Z\rangle}\right)^{0.015}, \tag{53}$$

$$\tau_{con2} = [0.335 - 0.095\exp(-M^{2}/4)] \times \left(\frac{L_p}{L_f}\right)^{0.63}\left(\frac{Z_c}{10^{-7}\langle Z\rangle}\right)^{0.02}, \quad \text{and} \tag{54}$$

$$n = 1 + 11\ \exp(-M/3.5)\left(\frac{L_p}{L_f}\right)^{1.3}, \tag{55}$$

which are applicable for all Mach numbers and pollution properties, as long as $L_p \leqslant L_f$. Note that unlike Equations (50) and (51), these fits are for convenience only and not based on an underlying physical picture. We showed that the model is valid for $Z_c \lesssim 10^{-3}\langle Z\rangle$, where τ_{con1} and τ_{con2} only have a weak dependence on Z_c (Section 5.4.4). If Z_c is close to or larger than $\langle Z\rangle$, the model is no longer applicable, and we defer a study of this situation to a later work. We also tested the convergence of the model parameters with the numerical resolution (Section 5.4.5). The parameters n and τ_{con} may have a dependence on the compressivity of the driving force, which will be systematically examined in a future work.

To apply our model and simulation results to the mixing of heavy elements in the ISM, we specified the source term in the concentration PDF equation, accounting for the effects of new metals from supernova explosions and the possible infall of pristine gas from the halo or the intergalactic medium. These two sources force spikes in the PDF at high and low concentration values, respectively. With the source term, we derived an equation (Equation (25)) for the global pristine fraction in early galaxies. A description for how to use the equation and our simulation results to estimate the primordial gas fraction was given in Section 6. We discussed the timescales of relevant processes that control how and how fast the pollution process proceeds. In particular, the spatial transport by turbulent motions over galactic scales may play an important role if the interstellar turbulence is driven at small scales, e.g., by supernova explosions.

Numerical simulations accounting for the interstellar environment at galactic scales are a valuable tool to study the pollution of primordial gas from a less idealized point of view. In fact, recent efforts to track metal mixing in the context of the formation

of protogalaxies have made significant improvements in tracking the spatial evolution of the metallicity, averaged over relatively large scales (e.g., Wise & Abel 2008). Greif et al. (2009, 2010) employed a turbulent diffusion formalism to mimic mixing by smoothing over the smoothed particle hydrodynamics (SPH) kernel, and a similar approach was used in the 10 Mpc SPH simulations by Maio et al. (2010) and Campisi et al. (2011), who assumed the initial metal pollution was spread over ≈kpc scales by cluster winds. Another recent simulation by Ritter et al. (2012) used a finite-difference code with adaptive mesh refinement coupled to Lagrangian tracer particles to keep track of the metals produced in an initially metal-free galaxy. Interestingly, they found that a cold supersonically turbulent core developed because of the fallback of metal-enhanced ejecta. However, because the resolution scale was much larger than the scales on which turbulence-enhanced molecular diffusivity operates (Pan & Scalo 2007), they could not resolve a sufficiently large range of scales to track the unmixed, primordial fraction.

To overcome limitations such as these, we have developed an LES approach based on our model and simulation results. In LESs, the flow quantities at resolved scales are directly computed, while the feedback effect of subgrid turbulent motions is modeled. To overcome the overpollution by numerical diffusion, a subgrid model was constructed to track the evolution of the concentration fluctuations below the resolution scale. Using the standard filtering procedure for the LES formulation, we derived an equation for the filtered concentration PDF representing metallicity fluctuations at subgrid scales, and discussed the treatment of each term in the equation. The core of our subgrid model is Equation (49) for the filtered pristine fraction (i.e., the pristine fraction in each computational cell), which was derived from the filtered PDF equation. Again, we repeat it here for convenience:

$$\frac{\partial(\overline{\rho}\,\widetilde{P})}{\partial t}+\frac{\partial}{\partial x_i}\left(\overline{\rho}\,\widetilde{P}\,\widetilde{v}_i\right)=\frac{\partial}{\partial x_i}\left(\overline{\rho}(\gamma+\gamma_{\rm P})\frac{\partial\widetilde{P}}{\partial x_i}\right)-\frac{n_{\rm s}}{\tau_{\rm scon}}\widetilde{P}(1-\widetilde{P}^{1/n_{\rm s}})-\overline{\dot{n}}_{\rm SN}m_{\rm ej}\widetilde{P}, \quad (56)$$

where $n_{\rm s}$ and $\tau_{\rm scon}$ are parameters for the subgrid pollution, corresponding to n and τ in our convolution model, $\gamma_{\rm P}$ is the eddy diffusivity for the pristine fraction, $\overline{\dot{n}}_{\rm SN}(\mathbf{x},t)$ is the filtered number rate of supernova explosions per unit volume, and each supernova is assumed to have an ejecta mass $m_{\rm ej}$. This equation adopts the commonly used eddy-diffusivity model for the transport effect of subgrid turbulent motions, and employs the convolution model for the pollution of the pristine gas within each cell. The implementation of our subgrid model was illustrated in the context of a one-equation LES model for the interstellar turbulence, which evolves the kinetic energy of subgrid turbulent motions. Together with the resolved temperature field, the subgrid kinetic energy specifies the turbulence properties in each cell, which are needed to calculate the eddy diffusivity in the transport term and to determine the parameters in the convolution model for the subgrid pollution. The convolution model parameters depend on the metal/supernova sources in each cell, and can be evaluated using our simulation results.

The resulting physically realistic model for the evolution of the unresolved primordial fraction serves as a prototype for future simulations aimed at interpreting many observations currently probing the nature of early galaxies. The continuing discovery of star-forming galaxies at $z\approx 7$–10 in broadband photometric searches, for example, (as in the Hubble UDF12 survey; Ellis et al. 2013) suggests that observations of galaxies with significant primordial fractions should soon become available. The situation for galaxies selected on the basis of strong Lyα emission (e.g., Cowie & Hu 1998; Rhoads et al. 2000) is even more promising, and it may only be a matter of time before several such galaxies are clearly identified as containing primordial stars recognizable by their large Lyα equivalent width and weak He II emission (Scannapieco et al. 2003; Jimenez & Haiman 2006). In fact, a recent detailed analysis of deep Subaru images by Inoue et al. (2011) strongly supports the interpretation that the mass fraction of stellar populations with extremely small metal abundances in $z\approx 3$ Lyα emitters may be 1%–10% by mass, based on their very strong rest frame Lyman continua. Based on similar diagnostics, Kashikawa et al. (2012) recently proposed a $z=6.5$ Lyα emitter as a Pop III candidate although enhanced Lyα emission from a clumpy, dusty medium (Neufeld 1991; Hansen & Oh 2006) cannot be ruled out conclusively in this case. If any of these galaxies are convincingly demonstrated to contain primordial stars, their evolution could only be simulated using an approach such as the one outlined here.

Currently, a more direct constraint on the evolution of primordial gas is based on the absence of metal lines in absorption line systems in the intergalactic medium. Fumagalli et al. (2011) used this approach to obtain upper limits of $Z<10^{-6}$ by mass in two Lyman limit systems associated with quasars at $z\sim 3.1$ and 3.4. Simcoe et al. (2012) used the lack of metal lines in a $z\approx 7$ quasar spectrum that shows a large neutral hydrogen column density to obtain an upper limit of $Z\approx 10^{-5}$–10^{-6}, depending on the whether the gas is bound in a galaxy or is diffuse intergalactic gas at that redshift. The implications of these measurements can only be fully explored through models such as ours, which capture the unresolved, unmixed fraction.

Finally, at least four examples of Galactic stars with [Fe/H] <-4.5 ($Z\lesssim 10^{-6.5}$) are known (e.g., Christlieb et al. 2002; Frebel et al. 2008; Norris et al. 2007; Caffau et al. 2011), although only one is not enhanced in carbon. Recently, Yong et al. (2012) have shown convincingly that the Milky Way metallicity PDF is still decreasing smoothly down to at least [Fe/H] $=-4.1$ ($Z\approx 10^{-6}$), without the sudden cutoff claimed in earlier work. Once the rather severe selection effects are understood, these measurements could also be directly compared with our models, and even allow their two main parameters to be calibrated outside of numerical simulations. In fact, our proposed LES is expected to give reliable predictions for any physical problem, astrophysical or otherwise, in which the unresolved, low concentration tail of the PDF needs to be tracked. Its numerical implementation and targeted application represents an extremely promising avenue for future studies.

We acknowledge support from NASA under theory Grant No. NNX09AD106 and Astrobiology Institute Grant 08-NAI5-0018 and from the National Science Foundation under grant AST 11-03608. All simulations were conducted at the Arizona State University Advanced Computing Center and the Texas Advanced Computing Center, using the FLASH code, a product of the DOE ASC/Alliances funded Center for Astrophysical Thermonuclear Flashes at the University of Chicago.

APPENDIX

FILTERED PDF EQUATION

We formulate a PDF approach for LESs of turbulent mixing. LESs based on the PDF method have been applied to study reacting turbulent flows (e.g., Gao & O'Brien 1993; Colucci et al. 1998; Jaberi et al. 1999; Pitsch 2006). We first derive an equation for the local fine-grained concentration PDF, and then apply the filtering procedure to obtain an exact equation for the filtered PDF at the resolution scale. The derivation is similar to that in Appendix A of PSS for the equation of the concentration PDF defined in a statistical ensemble.

We start with the definition of the fine-grained concentration PDF as a delta function,

$$\phi(Z;\mathbf{x},t)=\delta(Z-C(\mathbf{x},t)), \tag{A1}$$

because the concentration field in a given turbulent flow is single-valued at given position and time (PSS). Here, Z is the sampling variable. Since $\phi(Z;\mathbf{x},t)$ depends on t only through the variable $Z-C(\mathbf{x},t)$, the time derivative $\phi(Z;\mathbf{x},t)$ can be written as

$$\frac{\partial\phi(Z;\mathbf{x},t)}{\partial t}=-\frac{\partial\phi(Z;\mathbf{x},t)}{\partial Z}\frac{\partial C(\mathbf{x},t)}{\partial t}. \tag{A2}$$

Similarly, the spatial gradient of ϕ is given by

$$\frac{\partial\phi(Z;\mathbf{x},t)}{\partial x_i}=-\frac{\partial\phi(Z;\mathbf{x},t)}{\partial Z}\frac{\partial C(\mathbf{x},t)}{\partial x_i}. \tag{A3}$$

Using Equations (A2) and (A3) and the advection-diffusion equation (1), we have

$$\frac{\partial\phi(Z;\mathbf{x},t)}{\partial t}+v_i\frac{\partial\phi(Z;\mathbf{x},t)}{\partial x_i}=-\frac{\partial}{\partial Z}\left[\phi(Z;\mathbf{x},t)\left(\frac{1}{\rho}\frac{\partial}{\partial x_i}\left(\rho\gamma\frac{\partial C}{\partial x_i}\right)+S\right)\right], \tag{A4}$$

where we used the fact that, except $\phi(Z;\mathbf{x},t)$, all the quantities on the right-hand side are independent of Z.

Combining Equation (A4) with the continuity equation, we obtain

$$\frac{\partial(\rho\phi)}{\partial t}+\frac{\partial(\rho\phi v_i)}{\partial x_i}=-\frac{\partial}{\partial Z}\left[\rho\phi\left(\frac{1}{\rho}\frac{\partial}{\partial x_i}\left(\rho\gamma\frac{\partial C}{\partial x_i}\right)+S\right)\right], \tag{A5}$$

which was also derived in Appendix A of PSS. The diffusivity term in Equation (A5) can be rewritten as

$$-\frac{\partial}{\partial Z}\left[\rho\phi\left(\frac{1}{\rho}\frac{\partial}{\partial x_i}\left(\rho\gamma\frac{\partial C}{\partial x_i}\right)\right)\right]=\frac{\partial}{\partial x_i}\left(\rho\gamma\frac{\partial\phi}{\partial x_i}\right)-\frac{\partial^2}{\partial Z^2}\left(\rho\phi\gamma\left(\frac{\partial C}{\partial x_i}\right)^2\right), \tag{A6}$$

where the first term on the right-hand side is a spatial diffusion of the local PDF. Note that Equation (4) in Section 2.2 is derived by taking the ensemble average of this equation and using the definition and properties of the conditional ensemble average (see Appendix A of PSS).

We next apply a filtering procedure to Equation (A4). A convolution of $\phi(Z;\mathbf{x},t)$ with the filter function, G, gives a filtered PDF, $\overline{\phi}(Z;\mathbf{x},t)=\int_V\phi(Z;\mathbf{x}',t)G(\mathbf{x}-\mathbf{x}')dx'^3$, characterizing the concentration fluctuations within regions of the filter size (or resolution scale). For compressible turbulence, we define a filtered PDF with density weighting (Jaberi et al. 1999),

$$\widetilde{\phi}(Z;\mathbf{x},t)\equiv\frac{\overline{\rho\phi}}{\overline{\rho}}, \tag{A7}$$

which is a specific example of Equation (28). Using Equations (27) and (A7) in Equation (A5), we obtain the filtered PDF equation,

$$\frac{\partial(\overline{\rho}\,\widetilde{\phi})}{\partial t}+\frac{\partial(\overline{\rho v_i\phi})}{\partial x_i}=-\frac{\partial}{\partial Z}\left(\overline{\phi\frac{\partial}{\partial x_i}\left(\rho\gamma\frac{\partial C}{\partial x_i}\right)}\right)-\frac{\partial(\overline{\rho S\phi})}{\partial Z}. \tag{A8}$$

To write the equation in a more convenient form, we introduce conditional filtering based on the local concentration values.

For any variable A in the flow, we define a conditionally filtered quantity,

$$\overline{A|C=Z}=\frac{\overline{A\phi(Z;\mathbf{x},t)}}{\overline{\phi}}. \tag{A9}$$

Since the fine-grained PDF, ϕ, is a delta function, the definition is straightforward to understand: the conditionally filtered variable is the average over the set of points within a filter size satisfying $C(\mathbf{x},t)=Z$. It is analogous to the conditional average defined in the context of a statistical ensemble (see Section 2; PSS). We further introduce a density-weighted conditional filtering,

$$\widetilde{[A|C=Z]}_\rho=\frac{\overline{\rho A|C=Z}}{\overline{\rho|C=Z}}=\frac{\overline{\rho\phi A}}{\overline{\rho\phi}}, \tag{A10}$$

where the last step follows from Equation (A9). This definition is similar to Equation (3) for the density-weighted conditional average over an ensemble.

Combining Equations (A7) and (A10), we have $\overline{\rho\phi A}=\overline{\rho}\,\widetilde{\phi}\,\widetilde{[A|C=Z]}_\rho$. Applying this relation to the last three terms in Equations (A8), we obtain

$$\frac{\partial(\overline{\rho}\,\widetilde{\phi})}{\partial t}+\frac{\partial}{\partial x_i}(\overline{\rho}\,\widetilde{\phi}\,\widetilde{[v_i|C=Z]}_\rho)=-\frac{\partial}{\partial Z}\left(\overline{\rho}\,\widetilde{\phi}\left[\frac{1}{\rho}\frac{\partial}{\partial x_i}\left(\rho\gamma\frac{\partial C}{\partial x_i}\right)\,\middle|\,C=Z\right]_\rho\right)-\frac{\partial}{\partial Z}(\overline{\rho}\,\widetilde{\phi}\,\widetilde{[S|C=Z]}_\rho), \tag{A11}$$

which is equivalent to Equation (22) in Jaberi et al. (1999). Using Equation (A6) for the diffusivity term gives

$$\frac{\partial(\overline{\rho}\,\widetilde{\phi})}{\partial t}+\frac{\partial}{\partial x_i}(\overline{\rho}\,\widetilde{\phi}\,\widetilde{[v_i|C=Z]}_\rho)=\frac{\partial}{\partial x_i}\left(\overline{\rho\gamma\frac{\partial\phi}{\partial x_i}}\right)-\frac{\partial^2}{\partial Z^2}\left(\overline{\rho}\,\widetilde{\phi}\left[\gamma\left(\frac{\partial C}{\partial x_i}\right)^2\,\middle|\,C=Z\right]_\rho\right)-\frac{\partial}{\partial Z}\left(\overline{\rho}\,\widetilde{\phi}\,\widetilde{[S|C=Z]}_\rho\right). \tag{A12}$$

Note that Equation (A11) becomes identical to Equation (2) for the ensemble-defined PDF, if we replace $\overline{\rho}$, $\widetilde{\phi}$, and $\widetilde{[\cdots|C=Z]}_\rho$

by $\langle\rho\rangle$, Φ, and $\langle\cdots|C = Z\rangle_\rho$, respectively. The equivalence between the filtered PDF and the ensemble-defined PDF has been discussed in Section 2, based on the ergodic theorem and the assumption that statistical homogeneity is restored at the filter scale. Similar to the case of the ensemble PDF equation, the advection and diffusivity terms in Equations (A11) and (A12) need to be modeled due to the closure problem. In Section 7, we adopted an eddy-diffusivity assumption for the advection term, and the self-convolution models discussed in Section 3 may be applied to approximate the diffusivity term. Using the convolution PDF models and the results of our simulations, a subgrid model is constructed in Section 7 to investigate the pollution of primordial gas in early galaxies.

REFERENCES

Abel, T., Bryan, G., & Norman, M. 2000, ApJ, 540, 39
Bond, J. R., Arnett, W. D., & Carr, B. J. 1984, ApJ, 280, 825
Bromm, V., Coppi, P. S., & Larson, R. B. 2002, ApJ, 564, 23
Bromm, V., & Loeb, A. 2003, Natur, 425, 812
Bromm, V., & Yoshida, N. 2011, ARA&A, 49, 373
Brook, C. B., Kawata, D., Scannapieco, E., Martel, H., & Gibson, B. K. 2007, ApJ, 661, 10
Caffau, E., Bonifacio, P., Franois, P., et al. 2011, Natur, 477, 67
Campisi, M. A., Maio, U., Salvaterra, R., & Ciardi, B. 2011, MNRAS, 416, 2760
Cayrel, R., Depagne, E., Spite, M., et al. 2004, A&A, 416, 1117
Chai, X., & Mahesh, K. 2012, JFM, 699, 385
Chen, H., Chen, S., & Kraichnan, R. H. 1989, PhRvL, 63, 2657
Christlieb, N., Bessell, M. S., Beers, T. C., et al. 2002, Natur, 419, 904
Clark, P. C., Glover, S. C. O., Klessen, R. S., & Bromm, V. 2011a, ApJ, 727, 110
Clark, P. C., Glover, S. C. O., Smith, R. J., et al. 2011b, Sci, 331, 1040
Colella, P., & Glaz, H. M. 1985, JCoPh, 59, 264
Colella, P., & Woodward, P. R. 1984, JCoPh, 54, 174
Colucci, P. J., Jaberi, F. A., Givi, P., & Pope, S. B. 1998, PhFl, 10, 499
Cowie, L. L., & Hu, E. M. 1998, AJ, 115, 1319
Curl, S. 1963, AIChE, 9, 175
de Avillez, M., & Mac Low, M.-M. 2002, ApJ, 581, 1047
De Stefano, G., Vasilyev, O. V., & D. E. 2008, PhFl, 20, 045102
Dimonte, G., & Tipton, R. 2006, PhFl, 18, 085101
Dopazo, C. 1979, PhFl, 22, 20
Dopazo, C., & O'Brien, E. E. 1974, AcA, 1, 1239
Dopazo, C., Valino, L., & Fueyo, N. 1997, IJMPB, 11, 2975
Duplat, J., & Villermaux, E. 2008, JFM, 617, 51
Eidson, T. M. 1985, JFM, 158, 245
Ellis, R. S., McLure, R. J, Dunlop, J. S, et al. 2013, ApJL, 763, L7
Erlebacher, G., Hussaini, M. Y., Speziale, C. G., & Zang, T. A. 1992, JFM, 238, 155
Fang, Y., & Menon, S. 2006, in 44th AIAA Aerospace Sciences Meeting and Exhibit, AIAA Paper 2006-116
Federrath, C., Roman-Duval, J., Klessen, R. S., Schmidt, W., & Mac Low, M.-M. 2010, A&A, 512, 81
Ferrara, A. 2001, in ASP Conf. Ser. 222, The Physics of Galaxy Formation, ed. M. Umemura & H. Susa (San Francisco, CA: ASP), 301
Fox, R. O. 2003, Computational Models for Turbulent Reacting Flows (Cambridge: Cambridge Univ. Press)
Frebel, A., Collet, R., Eriksson, K., Christlieb, N., & Aoki, W. 2008, ApJ, 684, 588
Frebel, A., Johnson, J., & Bromm, V. 2009, MNRAS, 392, L50
Fryxell, B., Muller, E., & Arnett, D. 1989, in Proc. of the Fifth Workshop on Nuclear, Computation of Multi-dimensional Flows with Non-uniform Composition, ed. W. Hillbrandt & E. Muller (MPA-PI; Garching: MPI), 100
Fryxell, B., Olson, K., Ricker, P., et al. 2000, ApJS, 131, 273
Fumagalli, M., O'Meara, J. M., & Prochaska, J. X. 2011, Sci, 334, 1245
Gallerano, F., Pasero, E., & Cannata, G. 2005, CMT, 17, 101
Gao, F., & O'Brien, E. E. 1993, PhFl, 5, 1282
Garnier, E., Adams, N., & Sagaut, P. 2009, Large Eddy Simulation for Compressible Flows (Scientific Computation) (1st ed.; The Netherlands: Springer)
Genin, F., & Menon, S. 2010, JTurb, 11, 1
Germano, M. 1992, JFM, 238, 325
Germano, M., Piomelli, U., Moin, P., & Cabot, W. H. 1991, PhFl, 3, 1760
Ghosal, S., Lund, T. S., Moin, P., & Akselvoll, K. 1995, JFM, 286, 229
Girimaji, S. S. 1991, CST, 78, 177
Greif, T. H., Bromm, V., Clark, P. C., et al. 2012, MNRAS, 424, 399
Greif, T. H., Glover, S. C. O., Bromm, V., & Klessen, R. S. 2009, MNRAS, 392, 1381
Greif, T. H., Glover, S. C. O., Bromm, V., & Klessen, R. S. 2010, ApJ, 716, 510
Hanayama, H., & Tomisaka, K. 2006, ApJ, 641, 905
Hansen, M., & Oh, S. P. 2006, MNRAS, 367, 979
Haworth, D. C. 2010, PrECS, 36, 168
Heger, A., & Woosley, S. E. 2002, ApJ, 567, 532
Hosokawa, T., Omukai, K., Yoshida, N., & Yorke, H. W. 2011, Sci, 334, 1250
Hutchins, J. B. 1976, ApJ, 241, 103
Ievlev, V. M. 1973, DoSSR, 208, 1044
Inoue, A. K., Kousai, K., Iwata, I., et al. 2011, MNRAS, 411, 2336
Jaberi, F. A., Colucci, P. J., James, S., Givi, P., & Pope, S. B. 1999, JFM, 401, 85
Janicka, J., Kolbe, W., & Kollmann, W. 1979, JNET, 4, 47
Jimenez, C., Ducros, F., Cuenot, B., & Bedat, B. 2001, PhFl, 13, 1748
Jimenez, R., & Haiman, Z. 2006, Natur, 440, 501
Johnson, J. L., & Bromm, V. 2006, MNRAS, 366, 247
Kashikawa, N., Nagao, T., Toshikawa, J., et al. 2012, ApJ, 761, 85
Kim, W.-W., & Menon, S. 1999, IJNMF, 31, 983
Kollmann, W. 1990, ThCFD, 1, 249
Kosovic, B., Pullin, D., & Samtaney, R. 2002, PhFl, 14, 1511
Lesieur, M., & Metais, O. 1996, AnRFM, 28, 45
Lilly, D. K. 1966, NCAR Manuscript No. 123 (Boulder, CO: NCAR)
Lilly, D. K. 1992, PhFlA, 4, 633
Lundgren, T. S. 1967, PhFl, 12, 485
Maeder, A. 1992, A&A, 264, 105
Maio, U., Ciardi, B., Dolag, K., Tornatore, L., & Khochfar, S. 2010, MNRAS, 407, 1003
McKee, C. F., & Tan, J. C. 2008, ApJ, 681, 771
Meneveau, C., & Katz, J. 2000, AnRFM, 32, 1
Menon, S., & Kim, W.-W. 1996, in 34th Aerospace Sciences Meeting and Exhibit, AIAA Paper 96-0425
Moeng, C.-H. 1984, JAtS, 41, 2052
Moin, P., Squires, K., Cabot, W., & Lee, S. 1991, PhFl, 3, 2746
Monin, A. S. 1967, DoSSR, 177, 1036
Nagao, T., Sasaki, S. S., Maiolino, R., et al. 2008, ApJ, 680, 100
Neufeld, D. A. 1991, ApJL, 370, L85
Norman, C. A., & Spaans, M. 1997, ApJ, 480, 145
Norris, J. E., Christlieb, N., Korn, A. J., et al. 2007, ApJ, 670, 774
O'Brien, E. E. 1980, in Turbulent Reacting Flows, ed. P. A. Libby & F. A. Williams (New York: Springer-Verlag), 185
Oey, M. S. 2000, ApJL, 542, L25
Oey, M. S. 2003, MNRAS, 339, 849
Omukai, K., Tsuribe, T., Schneider, R., & Ferrara, A. 2005, ApJ, 626, 627
Padoan, P., Nordlund, A., Kritsuk, A. G., Normaln, M. L., & Li, P. S. 2007, ApJ, 661, 972
Pan, L., & Scalo, J. 2007, ApJ, 654, 29
Pan, L., & Scannapieco, E. 2010, ApJ, 721, 1765 (PS10)
Pan, L., & Scannapieco, E. 2011, PhRvE, 83, 045302(R)
Pan, L., Scannapieco, E., & Scalo, J. 2012, JFM, 700, 459 (PSS)
Park, N., & Mahesh, K. 2007, in 45th AIAA Aerospace Sciences Meeting and Exhibit, AIAA Paper 2007-0722
Pierce, C. D., & Moin, P. 1998, PhFl, 10, 3041
Piomelli, U., Cabot, W. H., Moin, P., & Lee, S. 1991, PhFl, 3, 1766
Pitsch, H. 2006, AnRFM, 38, 453
Pitsch, H., & Steiner, H. 2000, PhFl, 12, 2541
Pope, S. B. 1976, CoFl, 27, 299
Pope, S. B. 1985, PrECS, 11, 119
Pope, S. B. 2000, Turbulent Flows (Cambridge: Cambridge Univ. Press)
Rhoads, J. E., Malhotra, S., Dey, A., et al. 2000, ApJL, 545, L85
Ritter, J. S., Safranek-Shrader, C., Gnat, O., Milosavljevic, M., & Bromm, V. 2012, ApJ, 761, 56
Scalo, J., & Biswas, A. 2002, MNRAS, 332, 769
Scannapieco, E., & Brüggen, M. 2010, MNRAS, 405, 1634
Scannapieco, E., Kawata, D., Brook, C. B., et al. 2006, ApJ, 653, 285
Scannapieco, E., Madau, P., Woosley, S., Heger, A., & Ferrara, A. 2005, ApJ, 633, 1031
Scannapieco, E., Schneider, R., & Ferrara, A. 2003, ApJ, 589, 35
Schaerer, D. 2002, A&A, 382, 28
Schmidt, W., Niemeyer, J. C., & Hillebrandt, W. 2006, A&A, 450, 265
Schneider, R., Ferrara, A., Salvaterra, R., Omukai, K., & Bromm, V. 2003, Natur, 442, 869
Schneider, R., Omukai, K., Bianchi, S., & Valiante, R. 2012, MNRAS, 419, 1566

Schumann, U. 1975, JCoPh, 18, 376
Simcoe, R. A., Sullivan, P. W., Cooksey, K. L., et al. 2012, Natur, 492, 79
Smagorinsky, J. 1963, MWRv, 91, 99
Spaans, M., & Silk, J. 2005, ApJ, 626, 644
Speziale, C. G., Hussaini, M. Y., Erlebacher, G., & Zang, T. A. 1988, PhFl, 31, 940
Stacy, A., Greif, T. H., & Bromm, V. 2010, MNRAS, 403, 45
Thornton, K., Gaudlitz, M., Janka, H.-Th., & Steinmetz, M. 1998, ApJ, 500, 95
Tinsley, B. M. 1980, FCPh, 5, 287
Trenti, M., & Stiavelli, M. 2007, ApJ, 667, 38
Trenti, M., & Stiavelli, M. 2009, ApJ, 694, 879
Turk, M. J., Abel, T., & O'Shea, B. 2009, Sci, 325, 601
Venaille, A., & Sommeria, J. 2007, PhFl, 19, 028101
Venaille, A., & Sommeria, J. 2008, PhRvL, 100, 234506
Villermaux, E., & Duplat, J. 2003, PhRvL, 91, 184501
Vreman, B., Geurts, N., & Kuerten, H. 1997, JFM, 339, 357
Walker, T. P., Steigman, G., Kang, H.-S., Schramm, D. M., & Olive, K. 1991, ApJ, 376, 51
Watanabe, T., & Gotoh, T. 2004, NJPh, 6, 40
Whalen, D. J., Even, W., Frey, L. H., et al. 2012, ApJ, submitted (arXiv:1211.4979)
Wise, J. H., & Abel, T. 2008, ApJ, 685, 40
Woosley, S. E., & Weaver, T. A. 1995, ApJS, 101, 181
Yong, D., Norris, J. E., Bessell, M. S., et al. 2012, ApJ, 762, 27
Yoshizawa, Y. 1986, PhFl, 29, 2152